Damping, on-chip transduction, and coherent control of nanomechanical resonators

Dissertation der Fakultät für Physik der
Ludwigs-Maximilians-Universität München

vorgelegt von
Thomas Faust
geboren in München

München, Februar 2013

Erstgutachter: Prof. Jörg Kotthaus
Zweitgutachter: Prof. Joachim Rädler
Tag der mündlichen Prüfung: 26. April 2013

Zusammenfassung

Nanomechanische Resonatoren sind kleine, schwingende Systeme, deren Abmessungen in zumindest einer Dimension unter einem Mikrometer betragen. Aufgrund ihrer geringen Abmessungen und der sehr kleinen Massen reagieren sie auf minimale Änderungen in ihrer Umgebung, was sie zu sehr empfindlichen Sensoren macht. Die Eigenschaften der Resonatoren verändern sich allerdings mit zunehmender Miniaturisierung, sodass auch neue Antriebs- und Detektionskonzepte erforderlich werden.

In dieser Arbeit wird zuerst ein hochempfindlicher, rein elektrischer Detektionsmechanismus entwickelt. Hierfür wird ein beidseitig eingespannter Balken aus Siliziumnitrid zwischen zwei Elektroden positioniert, sodass seine Bewegung winzige Kapazitätsänderungen hervorruft. Diese werden an einen Mikrowellenschwingkreis, dessen Resonanzfrequenzvariation sehr genau messbar ist, gekoppelt. So lässt sich einerseits die thermische Bewegung des Balkens bei Raumtemperatur auflösen, und andererseits kann durch "opto"mechanische Rückwirkung die Dämpfung des mechanischen Resonators verändert werden, wodurch er sogar sich sogar in Selbstoszillation bringen lässt. Alternativ können auch zusätzlich Gleich- und Wechselspannungen an die Elektroden angelegt werden, womit der Balken sowohl in seiner Resonanzfrequenz verstimmt als auch angetrieben werden kann.

Das dabei entstehende, stark inhomogene elektrische Feld erzeugt zusätzlich eine Kopplung zwischen den beiden orthogonalen Biegemoden des Balkens, sodass ein abstimmbares System aus zwei gekoppelten harmonischen Oszillatoren gebildet wird. In einem ersten Versuch wird anhand von Landau-Zener-Übergängen die zeitaufgelöste Kontrolle des Systems demonstriert. Mit einer leicht verbesserten Probe können dann auch gepulste, kohärente Experimente mit dem nanomechanischen Zwei-Niveau-System durchgeführt werden. Durch die richtige Wahl der Pulse lässt sich jeder beliebige Zustand auf der Bloch-Kugel erreichen, während Ramsey- und Spin-Echo-Sequenzen die vollständige Charakerisierung der Kohärenzzeiten ermöglichen. Hierbei zeigt sich, dass alle Phononen in der gleichen kollektiven Mode beinhaltet sind und somit keine inhomogene Verbreiterung zu beobachten ist. Außerdem findet einzig Energierelaxation statt, da die dominate Wechselwirkungsprozesse mit kurzwelligen Phononen inelastisch sind. Somit sind sämtliche Kohärenzzeiten des Systems durch die mechanische Dämpfung limitiert.

Anfangs- und Endpunkt der Arbeit ist die Untersuchung des Dämpfungsverhaltens zugverspannter Silizumnitridresonatoren. Hierbei wird zunächst die gemesse Dämpfung vieler verschiedener Balken und Obermoden in einem einfachen Modell reproduziert, welches auch den Zusammenhang zwischen der außergewöhnlich hohen Güte und der Zugspannung der Resonatoren erklärt. Durch die Fortschritte in der Detektionstechnik kann am Ende der Arbeit die Dämpfung eines Resonators über einen weiten Temperaturbereich vermessen werden, wobei sich die charakteristische Signatur der für amorphe Systeme typischen Defekte zeigt.

Contents

Chapter 1

Introduction

Advances in microfabrication techniques have led to an integration of small mechanical elements into conventional CMOS integrated circuits. These combinations of a mechanical resonator with an electrical circuit are called microelectromechanical systems (MEMS), which have found widespread applications, for example in gyrometers, acceleration sensors, radio frequency filters and micrufluidic components [Jud01, Luc04, Dea09, Bhu11].

Even smaller resonators are not yet used in industrial applications, but have been the subject of intense research over the last few years. Nanomechanical resonators with masses in the picogramm range were cooled down to the quantum ground state of their harmonic oscillator mode [O'C10, Teu11, Cha11], making them the world's largest quantum objects [Cho10] and opening up new possibilities to test the predictions of quantum theories using macroscopic objects. Apart from such fundamental experiments, there are numerous, more practical utilizations of nanomechanical resonators. Their small masses and high sensitivity to environmental changes make them ideal candidates for extremely sensitive mass [Yan06, Jen08, Cha12], force [Sto97, Mam01, Arl06] and gas or chemical [Hag01, Li10] sensors. Apart from these frequency-shift based sensing techniques, the sharp mechanical resonances allow building nanoelectromechanical oscillators [Fen08, Unt10d] while the nonlinear properties are useful for memory elements [Koz07, Roo09, Unt10c] and amplifiers [Kar11].

For all of these applications, several aspects of the nanomechanical system are of particular importance: Firstly, low mechanical losses are an essential criterion. The usual figure of merit is the quality factor of the harmonic oscillator. It is a dimensionless number given by the resonance frequency divided by the linewidth of the resonance. Alternatively, it can be defined as the number of oscillation cycles during a ringdown to $1/e$ of the energy.

A second important feature is a sensitive detection scheme to read out the motion of the mechanical resonators. There are numerous techniques available, which can be divided into two groups. On the one hand, there are optical techniques, mostly using some sort of cavity to achieve excellent sensitivities [Rug89, Kar05, Tho08, Ane09, Ane10b].

Their biggest disadvantage is the need for stable and precise positioning of the mechanical resonator relative to the optical components. On the other hand, a direct transduction of mechanical motion into a current or voltage can be achieved with electrical techniques. Examples include piezoelectric [Mas07, Mah08], magnetomotive [Cle96], capacitive [Kno03, Koz06] and dielectric [Unt09] detection schemes. As they rely on electrode structures patterned on the same chip as the mechanical resonator, positioning is not an issue. Furthermore, a multitude of mechanical elements can be connected in parallel and read out simultaneously. The disadvantages include a more challenging microfabrication and restrictions on the (piezo-)electrical properties of the resonator material.

Lastly, the mechanical resonance needs to be actuated, and some kind of tuning mechanism is essential if the frequency is to be adjusted to other systems. An external piezoelectric transducer [Ver06] enables the simultaneous actuation of a multitude of beams, while photothermal effects [Ili05, Sam06] allow for an all-optical drive. Most of the already mentioned electrical detection schemes can also be reversed to tune and actuate a resonator by applying constant and alternating voltages or currents [E05].

1.1 Scope of the thesis

This work is a cumulative thesis, meaning that some chapters (2.1, 3.1, 3.2, 4.1 and 4.2) consist of the un-modified original publications that resulted from this project. The starting point for this work were the unusually high mechanical quality factors of prestressed silicon nitride beam resonators, first discovered in 2006 [Ver06]. A systematic study [Unt10b] revealed a dependence on beam length and mode number, which can be explained by a theoretical model developed by Q. Unterreithmeier [Unt10a]. These results are presented in the first half of chapter 2, while the second half describes a few similar measurements at low temperatures using a fiber-optical detection setup.

As this setup proved to be rather unsuitable for extended and reliable low-temperature operation, a new detection scheme is developed in chapter 3: The first half describes a microwave cavity based detection scheme [Fau12a] utilizing the dielectric coupling to a silicon nitride beam previously mostly used for actuation [Sch06, Unt09]. This allows for a positioning-free, multiplexed readout of multiple beams with comparable sensitivity to the previously used fiber-optical setup, while the cavity backaction additionally provides control over the mechanical quality factor. The second half of the chapter introduces a small modificiation of the setup allowing to integrate the dielectric actuation via dc and rf voltages with this microwave readout [Rie12]. Apart from the dielectric actuation and tuning as well as microwave detection, this also provides a means to voltage-tune the mechanical quality factor, as dielectric damping effects in the beam material begin to play a significant role in the large inhomogeneous electric field created by the dc voltage.

With a suitable electrode geometry, the dc voltage tuning can be used to match the resonance frequencies of the in-plane and out-of-plane flexural modes. They then exhibit a pronounced avoided crossing, indicating strong coupling between the two modes,

which is the subject of chapter 4. In the first section, Landau-Zener transitions between the two modes are studied and an excellent agreement with a classical theoretical model is achieved [Fau12c]. The second section uses the two hybrid modes formed by the coupled modes as the discrete energy levels of a two-level system. Using pulsed excitations, experiments demonstrating the coherent control of the superposition states can be performed [Fau12b]. As the coherence time is solely limited by energy decay, cavity backaction effects of the readout cavity can be used to enhance or decrease the coherence time of the system. Furthermore, Stückelberg oscillations are another experimental proof of the coherent nature of the investigated mechanical system.

Chapter 5 once again deals with the dissipation mechanisms in silicon nitride resonators. The electrical transduction technique presented before enables the temperature-dependent measurement of the mechanical properties of a silicon nitride resonator. The mechanical damping between 8 and 300 K provides a strong indication that the loss process is dominated by localized defects in the resonator material, a well-known phenomenon in glassy systems. The second part of the chapter presents the first advances towards silicon nitride resonators coupled to on-chip niobium coplanar waveguides. This will allow highly sensitive measurements at very low temperatures, as the extremely low losses of the superconducting microwave circuits lead to negligible power dissipation and a highly increased detection sensitivity.

A final conclusion sums up the work and provides an outlook on possible future projects. The appendices provides additional information not mentioned in the published articles as well as details of the fabrication process and measurement setup.

Chapter 2

Dissipation in silicon nitride - Part 1

Mechanical resonators made from a thin, pre-stressed layer of silicon nitride (SiN) offer high resonator frequencies at moderate device dimensions and a simple fabrication, as they are very robust, even in a liquid environment [Ver06]. Their most striking feature is the exceptionally high quality factor compared to other nanomechanical resonators of similar size or frequency. Shortly after the first use of silicon nitride resonators in 2006 [Ver06], a chip bending experiment [Ver07] demonstrated a direct connection between the resonator stress and the mechanical quality factor. Both single-crystal silicon as well as silicon nitride resonators showed an increased quality factor when external stress was applied to the devices. However, this work as well as later articles [Sou09] were unable to explain the mechanism connecting the external or built-in stress to the increase in quality factor.

For a more systematic study of this effect, we decided to fabricate doubly-clamped silicon nitride beams with multiple lengths ranging from 5 to 35 µm. The lengths were chosen such that higher harmonics of the longest resonator would have the same wavelength (i. e. distance between two antinodes) as the fundamental modes of the shorter beams. Each beam was driven electrically via dielectric actuation [Sch06, Unt09], the readout was performed using a fiber-based interferometric technique [Aza07]. The measured quality factors over a whole frequency decade allowed us to develop and test a theoretical model, explaining the measured values. This model, which was mainly developed by Q. Unterreithmeier [Unt10a], is based on the assumption that the relevant losses occur inside the resonator material and are proportional to the local bending. A more detailed description of this model and other remarks on the experiment can be found in appendix C (not included in the main part of the thesis as this part of the work was mostly created by Q. Unterreithmeier).

These results, presented in chapter 2.1, do not allow to determine the actual microscopic loss mechanism which leads to the observed damping, but the most likely candidate are localized defects in the amorphous silicon nitride with a broad energy spectrum. At low temperatures, such defects are usually referred to as two-level systems and are a common phenomenon in glasses such as silicon oxide or silicon nitride. Their dissipation

exhibits a very characteristic temperature dependence [Arc09], which is well-described in the literature [Vac05], thus a measurement of mechanical quality factors at different temperatures should clarify their role in the mechanical dissipation.

First measurements of silicon nitride beam quality factors at temperatures near 4 K are presented in chapter 2.2. Actuation and detection is performed similar to the room temperature measurements described in chapter 2.1. The optical readout causes several problems: Higher optical powers lead to a decent signal to noise ratio but heat the sample, while very low light powers create only a very weak signal and thus large errors for the measured quality factors. Furthermore, the precise positioning requirements of the fiber relative to the sample necessitates frequent adjustment of the fiber position, especially when the temperature of the cryostat is changed. This prompted the developement of an improved, all-electrical detection setup employing a microwave resonator, which is presented in chapter 3.

2.1 Damping of Nanomechanical Resonators

Published as *Physical Review Letters* **105**, 027205 (2010), reference [Unt10b].

Damping of Nanomechanical Resonators

Quirin P. Unterreithmeier,* Thomas Faust, and Jörg P. Kotthaus

Fakultät für Physik and Center for NanoScience (CeNS), Ludwig-Maximilians-Universität, Geschwister-Scholl-Platz 1, D-80539 München, Germany

(Received 9 March 2010; published 9 July 2010)

We study the transverse oscillatory modes of nanomechanical silicon nitride strings under high tensile stress as a function of geometry and mode index $m \leq 9$. Reproducing all observed resonance frequencies with classical elastic theory we extract the relevant elastic constants. Based on the oscillatory local strain we successfully predict the observed mode-dependent damping with a single frequency-independent fit parameter. Our model clarifies the role of tensile stress on damping and hints at the underlying microscopic mechanisms.

DOI: 10.1103/PhysRevLett.105.027205 PACS numbers: 85.85.+j, 46.40.Ff, 62.40.+i

The resonant motion of nanoelectromechanical systems has received a lot of recent attention. Their large frequencies, low damping, i.e., high mechanical quality factors, and small masses make them equally important as sensors [1–4] and for fundamental studies [3–9]. In either case, low damping of the resonant motion is very desirable. Despite significant experimental progress [10,11], a satisfactory understanding of the microscopic causes of damping has not yet been achieved. Here we present a systematic study of the damping of doubly-clamped resonators fabricated out of prestressed silicon nitride leading to high mechanical quality factors [10]. Reproducing the observed mode frequencies applying continuum mechanics, we are able to quantitatively model their quality factors by assuming that damping is caused by the local strain induced by the resonator's displacement. We thereby deduce that the high quality factors of strained nanosystems can be attributed to the increase in stored elastic energy rather than a decrease in energy loss. Considering various microscopic mechanisms, we conclude that the observed damping is most likely dominated by dissipation via localized defects uniformly distributed along the resonator.

We study the oscillatory response of nanomechanical beams fabricated from high stress silicon nitride (SiN). A released doubly-clamped beam of such a material is therefore under high tensile stress, which leads to high mechanical stability [12] and high mechanical quality factors [10]. Such resonators therefore have been widely used in recent experiments [6,9]. Our sample material consists of a silicon substrate covered with 400 nm thick silicon dioxide serving as sacrificial layer and a $h = 100$ nm thick SiN device layer. Using standard electron beam lithography and a sequence of reactive ion etch and wet-etch steps, we fabricate a series of resonators having lengths of $35/n$ μm, $n = \{1, \ldots, 7\}$ and a cross section of 100×200 nm^2 as displayed in Figs. 1(a) and 1(b). Since the respective resonance frequency is dominated by the large tensile stress [10,13], this configuration leads to resonances of the fundamental modes that are approximately equally spaced in frequency. Suitably biased gold electrodes processed beneath the released SiN strings actuate the resonators via dielectric gradient forces to perform out-of-plane oscillations, as explained in greater detail elsewhere [12]. The length and location of the gold electrodes is properly chosen to be able to also excite several higher order modes of the beams. The experiment is carried out at room temperature in a vacuum below 10^{-3} mbar to avoid gas friction.

The displacement is measured using an interferometric setup that records the oscillatory component of the reflected light intensity with a photodetector and network analyzer [12,14]. The measured mechanical response around each resonance can be fitted using a Lorentzian line shape as exemplarily seen in the inset of Fig. 2. The thereby obtained values for the resonance frequency f and

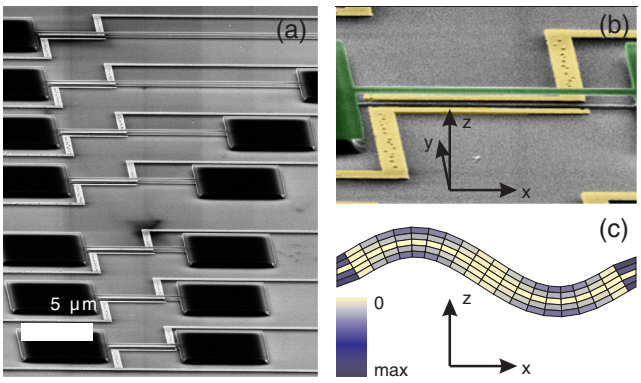

FIG. 1 (color online). *Setup and geometry.* (a) Scanning electron microscope picture of our sample; the lengths of the investigated nanomechanical silicon nitride strings are $35/n$ μm, $n = \{1, \ldots, 7\}$; their widths and heights are 200 nm and 100 nm, respectively. (b) Zoom-in of (a) the resonator (highlighted in green [dark gray]) is dielectrically actuated by the nearby gold electrodes (yellow [light gray]); its displacement is recorded with an interferometric setup. (c) Schematic mode profile and absolute value of the resulting strain distribution (color coded) of the second harmonic.

quality factor Q for all studied resonators and observed modes are displayed in Fig. 2 (filled circles). In order to reproduce the measured frequency spectrum, we apply standard beam theory (see, e.g., [15]). Without damping, the differential equation describing the spatial dependence of the displacement for a specific mode m of beam n $u_{n,m}[x]$ at frequency $f_{n,m}$ writes (with $\rho = 2800\ \mathrm{kg/m^3}$ being the material density [16]; E_1, σ_0 are the (unknown) real Young's modulus and built-in stress, respectively):

$$\frac{1}{12}E_1 h^2 \frac{\partial^4}{\partial x^4}u_{n,m}[x] - \sigma_0 \frac{\partial^2}{\partial x^2}u_{n,m}[x] - \rho(2\pi f_{n,m})^2 u_{n,m}[x] = 0 \quad (1)$$

Solutions of this equation have to satisfy the boundary conditions of a doubly-clamped beam (displacement and its slope vanish at the supports ($u_{n,m}[\pm l/(2n)] = (\partial/\partial x)u_{n,m}[\pm l/(2n)] = 0$, l/n: beam length). These conditions lead to a transcendental equation that is numerically solved to obtain the frequencies $f_{n,m}$ of the different modes.

The results are fitted to excellently reproduce the measured frequencies, as seen in Fig. 2 (hollow squares). One thereby obtains as fit parameters the elastic constants of the microprocessed material $E_1 = 160$ GPa, $\sigma_0 = 830$ MPa, in good agreement with previously published measurements [13].

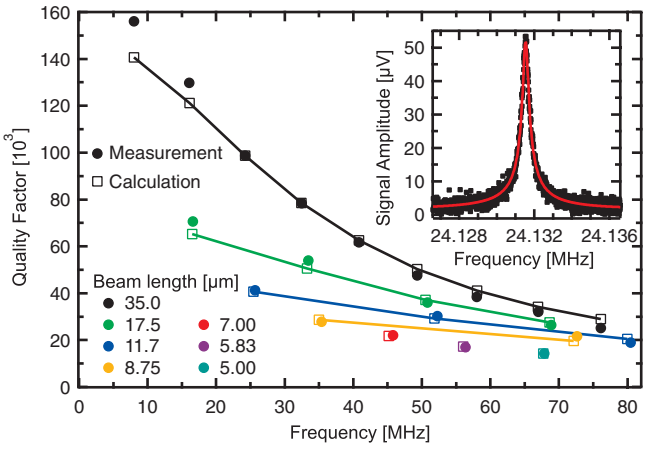

FIG. 2 (color online). *Resonance frequency and mechanical quality factor.* The harmonics of the nanomechanical resonator show a Lorentzian response (exemplary in the inset). Fitting yields the respective frequency and mechanical quality factor. The main figure displays these values for several harmonics (same color) of different beams as indicted by the color. To reproduce the resonance frequencies, we fit a continuum model to the measured frequencies. We thereby retrieve the elastic constants of our (processed) material, namely, the built-in stress $\sigma_0 = 830$ MPa and Young's modulus $E_1 = 160$ GPa. From the displacement-induced, mode-dependent strain distribution, we calculate (except for an overall scaling) the mechanical quality factors. Calculated frequencies and quality factors are shown as hollow squares, the responses of the different harmonics of the same string are connected.

For each harmonic, we now are able to calculate the strain distribution within the resonator induced by the displacement $u[x]$ and exemplarily shown in Fig. 1(c). The measured dissipation is closely connected to this induced strain $\epsilon[x, z, t] = \epsilon[x, z]\exp[i2\pi f t]$. As in the model originally discussed by Zener [17] we now assume also for our case of a statically prestressed beam that the displacement-induced strain and the accompanying oscillating stress $\sigma[x, z, t] = \sigma[x, z]\exp[i2\pi f t]$ are not perfectly in phase; this can be expressed by a Young's modulus $E = E_1 + iE_2$ having an imaginary part. The relation reads again $\sigma[x, z] = (E_1 + iE_2)\epsilon[x, z]$. During one cycle of oscillation $T = 1/f$, a small volume δV of length s and cross section A thereby dissipates the energy $\Delta U_{\delta V} = As\pi E_2 \epsilon^2$. The total loss is obtained by integrating over the volume of the resonator.

$$\Delta U_{n,m} = \int_V dV \Delta U_{\delta V} = \pi E_2 \int_V dV \epsilon_{n,m}[x, z]^2 \quad (2)$$

The strain variation and its accompanying energy loss can be separated into contributions arising from overall elongation of the beam and its local bending. It turns out that here the former is negligible, despite the fact that the elastic energy is dominated by the elongation of the string, as discussed below. To very high accuracy we obtain for the dissipated energy $\Delta U_{n,m} \approx \pi/12 E_2 w h^3 \int_l dx(\partial^2/(\partial x)^2 u_{n,m})^2$. A more rigorous derivation can be found in the supplementary information [18]. The total energy depends on the spatial mode [through $\epsilon_{n,m}$, see exemplary Fig. 1(c)] and therefore strongly differs for the various resonances. To obtain the quality factor, one has to calculate the stored energy, e. g., by integrating the kinetic energy $U_{n,m} = \int_l dx A\rho(2\pi f_{n,m})^2 u_{n,m}[x]^2$. The overall mechanical quality factor is $Q = 2\pi U_{n,m}/\Delta U_{n,m}$. A more detailed derivation can be found in [18].

Assuming that the unknown value of the imaginary part E_2 of the elastic modulus is independent of resonator length and harmonic mode, we are left with one fit parameter E_2 to reproduce all measured quality factors and find excellent agreement (Fig. 2, hollow squares). We therefore successfully model the damping of our nanoresonators by postulating a frequency-independent mechanism caused by local strain variation. We wish to point out that the quality factor of, e.g., the second harmonic of a particular beam is significantly higher if compared to the fundamental one of a shorter beam with the same frequency. This can be understood by the fact that the maximum strain and thus local dissipation occurs near the clamping points and a higher harmonic has less clamping points per antinode [see Fig. 1(c)].

Allowing E_2 to depend on frequency, the accordance gets even better, as discussed in detail in [18].

We now discuss the possible implications of our findings, considering at first the cause of the high quality factors in overall prestressed resonators and then the compatibility of our model with different microscopic damping

mechanisms. In a relaxed beam, the elastic energy is stored in the flexural deformation and becomes for a small test volume $U_{\delta V} = 1/2AsE_1\epsilon^2$. In the framework of a Zener model, as employed here, this result is proportional to the energy loss [see Eq. (2)] and thus yields a frequency-independent quality factor $Q = E_1/E_2$ for the unstressed beam. In accordance with this finding, Ref. [10] reports a much weaker dependence of quality factor on resonance frequency, in strong contrast with the behavior of their stressed beams.

Similar as in the damping model, the total stored elastic energy in a beam can be very accurately separated into a part connected to the bending and a part coming from the overall elongation. The latter is proportional to the prestress σ_0 and vanishes for relaxed beams, refer to [18] for details. Assuming a constant $E = E_1 + iE_2$, Fig. 3 displays the calculation of the elastic energy and the quality factor for the fundamental mode of our longest ($l = 35\ \mu$m) beam as a function of overall built-in stress σ_0. The total elastic energy is increasingly dominated by the displacement-induced elongation $U_{\text{elong}} = 1/2\sigma_0 wh \int_l dx(\partial/(\partial x)u[x])^2$. In contrast the bending energy $U_{\text{bend}} = 1/24E_1 wh^3 \int_l dx(\partial^2/(\partial x)^2 u[x])^2$, which in our model is proportional to the energy loss, is found to increase much slower with σ_0. Thus one expects Q to increase with σ_0, a finding already discussed by Schmid and Hierold for micromechanical beams [19]. However, their model assumes the simplified mode profile of a stretched string and can not explain the larger quality factors of higher harmonics when compared to a fundamental resonance of the same frequency. Including beam stiffness, our model can fully explain the dependence of frequency and damping on length and mode index, as reflected in Fig. 2. It also explains the initially surprising finding [20] that amorphous silicon nitride resonators exhibit high quality factors when stretched whereas having Q

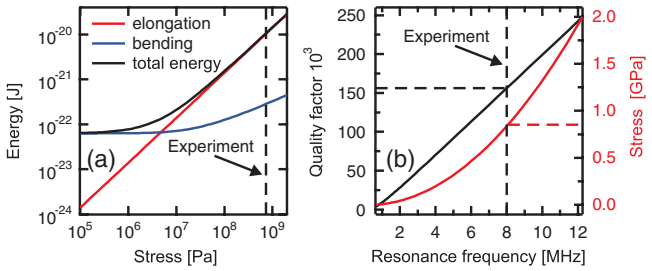

FIG. 3 (color online). *Elastic energy and mechanical quality factor of the beam in dependence of stress.* (a) The elastic energies of the fundamental mode of the beam with $l = 35\ \mu$m are displayed vs applied overall stress separated into the contributions resulting from the overall elongation and the local bending. The dashed line marks the strain of the experimentally studied resonator $\sigma_0 \approx 830$ MPa, there the elongation term dominates noticeably. (b) Quality factor and frequency are calculated for varying stress σ_0. In order to compare the calculation with other published results, quality factor and stress are displayed vs resulting frequency.

factors in the relaxed state that reflect the typical magnitude of internal friction found to be rather universal in glassy materials [21]. More generally we conclude that the increase in mechanical quality factors with increasing tensile stress is not bound to any specific material.

Since the resonance frequency is typically easier to access in an experiment, we plot the quality factor vs corresponding resonance frequency in Fig. 3(b), with both numbers being a function of stress. The resulting relation of quality factor on resonance frequency is (except for very low stress) almost linear; experimental results by another group can be seen to agree well with this finding [22]. In addition, we show in [18] that although the energy loss per oscillation increases with applied stress, the linewidth of the mechanical resonance decreases.

We will now consider the physical mechanisms that could possibly contribute to the observed damping. As explained in greater detail in [18], we can safely neglect dampings that are intrinsic to any (bulk) system, namely, clamping losses [23,24], thermoelastic damping [25,26] and Akhiezer damping [26,27], since the corresponding model calculations all predict damping constants significantly smaller than the ones observed.

Therefore, we would like to discuss the influence of localized (defect) states. Mechanisms with discrete relaxation rates will exhibit damping maxima whenever the oscillation frequency matches the relaxation rate [25,26,28]. As our model however is based on a frequency-independent loss mechanism, we therefore conclude that a broad range of states is responsible for the observed damping. This assumption is consistent with a model calculation dealing with the influence of two-level systems on acoustic waves [29] at high temperatures. There, the strain modulates the energy separation of the two states and thereby excites the system out of thermal equilibrium; the subsequent relaxation causes the energy loss. In addition, published quality factors of relaxed silicon nitride nanoresonators [20] cooled down to liquid helium temperature display quality factors that are well within the typical range of amorphous bulk materials [21], therefore the observed damping mechanism can be assumed to reduce to the concept of two-level systems at low temperatures. Moreover, on a different sample chip we measured a set of resonators showing quality factors that are uniformly decreased by a factor of approximately 1.4 compared to the data presented in Fig. 2; the corresponding data are presented in [18]. Their response can still be quantitatively modeled resulting in an increased imaginary part of Young's modulus E_2. We attribute this reduction in quality factor to a nonoptimized RIE-etch step, that leads to an increased density of defect states in the near-surface region of the resonator. In contrast, the above mentioned intrinsic mechanisms are not expected to be influenced by such processing.

We wish to point out some limitations of our simple model description. One is that the above stated simplification to local two-level systems cannot be rigorously ap-

plied at elevated temperatures as the concept of two-level systems should be replaced by local excitable systems. The other is that our assumption of a damping mechanism via localized defects distributed uniformly along the resonator cannot differentiate between surface and volume losses (see [18]). In fact, measurements performed on beams with larger width exhibit slightly higher quality factors pointing toward a contribution of surface defects as does the effect of sample processing discussed above, a well-known observation in micro- or nanoresonators, see e.g. [30,31]. At present we cannot conclude on the microscopic nature of the defect states implicitly assumed in our model. These could reflect the amorphous nature of the SiN resonator but also be influenced by near-surface modification.

In conclusion, we systematically studied the transverse mode frequencies and quality factors of prestressed SiN nanoscale beams. Implementing continuum theory, we reproduce the measured frequencies varying with beam length and mode index over an order of magnitude. Assuming that damping is caused by local strain variations induced by the oscillation, independent of frequency, enables us to calculate the observed quality factors with a single interaction strength as free parameter. We thus identify the unusually high quality factors of prestressed beams as being primarily caused by the increased elastic energy rather than a decrease in damping rate. Several possible damping mechanisms are discussed; because of the observed nearly frequency independent damping parameter E_2, we attribute the mechanism to interaction of the strain with local defects of not yet identified origin. One therefore expects that defect-free resonators exhibit even larger quality factors, as recently demonstrated for ultraclean carbon nanotubes [11].

Financial support by the Deutsche Forschungsgemeinschaft via Project No. Ko 416/18, the German Excellence Initiative via the Nanosystems Initiative Munich (NIM) and LMUexcellent as well as the Future and Emerging Technologies programme of the European Commission, under the FET-Open project QNEMS (233992) is gratefully acknowledged. We would like to thank Florian Marquardt and Ignacio Wilson-Rae for stimulating discussions.

*unterreithmeier@physik.uni-muenchen.de

[1] K. Jensen, K. Kim, and A. Zettl, Nature Nanotech. **3**, 533 (2008).
[2] B. Lassagne, D. Garcia-Sanchez, A. Aguasca, and A. Bachtold, Nano Lett. **8**, 3735 (2008).
[3] M. D. LaHaye, J. Suh, P. M. Echternach, K. C. Schwab, and M. L. Roukes, Nature (London) **459**, 960 (2009).
[4] J. D. Teufel, T. Donner, M. A. Castellanos-Beltran, J. W. Harlow, and K. W. Lehnert, Nature Nanotech. **4**, 820 (2009).
[5] J. S. Aldridge and A. N. Cleland, Phys. Rev. Lett. **94**, 156403 (2005).
[6] T. Rocheleau, T. Ndukum, C. Macklin, J. B. Hertzberg, A. A. Clerk, and K. C. Schwab, Nature (London) **463**, 72 (2010).
[7] M. Li, W. H. P. Pernice, C. Xiong, T. Baehr-Jones, M. Hochberg, and H. X. Tang, Nature (London) **456**, 480 (2008).
[8] S. Etaki, M. Poot, I. Mahboob, K. Onomitsu, H. Yamaguchi, and H. S. J. van der Zant, Nature Phys. **4**, 785 (2008).
[9] M. Eichenfield, R. Camacho, J. Chan, K. J. Vahala, and O. Painter, Nature (London) **459**, 550 (2009).
[10] S. S. Verbridge, J. M. Parpia, R. B. Reichenbach, L. M. Bellan, and H. G. Craighead, J. Appl. Phys. **99**, 124304 (2006).
[11] A. K. Huettel, G. A. Steele, B. Witkamp, M. Poot, L. P. Kouwenhoven, and H. S. J. van der Zant, Nano Lett. **9**, 2547 (2009).
[12] Q. P. Unterreithmeier, E. M. Weig, and J. P. Kotthaus, Nature (London) **458**, 1001 (2009).
[13] Q. P. Unterreithmeier, S. Manus, and J. P. Kotthaus, Appl. Phys. Lett. **94**, 263104 (2009).
[14] N. O. Azak, M. Y. Shagam, D. M. Karabacak, K. L. Ekinci, D. H. Kim, and D. Y. Jang, Appl. Phys. Lett. **91**, 093112 (2007).
[15] W. Weaver, S. P. Timoshenko, and D. H. Young, *Vibration Problems in Engineering* (Wiley, New York, 1990).
[16] M. G. el Hak, *The MEMS Handbook* (CRC Press, Boca Raton, 2001).
[17] C. Zener, Phys. Rev. **53**, 90 (1938).
[18] See supplementary material at http://link.aps.org/supplemental/10.1103/PhysRevLett.105.027205.
[19] S. Schmid and C. Hierold, J. Appl. Phys. **104**, 093516 (2008).
[20] D. R. Southworth, R. A. Barton, S. S. Verbridge, B. Ilic, A. D. Fefferman, H. G. Craighead, and J. M. Parpia, Phys. Rev. Lett. **102**, 225503 (2009).
[21] R. O. Pohl, X. Liu, and E. Thompson, Rev. Mod. Phys. **74**, 991 (2002).
[22] S. Verbridge, D. Shapiro, H. Craighead, and J. Parpia, Nano Lett. **7**, 1728 (2007).
[23] Z. Hao, A. Erbil, and F. Ayazi, Sens. Actuators. A, Phys.**109**, 156 (2003).
[24] I. Wilson-Rae, Phys. Rev. B **77**, 245418 (2008).
[25] R. Lifshitz and M. L. Roukes, Phys. Rev. B **61**, 5600 (2000).
[26] A. A. Kiselev and G. J. Iafrate, Phys. Rev. B **77**, 205436 (2008).
[27] A. Akhieser, J. Phys. (Moscow) **1**, 277 (1939).
[28] A. N. Cleland, *Foundations of Nanomechanics* (Springer, New York, 2003).
[29] J. Jackle, Z. Phys. **257**, 212 (1972).
[30] J. L. Yang, T. Ono, and M. Esashi, J. Microelectromech. Syst. **11**, 775 (2002).
[31] D. W. Carr, S. Evoy, L. Sekaric, H. G. Craighead, and J. M. Parpia, Appl. Phys. Lett. **75**, 920 (1999).

2.2 Optical measurements at low temperatures

To continue the work presented in the last chapter, measurements of the mechanical properties of several resonators at different temperatures will help to determine the actual microscopic mechanism leading to dissipation in silicon nitride beams. As shown in the work of Arcizet et al. [Arc09] using an unstressed silica microresonator, a quality factor dominated by interaction with two-level systems will lead to a dissipation peak at a temperature in the range of 50 K in typical glasses. As the silicon nitride thin films used to fabricate the resonators are also an amorphous material, a similar behaviour is to be expected.

2.2.1 Measurement Setup

The chip design used in the previous chapter does not need to be altered for low temperature operation, as the dielectric drive works independently of the temperature. The detection scheme using a cleaved fiber tip positioned directly above the resonator can also be used at low temperatures, although the amount of reflected light collected by the fiber is very low (caused by the divergent beam profile exiting a single-mode fiber). An improvement can be made by using so-called "lensed fibers", where the fiber tip is manufactured to form a lens with a focal length of approximately 10 µm. This leads to a much stronger signal on the photodetector at the same laser input power, and thus helps to reduce laser heating. Additionally, the well-defined focal plane allows for a more controlled approach of the fiber tip to the sample surface, as the intensity of the reflected light exhibits a sharp maximum at the correct distance.

The sample is mounted inside a closed cycle pulse tube cryostat manufactured by *VERICOLD*, reaching a base temperature slightly below 4 K. To further reduce the sample temperature, it is equipped with an adiabatic demagnetisation refrigeration (ADR) stage, consisting of a large cylinder made from a paramagnetic salt connected to the sample stage and a 6 T superconducting magnet. To minimize heat conduction, the high-frequency connections needed to drive the beam resonances are realized via only 0.5 mm thick stainless steel semirigid coaxial cables down to the 4 K stage. The further connections use superconducting niobium semirigid cables. At every stage, the inner and outer conductors are thermalized via short microstrip transmission lines on a sapphire substrate which are introduced into the signal path.

The sample chip itself is glued to a gold-plated printed circuit board sample holder using conductive silver glue while gold bond wires are used to connect the two electrodes used for dielectric actuation. A ruthenium oxide temperature sensor is bonded onto the bottom side of the sample holder, ensuring an accurate temperature readout. As the sample holder is connected with the salt cylinder via a solid copper rod and is thus stationary inside the cryostat, the fiber tip is aligned with a ANP100 piezo positioner stack from *Attocube* (see Fig. 2.1) mounted upside down on the top portion (the 4 K stage) of the insert.

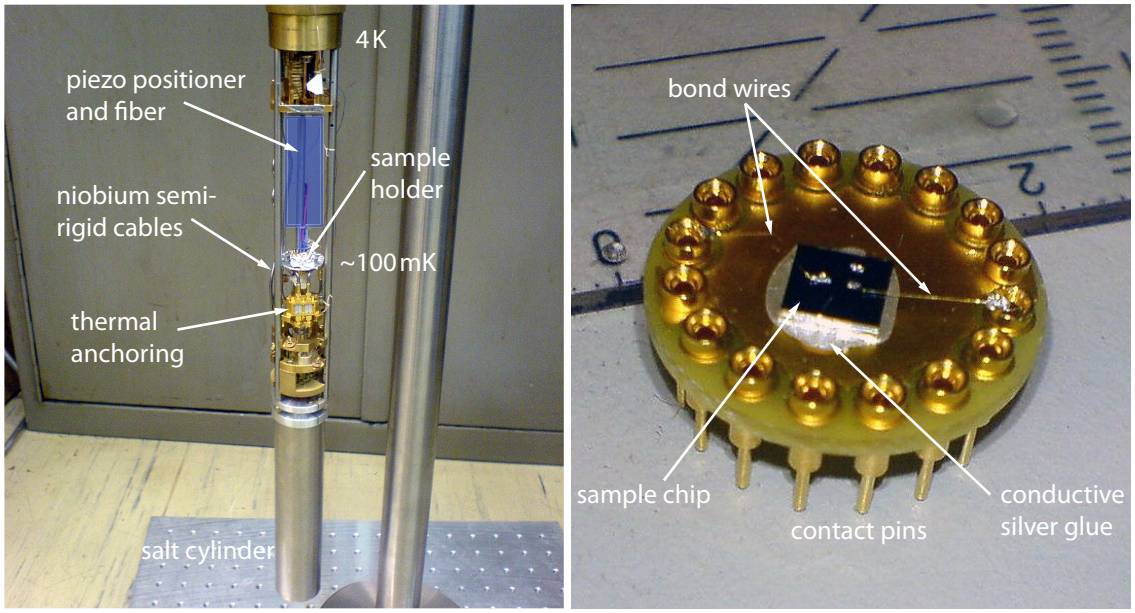

Figure 2.1: Pictures of the VERICOLD insert and the sample holder: On the left, the lower part of the cryostat insert is shown along with a sketched representation of the piezo positioner stage, which holds the fiber end closely above the chip surface. The sample holder is shown in more detail on the right, the bond wires connected with small indium dots are clearly visible.

A copper shield forms a vacuum-tight seal around the bottom part of the insert. Helium exchange gas is used to thermally connect the outer wall of the insert to the pulse tube cooler, while the thermal coupling of the salt cylinder (and thus the sample) to this 4 K reservoir can be controlled by the helium pressure in the inner volume. This allows to first thermalize the sample, and then measure in vacuum at either 4 K or even lower temperatures. To cool down further, the magnetic field needs to be turned on while the salt cylinder is still in contact with the exchange gas. All magnetic dipoles in the paramagnetic salt now align with the external field, entering a low-entropy state (and thereby heating the salt). If the exchange gas is pumped out after the salt is once again thermalized, and the magnetic field is slowly ramped down, the dipoles can flip back to a random orientation, thereby absorbing energy from their environment and thus reducing its temperature. With no laser illumination (or other heat source), temperatures as low as 60 mK can be reached. If the magnetic field once again reaches 0 T, the whole procedure has to be repeated, thus limiting the uninterrupted measurement time to about an hour at $\sim$500 mK in this experiment.

2.2.2 Low-temperature quality factors

A whole set of harmonics up to the 11th mode of a 35 µm long beam at approximately 4 K is measured. The quality factors of each resonance plotted versus the mode frequency (similar to the black data points of Fig. 2 in chapter 2.1) are shown in Fig. 2.2a. The the-

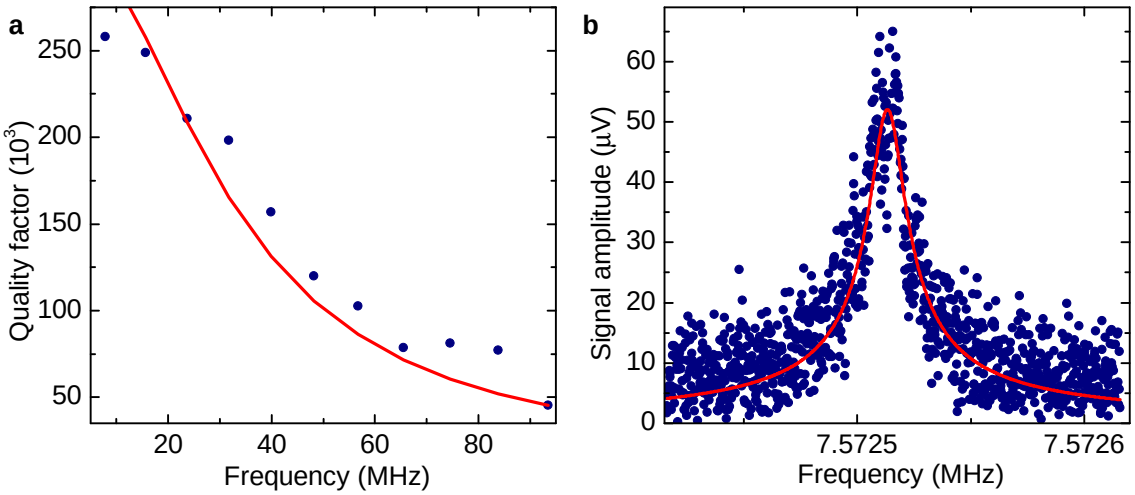

Figure 2.2: Measurement of low temperature resonances: Panel **a** shows the quality factors of several harmonics versus their frequency at approximately 4 K and a fit of the damping model. The response of the fundamental mode at 1 K is shown in **b** along with a fit.

oretical model used in chapter 2.1 and described in more detail in appendix C is fitted to the data points in order to extract the mechanical properties of the beam. The elastic parameters change slightly with temperature: The Youngs Modulus increases from 160 GPa at 300 K to 165 GPa at 4 K, while the prestress relaxes from 830 MPa down to 800 MPa, as the difference in the thermal expansion coefficients between the silicon nitride film and the silicon substrate slightly relaxes the stress with lowered temperatures.

The loss modulus E_2 is found to decrease from 40 to 20 MPa, which demonstrates that the dissipation inside the resonator decreases from room temperature to 4 K. Measurements of the full mode spectrum at even lower temperatures are hardly possible, as the high laser powers of more than 100 μW that are necessary to resolve these modes lead to excessive heating, which exceeds the ADR's cooling power.

The quality factor of the fundamental mode can be measured at even lower temperatures, as laser powers below 30 μW are sufficient to resolve this resonance with a decent signal to noise ratio, see Fig. 2.2b. The extracted quality factor is $(498 \pm 11) \cdot 10^3$ at 1 K, while at 450 mK the same mode has a Q of $(483 \pm 13) \cdot 10^3$.

Apart from the lack of cooling power at temperatures below 4 K, other problems make reliable long-term optical measurements in this cryostat quite difficult: The lower part of the insert, onto which the sample is mounted, is connected to the upper part, supporting the positioner with the attached glass fiber, via three thin stainless steel tubes. Furthermore, the low-temperature stage is solely suspended from thin pieces of plastic twine to achieve a sufficient thermal insulation between the different stages of the cryostat. The forces exerted onto the paramagnetic salt (and maybe small ferromagnetic parts in the cryostat) upon any change in the magnetic field lead to large displacements between sample and fiber tip in the range of several μm, which occur as large, sudden jumps as well as slow drifts. The thermal expansion and contraction of the different parts of

the cryostat also leads to slow drifts of the position. These effects make it necessary to constantly adjust the fiber position, which makes it impossible to average the signal or conduct longer measurements. The sudden jumps destroyed quite a few samples and fibers used in the experiments, as the jump can be larger than the distance between the lensed fiber and the chip, crashing the fiber onto the chip surface.

To systematically measure the temperature dependence of the mechanical quality factor, another detection scheme, which does not need any adjustments and works independent of temperature is necessary. The next chapter describes such a detection technique using the on-chip electrodes and a separate microwave resonator to implement a completely electrical measurement.

Chapter 3

Heterodyne microwave detection

In the previous chapter, the motion of the mechanical resonator is detected using fiber-optical interferometry [Aza07], where the interference between the reflection signal of the substrate and the beam leads to a modulation of the reflected light. The advantages of this technique include a high sensitivity and a rather simple setup, furthermore it works with any sample geometry and does not require additional processing steps when fabricating the resonators. The big disadvantage, along with other optical techiques [Rug89, Kar05], is the need for precise and stable relative positioning of sample and optics.

There are numerous other detection schemes which do not rely on optical techniques, and directly generate electrical signals. Examples include the magnetomotive detection [Cle96], where the Lorentz force creates an alternating current in a vibrating, conductive beam, piezolelectric transduction [Mas07, Mah08] using resonators made of a suitable material, and capacitive techniques [Kno03, Koz06], which require a side electrode next to the metalized beam to form a capacitor with a modulated electrode separation. All of these nanomechanical detection schemes require at least a partial metallization of the resonator structure, which, at least at room temperature, induces additional losses [Sek02, Yu12]. Apart from that, the mechanical response of such a two-layer system is much harder to model, complicating theoretical predictions of the resonant properties.

The dielectric driving scheme can be reversed to be used as a detection mechanism [Unt09]: The two side electrodes form a capacitor with a dielectric object (the resonator) oscillating in its inhomogeneous field, thus modulating the capacitance. However, the signal generated this way is rather weak, and is superimposed by strong crosstalk if a resonant electrical actuation is used.

Both of these drawbacks can be overcome by a heterodyne measurement in which the weak signal is not measured directly, but is instead used to modulate the response of a higher-frequency resonator, which can then be read out with high sensitivity. This is commonly used in cavity optomechanics [Met04, Arc06, Gig06, Kle06, Tho08, Sch08, Ane09], where the resonance frequency of an optical cavity is coupled to the displacement of a mechanical resonator, often realized by using the mechanical structure as one of the

end mirrors of the cavity. A very similar concept is the capacitive coupling of the displacement of a mechanical resonator to an electrical cavity, which is usually performed using superconducting resonators at cryogenic temperatures [Reg08, Sil09, Roc10, Teu11].

As we want to use the dielectric coupling to a microwave resonator at room temperature, we can not employ superconducting resonators but instead have to rely on a resonant structure made from copper. Two factors are important for the choice of the right cavity design: The internal losses of the cavity should be as low as possible, as the detection signal at a constant probe power scales with the square of the cavity quality factor [Teu09]. Additionally, easy access to the electric field of the cavity is necessary, as the on-chip electrodes need to be connected to the cavity. The second criteria favors a microstrip resonator over larger 3D cavities with higher quality factors. It consists of a small copper strip on a dielectric substrate. One end of the strip is grounded, it thus supports a $\lambda/4$ mode with the maximal electric field at the open end, which allows a very easy connection to the on-chip electrodes via a bond wire. The back side of the substrate is covered by a uniform copper layer serving as a ground plane.

The room-temperature operation of the detection scheme requires the use of a different substrate material for the mechanical resonator chip. The thermally activated charge carriers in the previously used silicon substrates lead to a strong damping of the microwave resonance via ohmic losses, an effect which only vanishes at temperatures below approximately 60 K [Kre11]. Thus, insulating fused silica wafers, coated with a 100 nm thick silicon nitride layer, were used to fabricate the mechanical resonators (see appendix B).

The successful implementation of this dielectric detection scheme is described in the following chapter 3.1, including the "opto"mechanical effects induced by the cavity backaction on the mechanical resonator [Mar07, Teu08]. This provides control over the mechanical quality factor by detuning the microwave pump frequency from the resonance frequency of the cavity, which leads to the generation or anihilation of phonons in the mechanical modes. The effect can even be used to enter the regime of cavity-induced self-oscillation, resulting in an effective mechanical quality factor of over one million. The backaction effects are explained in more detail in chapter 3.1.1, which also presents the calculation of the displacement sensitivity of the detection scheme and the mass sensitivity of the resonator.

When the side electrodes are used for heterodyne detection in the way described in chapter 3.1, they can not simultaneously be used to dielectrically actuate the beam. Thus we either relied on a piezo actuator or pumped the mechanical motion via the cavity. A simple modification allows to apply dc and rf voltages to the side electrodes while also using them to detect the beam's motion. The addition of a small capacitor provides a ground path for the microwave signals while the driving signal can be applied to the electrodes at the same time. It turns out that the application of a dc voltage not only changes the spring constant and thus resonance frequency of the beam via the force gradient created by the inhomogeneous electric field. The re-orientation of the microscopic dipoles inside the dielectric material, caused by the different electric fields at different positions during

one oscillation cycle, also causes dielectric losses in the resonator. The combination of both effects allows to extract the complex polarizability of the material from its resonant properties. Both results are presented in chapter 3.2. Furthermore, the exact position of the electrodes relative to the beam influences the tuning behaviour of the modes. The tuning direction of the out-of-plane mode can be inverted if the electrodes are situated below and not above the beam, which can also be reproduced by finite element simulations in *COMSOL Multiphysics*. This is also discussed in chapter 3.2.

3.1 Microwave cavity-enhanced transduction for plug and play nanomechanics at room temperature

Published as *Nature Communications* **3**, 728 (2012), reference [Fau12a].

nature COMMUNICATIONS

OPEN

ARTICLE

Received 6 Sep 2011 | Accepted 2 Feb 2012 | Published 6 Mar 2012

DOI: 10.1038/ncomms1723

Microwave cavity-enhanced transduction for plug and play nanomechanics at room temperature

T. Faust[1], P. Krenn[1], S. Manus[1], J.P. Kotthaus[1] & E.M. Weig[1]

Following recent insights into energy storage and loss mechanisms in nanoelectromechanical systems (NEMS), nanomechanical resonators with increasingly high quality factors are possible. Consequently, efficient, non-dissipative transduction schemes are required to avoid the dominating influence of coupling losses. Here we present an integrated NEMS transducer based on a microwave cavity dielectrically coupled to an array of doubly clamped pre-stressed silicon nitride beam resonators. This cavity-enhanced detection scheme allows resolving of the resonators' Brownian motion at room temperature while preserving their high mechanical quality factor of 290,000 at 6.6 MHz. Furthermore, our approach constitutes an 'opto'-mechanical system in which backaction effects of the microwave field are employed to alter the effective damping of the resonators. In particular, cavity-pumped self-oscillation yields a linewidth of only 5 Hz. Thereby, an adjustement-free, all-integrated and self-driven nanoelectromechanical resonator array interfaced by just two microwave connectors is realised, which is potentially useful for applications in sensing and signal processing.

[1] Center for NanoScience (CeNS) and Fakultät für Physik, Ludwig-Maximilians-Universität, Geschwister-Scholl-Platz 1, München 80539, Germany. Correspondence and requests for materials should be addressed to E.M.W. (email: weig@lmu.de).

The increasing importance of nanomechanical resonators for both fundamental experiments[1–3] and sensing applications[4,5] in recent years is a direct consequence of their high resonance frequencies as well as low masses. However, because of their small size, they couple only weakly to their environment, which can make it difficult to efficiently transduce their motion. This coupling can be strongly enhanced via an optical[6–11] or electrical microwave[12–17] cavity. While both methods enable sensitive displacement detection, only the latter is suitable for large-scale integration of many resonators with a single cavity. Up to now, nanoelectromechanical transduction via microwave cavities is predominantly performed at cryogenic temperatures to benefit from superconducting cavities capacitively coupled to superconducting mechanical resonators. With a main focus on quantum mechanical ground state cooling[2], the potential of cavity nanoelectromechanical systems (NEMS) for integrated transduction at room temperature is yet to be exploited.

To this end, we present an approach based on a copper microstrip cavity operating at 300 K. While previous works[12–16] relied on capacitive coupling between cavity and metallized resonator, we employ a dielectric resonator made of highly stressed silicon nitride. This avoids additional damping by losses in the metallization layer, which frequently is one of the dominating sources of dissipation at room temperature[18,19]. For transduction, we take advantage of dielectric gradient forces, which are becoming more and more established as a powerful tool to control NEMS[20–23]: if a dielectric beam is placed in between two vertically offset electrodes, its vibration will induce a periodic modulation of their mutual capacitance. We demonstrate that this modulation alters the response of a connected microwave cavity, which can be demodulated to probe the displacement of the nanomechanical resonator. The resulting heterodyne cavity-enhanced detection scheme allows probing of the resonator's Brownian motion with a sensitivity of presently 4.4 pm/$\sqrt{\text{Hz}}$ at 300 K. We have tested the scheme to operate at temperatures between 300 K and low temperatures (4 K), at which superconducting cavities become superior. Furthermore, the coupled cavity-resonator device is a microwave analogy of an optomechanical system: cavity electromechanics can be employed to amplify or damp the mechanical vibration utilizing the dynamical backaction of the microwave field. By strongly amplifying the motion, the regime of cavity-pumped self-oscillation is reached. The resulting high-amplitude, narrow-band signal with a linewidth of only 5 Hz can be used to track the resonance frequency of the beam, yielding an estimated mass resolution of about 10^{-18} g.

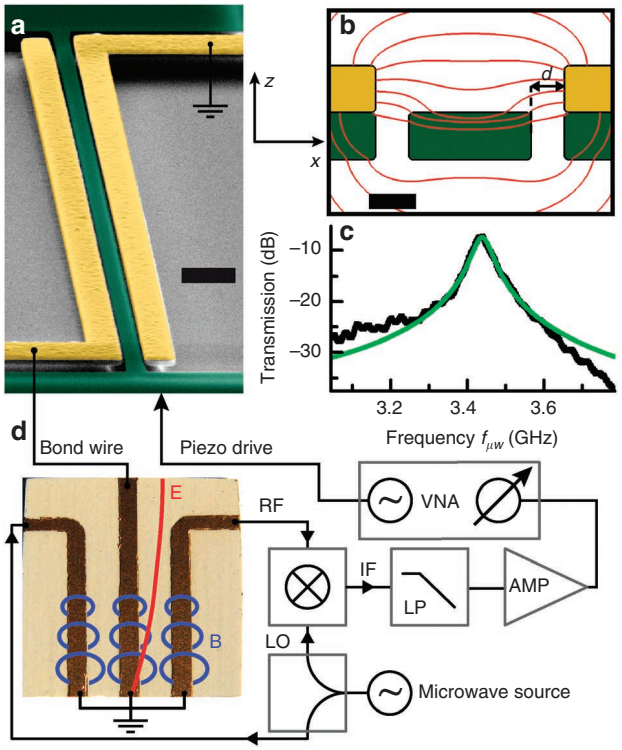

Figure 1 | Sample and setup. a shows a scanning electron micrograph of the 55 mm long silicon nitride beam (green) flanked by two gold electrodes (yellow). Scale bar corresponds to 1 μm. The schematic cross-section of the beam and electrodes in **b** (scale bar corresponds to 100 nm) exhibits a symmetric gap of $d = 60$ nm and includes simulated electric field lines. The beam is placed just below the electrodes, where its movement in the z direction induces the largest modulation of the capacitance. The electrodes are connected to an electrical $\lambda/4$ microwave cavity via bond wires. **c** depicts its transmission spectrum (black) with a Lorentzian fit (green). The schematic circuit diagram shown in **d** includes a photo of the cavity circuit board (8×8 mm^2). It also illustrates magnetic field lines (blue) indicating the inductive coupling between the two side electrodes and the central resonator, and the electric field distribution (red) in the resonator. The cavity is pumped by a microwave source, the radio frequency transmission signal is mixed with a reference signal (LO) such that the mechanical sidebands (IF) are demodulated. A lowpass filter (LP) is used to remove higher-frequency components, and the amplified (AMP) sideband signal is fed to a vector network analyser (VNA), which can also drive a piezo to actuate the beam. See Fig. 5 and Methods for the detailed circuit.

Results

Device and measurement setup. Arrays of mechanical beam resonators of different length are fabricated out of a 100-nm-thick pre-stressed silicon nitride film deposited on a fused silica wafer (see Fig. 1a for one element as well as Methods and Supplementary Fig. S1). Each nanomechanical resonator is embedded in a capacitive structure, which is part of the resonant LC circuit as sketched in Fig. 1a,b and c,d, respectively. One of the electrodes is connected to an external $\lambda/4$ microstrip cavity (see Fig. 1d and Methods) with a resonance frequency of $f_c = 3.44$ GHz and a quality factor of 70, the transmission of which is shown in Fig. 1c. In contrast to the more common SiN films on silicon substrates, SiN on fused silica avoids room temperature dissipation of microwave signals by mobile charge carriers and generates an even higher tensile stress in the SiN film[24]. Measuring the resonance frequencies of several harmonic modes and fitting these with a simple theoretical model[25] yields a beam stress of 1.46 ± 0.03 GPa. Recently, it has been demonstrated that the tensile stress in a nanomechanical resonator enhances its eigenfrequency and quality factor[25,26]. Thus, the observed quality factors are higher than the ones measured with resonators of the same eigenfrequency on a silicon substrate with a prestress of 0.83 GPa, and beams of the same length have higher resonance frequencies. Whereas the described scheme has been employed on a range of microwave cavities and nanomechanical resonator arrays, all measurements shown here have been performed on one 55 μm long beam with a fundamental mechanical resonance frequency of $f_m = 6.6$ MHz and a room temperature quality factor $Q_m = 290{,}000$.

By coupling the mechanical resonator to the microwave cavity, the electrical resonance frequency f_c is periodically modulated, causing sidebands at $f_c \pm f_m$ in the microwave transmission signal. These are demodulated, filtered and amplified (see Fig. 1d, Fig. 5 and Methods), then fed directly into a vector network analyser, the output of which can be used to excite the mechanical resonator via a piezo inertial drive[26]. The resonator chip, glued onto the piezo transducer, as well as the cavity are operated in a vacuum chamber at pressures below 5×10^{-4} mbar at room temperature.

Detection. The amplitude of the piezo-driven mechanical resonator (Fig. 2a) is probed by monitoring the sideband signal via the

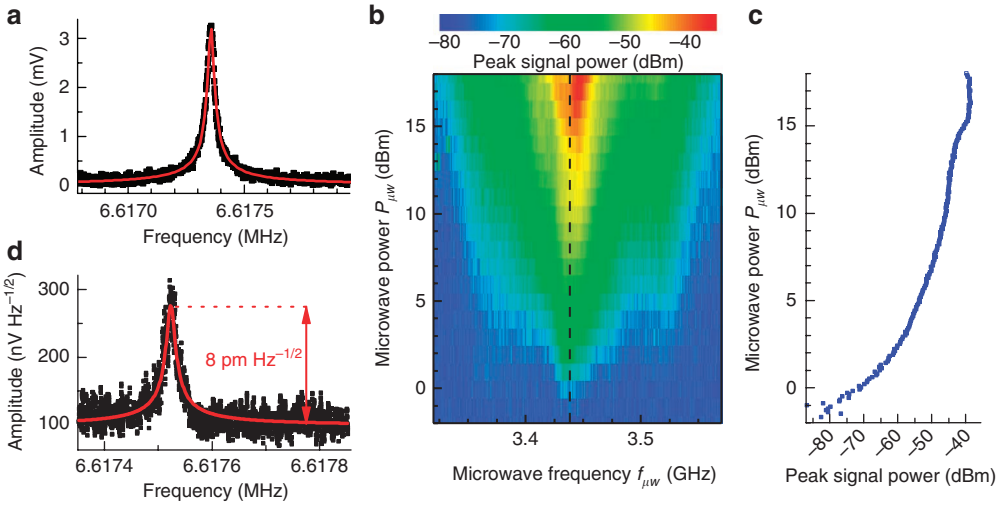

Figure 2 | Detection. The driven response of the 55 μm long beam is shown in **a**. It is vibrating with an amplitude of about 6 nm at a piezo-driving power of −70 dBm measured with a microwave power of $P_{\mu w}$ = 18 dBm at $f_{\mu w}$ = 3.44 GHz. To determine the operating regime of the detection scheme as a function of the cavity parameters, microwave frequency and power are systematically varied and the mechanical peak signal power reflecting the squared resonance amplitude (that is, the maximum of the resonance in **a**) is plotted in **b** for each point. A cut along the microwave cavity resonance (dashed line in **b**) shown in **c** depicts that the detected signal is maximized at cavity powers between 15 and 18 dBm. The Brownian motion of the resonator in **d** is employed to deduce the sensitivity of the detection scheme from the noise floor.

demodulated microwave transmission signal. Note that all amplitudes in this work are given as half-peak-to-peak values. A Lorentzian fit is used to extract the mechanical resonance amplitude, which depends on the output power $P_{\mu w}$ and frequency $f_{\mu w}$ of the microwave source. Figure 2b shows how the operating range of the detection mechanism can be mapped out by systematically varying the microwave parameters. The plot displays the colour-coded peak signal power of the mechanical spectrum, plotted for every set of $P_{\mu w}$ and $f_{\mu w}$. Maximum sensitivity is achieved on resonance with the microwave cavity (at $f_{\mu w}=f_c=3.44$ GHz, dashed line), where the cavity field and its sensitivity to frequency changes are maximized. The peak signal power in Fig. 2c is directly proportional to the microwave power at low levels, but nonlinear effects in the cavity cause the detection efficiency to level off above $P_{\mu w}=15$ dBm. Using the optimal operating point of $f_{\mu w}=f_c$ and $P_{\mu w}=18$ dBm, the thermally induced Brownian motion of the resonator can be easily resolved, as depicted in Fig. 2d. By calculating the thermal amplitude of the beam to be 8 pm/$\sqrt{\text{Hz}}$ at room temperature, the observed noise level corresponds to a sensitivity of 4.4 pm/$\sqrt{\text{Hz}}$ (see also Supplementary Methods). Thus, the full dynamic range of the resonator is accessible as the detection scheme allows to characterize the resonator response from the thermal motion until the onset of nonlinear behaviour.

As the detected signal is only proportional to the change in capacitance dC/dz caused by a displacement dz and other geometrical parameters, the displacement sensitivity is independent of the mechanical frequency. However, higher-frequency beams imply a reduced electrode length and thus weaker coupling for constant cross-section of the detection capacitor. The same applies to higher harmonic modes, where only one antinode of odd harmonic modes generates a signal, as the other antinodes cancel each other. This results in a $1/f$ scaling of the sensitivity in the case of a stressed string, as observed in other measurements for beams with frequencies between 6 and 60 MHz.

Furthermore, even the in-plane motion of the beam can be detected (not shown). Considering the electrode geometry displayed in Fig. 1b, this seems to be suprising at first. Ideally, the capacitance gradient dC/dx is a parabola such that both a displacement of the beam in positive and negative x direction increases the capacitance symmetrically. Thus, there should be no signal on the resonance frequency of the mode. But even small imperfections during sample fabrication lead to a slightly off-centre position of the beam and thereby a non-zero capacitance gradient in the x direction. Therefore, in-plane modes are accessible, albeit with a lower sensitivity such that the Brownian motion cannot be resolved.

Backaction effects. For a detuned microwave cavity, the coupling between the cavity and the mechanical resonator gives rise to 'opto'-mechanical effects such as backaction cooling and pumping of the mechanical mode[2,3,6–12,16,17,27,28]. The signature of these cavity electromechanical effects can already be discerned in the red portion of Fig. 2b and is shown more clearly in Fig. 3. Comparison of the different mechanical resonance curves obtained for negative, positive and no detuning (inset of Fig. 3a) shows that both the resonance amplitudes (Fig. 3a) and the measured, effective $Q(\Delta)$ (Fig. 3b, see Supplementary Methods) change with detuning. If the detuning $\Delta=f_{\mu w}-f_c$ between microwave drive and cavity resonance frequency is negative (red detuned), the electrical force produced by the cavity field counteracts the vibrational motion, thereby decreasing its amplitude. For positive (blue) detuning, the amplitude is increased. As the resonance amplitude depicted in Fig. 3a is superimposed with the detuning-dependent sensitivity curve discussed in Fig. 2b and therefore distorted, we rather use the detuning dependence of the quality factor to analyse the data.

The effective $Q(\Delta)$ in Fig. 3b clearly shows the expected behaviour: at negative detuning, the additional cavity-induced damping $\Gamma(\Delta)$ is positive, such that the effective damping exceeds the intrinsic value and $Q(\Delta)$ decreases, whereas at positive detuning the opposite occurs, with an optimal detuning of $|\Delta_{opt}|=9$ MHz. Fitting the theoretical model (refs 27–29 and Supplementary Methods) to the data measured at several cavity drive powers allows to extract the average coupling factor $g=\partial f_c/\partial z=75\pm5$ Hz/nm. The backaction effect is independent of piezo-driven beam actuation as only the effective damping is changed. This is confirmed by repeating the experiment without piezo actuation (inset of Fig. 3b). A comparison between the weakly driven situation depicted in Fig. 3b and the Brownian motion in the inset only shows a significant increase of the noise in the latter case. Therefore, all measurements in Figs 3 and 4a

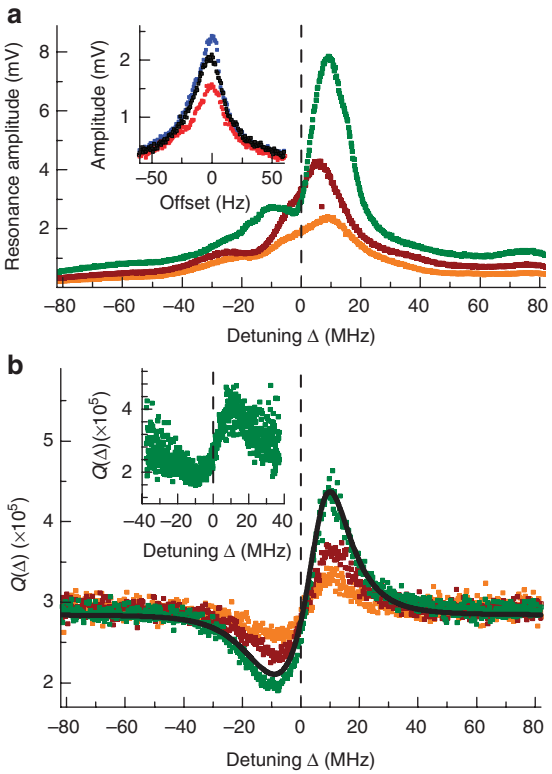

Figure 3 | Cavity electromechanics. Resonance amplitude and quality factor of the weakly driven (piezo power of −70 dBm) mechanical mode are increased or decreased depending on the microwave detuning $\Delta = f_{\mu w} - f_c$ due to the backaction of the microwave field on the resonator. This is shown in the inset of **a**, comparing resonance curves of the same resonance at a microwave power of 12 dBm for red, blue or no (red, blue and black points, respectively) detuning. For clarity, the resonance curves have been plotted versus the frequency offset to the respective (detuning-dependent) resonance frequency. Panel **a** shows the detuning dependence of the resonance amplitude (that is, maximum in inset) for different microwave powers of 18, 15 and 12 dBm (green, red and orange dots). In **b**, the detuning dependence of the quality factor for the same power values is depicted, along with a fit to the theoretical model (black line, see Supplementary Methods). The inset of **b** shows the quality factor of the Brownian motion versus detuning at 18 dBm microwave power with identical axes, the only difference to the main plot is the better signal to noise ratio in the weakly driven case.

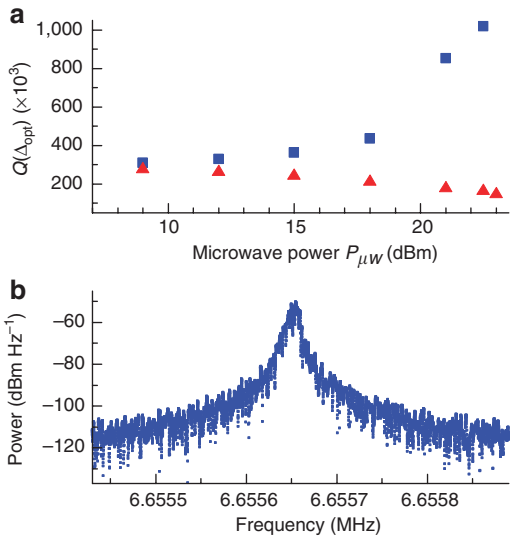

Figure 4 | Cavity-induced damping and self-oscillation. Using a blue-detuned (red-detuned) cavity drive, the amplitude of the beam can be amplified (damped). This effect is controlled by the microwave power $P_{\mu w}$, as shown in **a** (blue squares: blue detuning, red triangles: red detuning) for the optimal Δ_{opt} of ±9 MHz. By increasing the microwave power to 23 dBm, the backaction gain caused by the blue-detuned cavity exceeds the intrinsic damping, and self-oscillation occurs. The respective power spectrum in **b** shows a linewidth reduced to 5 Hz.

(except the inset in Fig. 3b) were done with a weak piezo actuation of −70 dBm to operate with an improved signal to noise ratio.

Increasing the microwave power to 23 dBm, the quality factor can be decreased to half its initial value with a negative Δ as shown in Fig. 4a, corresponding to an effective mode temperature of 150 K (ref. 6). For positive Δ, the quality factor diverges. This reflects cavity-driven self-oscillation of the beam, once the intrinsic damping is cancelled by the cavity backaction. The power spectrum of this oscillation is shown in Fig. 4b. Its linewidth of 5 Hz, corresponding to an effective quality factor[30] of 1.3 million, is limited by the stability of the oscillation frequency, which is mainly affected by fluctuations of the cavity drive.

This ultra-low linewidth is ideally suited for mass-sensing applications, giving rise to an estimated mass resolution of about 10^{-18} g (see Supplementary Methods). In contrast to single carbon nanotubes, which have been employed to probe masses of 10^{-22} g (refs 4,5), the presented scheme can readily be scaled up to a large-scale fabrication process involving many beams. Further improvements can be expected by increasing the electromechanical coupling constant[2,13]. This can be achieved by a reduced gap size in the detection capacitor. Beam–electrode separations of 20 nm have already been demonstrated[15], which should yield a tenfold increase in coupling.

Besides the backaction effects, there is a quasistatic electric force acting on the resonator[21]. The electric microwave field between the electrodes polarizes the dielectric beam, creating dipoles that are attracted to high electric fields. This leads to an additional effective spring constant that scales with the square of the field (that is, with $P_{\mu w}$) and leads to an increased (decreased) restoring force for the out-of-plane (in-plane) mode. The resulting difference in resonance frequency is clearly visible comparing Fig. 2a ($P_{\mu w} = 18$ dBm) to Fig. 4b ($P_{\mu w} = 23$ dBm) and can be employed to tune the mechanical eigenfrequency.

Discussion

There are only a few existing nanomechanical transduction schemes at room temperature providing good integration and scalability to large resonator arrays coupled to a single readout cavity: photonic circuits[31–33] offer extremely large displacement sensitivities, but are limited by the precise alignment of external components and thus sensitive to vibrations. On the other hand, adjustment-free schemes such as piezoelectric transduction[34] or capacitive detection[13,35], which, in addition, frequently require cryogenics, impose material constraints and can cause additional dissipation[18,19]. In contrast, the presented dielectric coupling of the nanomechanical resonator to the microwave cavity allows to maintain a large quality factor over a wide temperature range (tested between 4 and 300 K). Accordingly, the reported room temperature Q_m of 290,000 of the prestressed SiN-on-fused-silica nanoresonator is, to our knowledge, the highest ever obtained in this frequency range.

In conclusion, we present a room temperature platform for the sensitive readout, actuation and tuning of nanomechanical resonators. We achieve a sensitivity well below the Brownian motion for the fully integrable and robust heterodyne readout of a nanomechanical resonator via a weakly coupled microwave cavity ($g = \partial f_c / \partial z = 75 \pm 5$ Hz/nm). This coupling constant is significantly smaller than the one obtained with capacitively coupled

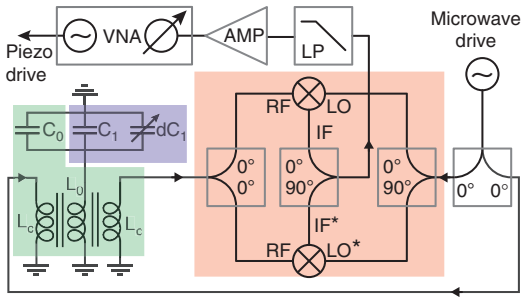

Figure 5 | Detailed electrical schematic. Detailed version of Fig. 1d showing an electrical equivalent circuit of the microwave cavity (green box) coupled to the resonator chip (blue box) and the complete IQ mixing circuit (red box). The two signal paths offset by 90° are denoted LO/IF and LO*/IF*, respectively.

beams[13] but requires neither cryogenics nor beam metallization. The relative cavity frequency shift g/f_c is comparable to typical optical experiments[22,36], as not only the coupling constant g but also the cavity resonance frequency f_c are orders of magnitude smaller in the microwave regime.

A major advantage of the presented scheme is the parallel readout of many beams and many modes (higher harmonics as well as in- and out-of-plane) using only a single microwave setup. Additionally, the cavity backaction can be used to control the amplitude of the resonator, thus allowing to omit the piezo actuator. By entering the regime of cavity-pumped self-oscillation a strong and narrowband signal is generated, perfectly suited for sensing applications requiring a simple resonance frequency readout. As both resonator and cavity are fabricated reproducibly using standard lithographic processes, inexpensive plug and play NEMS sensor modules using only two microwave connectors to interface them with control electronics can be developed.

Methods

Microwave setup. The microwave cavity is fabricated on a ceramic substrate suitable for high-frequency applications (Rogers TMM10) cut to small chips. Standard optical lithography and wet etch processes are employed to pattern the 17 μm thick top copper layer, onto which a 150 nm gold coating is evaporated to avoid corrosion.

The design of the microwave cavity shown in Fig. 1d consists of an 8 mm long and 0.64 mm wide centre strip that forms the actual λ/4 resonator. One end of the strip is grounded, while its other end is connected to the silica chip carrying the mechanical resonators. Two adjacent strips near the grounded end are used to inductively couple the cavity to the feed lines and measure the transmission signal. We chose inductive coupling to separate the interface to the chip at the open end from the interface to the feed lines at the grounded end of the λ/4 resonator. The length of the two feed lines (6 mm) and the distance between the striplines (1.2 mm) were optimized using high-frequency circuit simulations with APLAC for a tradeoff between transmission and quality factor of the cavity.

Figure 5 shows a detailed version of the simplified electrical circuit depicted in Fig. 1d. On the left, the electrical equivalent circuit of the λ/4 microstrip cavity including both feed lines and the coupling to the chip is depicted. The actual cavity consists of the inductance L_0 of the 8 mm long copper strip and its capacitance C_0 to the ground plane on the bottom of the circuit board. The inductive coupling between L_0 and the two feed lines with inductances L_c provides the external interface to the cavity. The resonator chip is connected to the open end of the cavity, it adds a static capacitance C_1 and a time-dependent contribution $dC_1(t)$, which oscillates with the actual beam displacement. A very rough estimate for L_0 and C_0 can be obtained from microstrip theory, giving values of 1 pF and 3 μH (this would result in $f_c = 1/(2\pi\sqrt{L_0C_0}) = 2.9$ GHz), neglecting the effects of the microstrip ends. As the resonance frequency of the bare microwave cavity is about 5% higher than with the bond wire and chip connected, C_1 must be $<10\%$ of C_0, as the bond wire also adds some inductance to the circuit.

A microwave tone is applied to one port of the cavity, thus creating a phase-modulated signal at the other port of the cavity caused by the alternating capacitance dC_1. As the transmission through the cavity also adds some detuning-dependent phase to the microwave tone, directly mixing the cavity output with the drive tone would result in a detuning-dependent phase difference between the two signals. This difference would need to be compensated for by an additional phase shifter, which had to be adjusted for maximum signal at every drive frequency. To avoid this tedious procedure, we use an IQ (in-phase/quadrature) mixer shown in the red box in Fig. 5. It consists of a 0°/0° and a 0°/90° power splitter as well as two mixers. The reference signal coming from the microwave generator is split into two parts with a 90° phase shift to each other. By mixing these two signals (LO and LO*) with the radio frequency transmission signal of the cavity, two intermediate frequency signals (IF and IF*) are created. Depending on the phase of the two input signals of the IQ mixer, at least one of these signals is always non-zero, and their (phase-correct) sum is completely independent of the phase relation of the input signals. Thus, by combining the two demodulated quadrature components with another 0°/90° power splitter and blocking the higher-frequency mixing products, amplitude and phase of the mechanical signal are reconstructed.

The noise background of this signal is primarily caused by the phase noise of the frequency generator driving the electrical cavity, causing more background noise with increasing power. Therefore, we use a Rohde and Schwarz SMA100A signal generator with extremely low phase noise below −150 dBc at 10 MHz offset. In order to preserve the low noise level, the demodulated sidebands are amplified with a 35 dB preamplifier with a noise figure of 1.3 dB. The output of this amplifier is either directly connected to a spectrum analyser (to quantify the Brownian motion) or amplified by another 30 dB and fed to a network analyser (in case of the driven measurements).

Resonator fabrication. The samples are fabricated on 500 μm thick fused silica wafers, which are coated with a 100 nm thick commercial high-quality LPCVD layer of pre-stressed silicon nitride. Large chips of size 5×5 mm^2 are cut from the wafer. To enable electron beam lithography on these non-conductive substrates, 2 nm of chromium is evaporated onto the PMMA resist before exposure and removed before developing. E-beam lithography and standard lift-off processes are used to define the gold electrodes and a thin cobalt etch mask protecting the beams. The subsequent inductively coupled plasma reactive ion etch using SF_6 and Ar removes the silicon nitride which is not protected by a metal layer. The final hydrofluoric acid wet etch removes the cobalt and releases the beams, while the gold electrodes use chromium as an adhesion layer and are not attacked by the acid. Finally, the chips are blow-dried with nitrogen, glued to the piezo and a wire bonder is used to connect them to the microwave cavity. All these processing steps use industry-standard techniques, so a large-scale fabrication of inexpensive sensor modules should be within reach.

Each mechanical resonator chip contains multiple beams with their respective electrodes, all shunted between two bond pads that are used to connect the chip to the microwave cavity. One design with big variations in the beam length is shown in Supplementary Fig. S1. It is also possible to use designs with very small length differences in the order of 100 nm, allowing to address many mechanical resonances by frequency division multiplexing in a narrow frequency band.

Resonator chip design. In order to choose the sample design with the highest coupling between the electrical cavity and the mechanical resonator, several simulations of the electrode configuration using COMSOL Multiphysics were conducted. The electrodes were patterned directly onto the SiN film to induce a maximal capacitance variation with beam displacement. We decided to put the gold electrodes on top of the silicon nitride layer and thereby deposit them before the reactive ion etch step, in contrast to our earlier designs where the gold was evaporated onto the remaining silicon dioxide covering the silicon substrate below the resonator[21]. In these previous designs, the vertical separation between the beam and the silicon dioxide layer had to exceed 250 nm to achieve sufficient underetching of the beam. Thus the new design allows for much smaller overall beam–electrode separations, resulting in a larger effect of the beam motion on the capacitance. Further simulations with this principal geometry varied several other parameters. These primarily show an $1/d$ scaling between the lateral beam–electrode distance d (see Fig. 1b) and the capacitance change per nanometre beam displacement, as expected for a capacitive interaction.

As the beams tend to stick to the side electrodes at very low gap sizes, the fabrication of smaller defect-free gaps by conventional scanning electron microscopy lithography and dry and wet etching was not successful. We have investigated devices with gap widths varying between 110 nm and 60 nm. Supplementary Figure S2 shows the coupling strength (black squares) extracted from the quality factor versus microwave frequency curves, as shown in Fig. 3b, for different values of d. The dotted red curve depicts the capacitance gradients obtained from the simulation multiplied with a scaling factor to fit the measured coupling strength. The dependence of the coupling strength on the gap size in the measurements is qualitatively reproduced by the simulations.

References

1. O'Connell, A. D. *et al.* Quantum ground state and single-phonon control of a mechanical resonator. *Nature* **464,** 697–703 (2010).
2. Teufel, J. D. *et al.* Sideband cooling of micromechanical motion to the quantum ground state. *Nature* **475,** 359–363 (2011).
3. Chan, J. *et al.* Laser cooling of a nanomechanical oscillator into its quantum ground state. *Nature* **478,** 89–92 (2011).
4. Lassagne, B., Garcia-Sanchez, D., Aguasca, A. & Bachtold, A. Ultrasensitive mass sensing with a nanotube electromechanical resonator. *Nano Lett.* **8,** 3735–3738 (2008).

5. Jensen, K., Kim, K. & Zettl, A. An atomic-resolution nanomechanical mass sensor. *Nat. Nano.* **3,** 533 (2008).
6. Metzger, C. H. & Karrai, K. Cavity cooling of a microlever. *Nature* **432,** 1002–1005 (2004).
7. Gigan, S. *et al.* Self-cooling of a micromirror by radiation pressure. *Nature* **444,** 67–70 (2006).
8. Arcizet, O., Cohadon, P.- F., Briant, T., Pinard, M. & Heidmann, A. Radiation-pressure cooling and optomechanical instability of a micromirror. *Nature* **444,** 71–74 (2006).
9. Kleckner, D. & Bouwmeester, D. Sub-kelvin optical cooling of a micromechanical resonator. *Nature* **444,** 75–78 (2006).
10. Schliesser, A., Riviere, R., Anetsberger, G., Arcizet, O. & Kippenberg, T. J. Resolved-sideband cooling of a micromechanical oscillator. *Nat. Phys.* **4,** 415–419 (2008).
11. Eichenfield, M., Camacho, R., Chan, J., Vahala, K. J. & Painter, O. A picogram- and nanometre-scale photonic-crystal optomechanical cavity. *Nature* **459,** 550–555 (2009).
12. Brown, K. R. *et al.* Passive cooling of a micromechanical oscillator with a resonant electric circuit. *Phys. Rev. Lett.* **99,** 137205 (2007).
13. Regal, C. A., Teufel, J. D. & Lehnert, K. W. Measuring nanomechanical motion with a microwave cavity interferometer. *Nat. Phys.* **4,** 555–560 (2008).
14. Sillanpää, M. A., Sarkar, J., Sulkko, J., Muhonen, J. & Hakonen, P. J. Accessing nanomechanical resonators via a fast microwave circuit. *Appl. Phys. Lett.* **95,** 011909 (2009).
15. Sulkko, J. *et al.* Strong gate coupling of high-q nanomechanical resonators. *Nano Lett.* **10,** 4884–4889 (2010).
16. Rocheleau, T. *et al.* Preparation and detection of a mechanical resonator near the ground state of motion. *Nature* **463,** 72–75 (2010).
17. Hao, L., Gallop, J. C. & Cox, D. Excitation, detection, and passive cooling of a micromechanical cantilever using near-field of a microwave resonator. *Appl. Phys. Lett.* **95,** 113501 (2009).
18. Sekaric, L., Carr, D. W., Evoy, S., Parpia, J. M. & Craighead, H. G. Nanomechanical resonant structures in silicon nitride: fabrication, operation and dissipation issues. *Sens. Actuators A: Phys.* **101,** 215–219 (2002).
19. Yu, P.- L., Purdy, T. P. & Regal, C. A. Control of material damping in high-Q membrane microresonators. Preprint at http://arxiv.org/abs/1111.170 (2011).
20. Schmid, S., Wendlandt, M., Junker, D. & Hierold, C. Nonconductive polymer microresonators actuated by the kelvin polarization force. *Appl. Phys. Lett.* **89,** 163506 (2006).
21. Unterreithmeier, Q. P., Weig, E. M. & Kotthaus, J. P. Universal transduction scheme for nanomechanical systems based on dielectric forces. *Nature* **458,** 1001–1004 (2009).
22. Anetsberger, G. *et al.* Near-field cavity optomechanics with nanomechanical oscillators. *Nat. Phys.* **5,** 909–914 (2009).
23. McRae, T. G., Lee, K. H., Harris, G. I., Knittel, J. & Bowen, W. P. Cavity optoelectromechanical system combining strong electrical actuation with ultrasensitive transduction. *Phys. Rev. A* **82,** 023825 (2010).
24. Retajczyk, T. F. & Sinha, A. K. Elastic stiffness and thermal expansion coefficients of various refractory silicides and silicon nitride films. *Thin Solid Films* **70,** 241–247 (1980).
25. Unterreithmeier, Q. P., Faust, T. & Kotthaus, J. P. Damping of nanomechanical resonators. *Phys. Rev. Lett.* **105,** 027205 (2010).
26. Verbridge, S. S., Parpia, J. M., Reichenbach, R. B., Bellan, L. M. & Craighead, H. G. High quality factor resonance at room temperature with nanostrings under high tensile stress. *J. Appl. Phys.* **99,** 124304 (2006).
27. Marquardt, F., Chen, J. P., Clerk, A. A. & Girvin, S. M. Quantum theory of cavity-assisted sideband cooling of mechanical motion. *Phys. Rev. Lett.* **99,** 093902 (2007).
28. Teufel, J. D., Regal, C. A. & Lehnert, K. W. Prospects for cooling nanomechanical motion by coupling to a superconducting microwave resonator. *New J. Phys.* **10,** 095002 (2008).
29. Clerk, A. A., Devoret, M. H., Girvin, S. M., Marquardt, F. & Schoelkopf, R. J. Introduction to quantum noise, measurement, and amplification. *Rev. Mod. Phys.* **82,** 1155–1208 (2010).
30. Feng, X. L., White, C. J., Hajimiri, A. & Roukes, M. L. A self-sustaining ultrahigh-frequency nanoelectromechanical oscillator. *Nat. Nano* **3,** 342 (2008).
31. Pernice, W. H. P., Li, M. & Tang, H. X. Optomechanical coupling in photonic crystal supported nanomechanical waveguides. *Opt. Express* **17,** 12424–12432 (2009).
32. Lin, Q., Rosenberg, J., Jiang, X., Vahala, K. J. & Painter, O. Mechanical oscillation and cooling actuated by the optical gradient force. *Phys. Rev. Lett.* **103,** 103601 (2009).
33. Eichenfield, M., Chan, J., Camacho, R. M., Vahala, K. J. & Painter, O. Optomechanical crystals. *Nature* **462,** 78–82 (2009).
34. Mahboob, I. & Yamaguchi, H. Parametrically pumped ultrahigh q electromechanical resonator. *Appl. Phys. Lett.* **92,** 253109 (2008).
35. Knobel, R. G. & Cleland, A. N. Nanometre-scale displacement sensing using a single electron transistor. *Nature* **424,** 291–293 (2003).
36. Thompson, J. D. *et al.* Strong dispersive coupling of a high-finesse cavity to a micromechanical membrane. *Nature* **452,** 72–75 (2008).

Acknowledgements

The financial support by the Deutsche Forschungsgemeinschaft via Project No. Ko 416/18, the German Excellence Initiative via the Nanosystems Initiative Munich (NIM) (which also contributed the title illustration) and LMUexcellent, the German-Israeli Foundation (G.I.F.), as well as the European Commission under the FET-Open project QNEMS (233992) is gratefully acknowledged. We would like to thank Florian Marquardt and Johannes Rieger for stimulating discussions.

Author contributions

All authors planned the experiment and discussed the data. The sample was fabricated by P.K., the measurement was carried out by P.K. and T.F. in a setup build by P.K., T.F. and S.M., who especially helped with the microwave measurements. T.F. and P.K. analysed the data, and T.F., J.P.K. and E.M.W. wrote the manuscript.

Additional information

Supplementary Information accompanies this paper at http://www.nature.com/naturecommunications

Competing financial interests: The authors declare no competing financial interests.

Reprints and permission information is available online at http://npg.nature.com/reprintsandpermissions/

How to cite this article: Faust, T. *et al.* Microwave cavity-enhanced transduction for plug and play nanomechanics at room temperature. *Nat. Commun.* 3:728 doi: 10.1038/ncomms1723 (2012).

3.1.1 Supplement

Published as Supplemental Material to *Nature Communications* **3**, 728 (2012), reference [Fau12a].

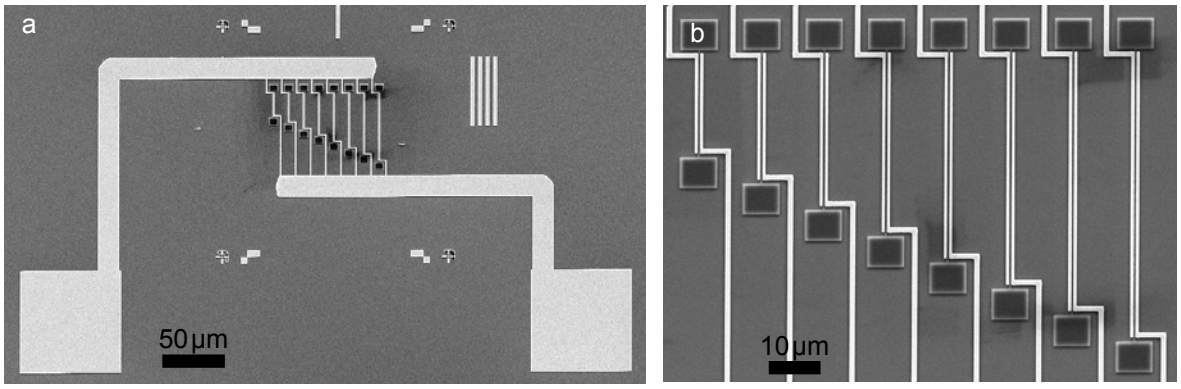

Supplementary Figure S1. **Mechanical resonator array:** A SEM micrograph of the entire mechanical resonator structure including the bond pads is shown in **a**. The central array of eight resonators with lengths ranging from 20 to 55 µm is shown in more detail in **b**.

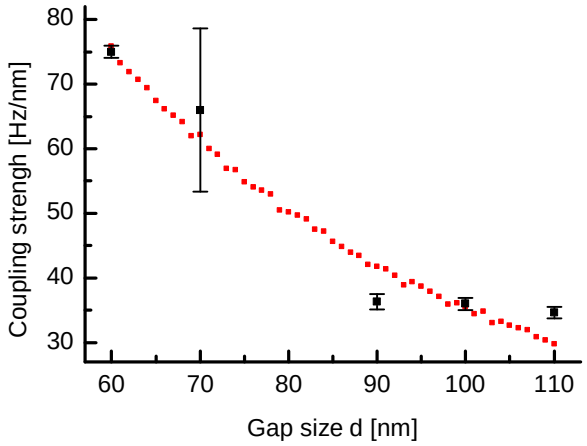

Supplementary Figure S2. **Coupling strength versus gap distance:** The black markers show the measured values of g for several different beams, including their error bars (confidence intervals of the fits). The large error at a gap size of 70 nm is caused by the low quality factor of this beam, presumably contaminated by etch residuals. The red dots are the capacitance gradients obtained from the simulation, multiplied by a scaling factor. There is a qualitative agreement between the simulation results and the measured data.

SUPPLEMENTARY METHODS

Displacement sensitivity

The displacement sensitivity is calibrated by calculating the amplitude distribution of the thermally induced Brownian motion of the beam [37]. The average kinetic energy of a harmonic oscillator in thermal equilibrium is

$$\langle E_{kin} \rangle = \frac{1}{2} k_B T = \frac{1}{4} m_{eff} \int_0^\infty A^2(f) f^2 df$$

where $A(f)$ designates the frequency-dependent displacement of the resonator, k_B is the Boltzmann constant, T the ambient temperature and

$$m_{eff} = \frac{m}{2} = \frac{\rho \cdot l \cdot w \cdot t}{2} = 1.9 \cdot 10^{-12}\,\mathrm{g}$$

the effective mass of a string with a sinusoidal oscillation profile, using the densitiy of silicon nitride $\rho = 2,600\,\mathrm{kg/m^3}$, the beam length $l = 55\,\mu\mathrm{m}$, width $w = 260\,\mathrm{nm}$ and thickness $t = 100\,\mathrm{nm}$. By assuming a Lorentzian distribution with the measured beam center frequency f_m and quality factor Q_m for $A(f)$, the amplitude of the spectral displacement distribution $A(f)$ can be calculated, yielding a peak value of $8\ \frac{\mathrm{pm}}{\sqrt{\mathrm{Hz}}}$.

By definition, the mechanical amplitude corresponding to a signal-to-noise ratio of unity defines the displacement sensitivity of the detection scheme. The peak amplitude of the fit in Fig. 2d of the main text is 276 nV, the noise level 98 nV, yielding a SNR of 1.8. We thus achieve a sensitivity of $\frac{8\ \frac{\mathrm{pm}}{\sqrt{\mathrm{Hz}}}}{1.8} = 4.4\ \frac{\mathrm{pm}}{\sqrt{\mathrm{Hz}}}$.

Theory of cavity-induced damping

A full quantum theory of cavity-assisted sideband cooling is given by Marquardt et al. [27]. In the following, his results are converted such that only experimentally accessible parameters enter, similar to the representation in the work of Teufel et al. [28]. The additional mechanical backaction damping exerted by the cavity is given as [27]

$$\Gamma = \frac{1}{\hbar^2} \left[S_{FF}(\omega_m) - S_{FF}(-\omega_m) \right] x_{ZPF}^2 \tag{S1}$$

with $\omega_m = 2\pi f_m$ and the zero point fluctuation $x_{ZPF} = \sqrt{\frac{\hbar}{2 m_{eff} \omega_m}}$. Furthermore, the radiation pressure power spectrum is

$$S_{FF}(\omega) = \hbar^2 A^2 \bar{n} \frac{\kappa}{(\omega + \Delta')^2 + (\kappa/2)^2} \tag{S2}$$

using the average number of cavity photons $\bar{n}$, the cavity damping $\kappa = \frac{2\pi f_c}{Q_c} = \frac{\omega_c}{Qc}$, the coupling constant $A = \frac{\partial \omega_c}{\partial z}$ and the angular frequency detuning $\Delta' = 2\pi(f_{\mu w} - f_c)$.

Equation S1 can then be expressed as

$$\Gamma = \frac{2\hbar A^2 \bar{n}}{m_{eff} \omega_m} \left[\frac{\kappa}{\kappa^2 + 4(\Delta' + \omega_m)^2} - \frac{\kappa}{\kappa^2 + 4(\Delta' - \omega_m)^2} \right]. \tag{S3}$$

The power lost in the cavity is $\kappa E_{\mathrm{stored}} = \kappa \bar{n} \hbar \omega_c$. In a steady state, this has to equal the power coupled into the cavity via the feed lines. Assuming that the cavity losses κ are only due to energy loss into the two symmetric feed lines (and thereby the coupling constant between one feed line and the cavity is $\kappa/2$), equation E47 in the supplement of Clerk et al. [29] gives the relation

$$P_{inc} = \hbar \omega_c \bar{n} \frac{\kappa}{2} \Rightarrow \bar{n} = \frac{2 P_{inc}}{\hbar \omega_c \kappa} \tag{S4}$$

for a two-sided cavity where the power is provided only via one of the two feed lines. Furthermore, this has to be

multiplied with the cavity resonance $\frac{\kappa^2}{\kappa^2+4\Delta'^2}$. Thus, the electromechanically induced damping can be written as

$$\Gamma(\Delta') = \frac{4P_{inc}A^2\kappa^2}{m_{eff}\omega_m\omega_c(\kappa^2+4\Delta'^2)}\left[\frac{1}{\kappa^2+4(\Delta'+\omega_m)^2} - \frac{1}{\kappa^2+4(\Delta'-\omega_m)^2}\right] \tag{S5}$$

or converted in frequency units

$$\Gamma(\Delta) = \frac{4P_{inc}g^2\kappa^2}{m_{eff}f_m f_c(\kappa^2+16\pi^2\Delta^2)}\left[\frac{1}{\kappa^2+16\pi^2(\Delta+f_m)^2} - \frac{1}{\kappa^2+16\pi^2(\Delta-f_m)^2}\right] \tag{S6}$$

using the normal frequency detuning $\Delta = f_{\mu w} - f_c$ and the coupling constant $g = \frac{\partial f_c}{\partial z}$. The angular frequency result of equation (S5) agrees with the formula used in [28] to within a factor of two. This is a consequence of the one-sided cavity and therefore a twice as effective input power coupling employed in the work of Teufel et al., leading to an additional factor two in the relation between input power and the number of cavity photons (S4 and [29]).

Using equation (S6), the effective quality factor Q of the mechanical mode depending on both the intrinsic damping $\gamma_m = \frac{2\pi f_m}{Q_m}$ and on the detuning Δ of the electrical cavity can be calculated:

$$Q(\Delta) = \frac{2\pi f_m}{\gamma_{total}} = \frac{2\pi f_m}{\gamma_m + \Gamma(\Delta)}. \tag{S7}$$

This formula was used to extract the coupling constant from the measured data sets of quality factors versus detuning and is shown as a black line in Fig. 3b of the main text. Note that the incident microwave power is the power in the feedline and not the generator output power, therefore $P_{inc} = 0.32 \cdot P_{\mu w}$, as 5 dB are lost in the cables and power splitter between the microwave source and the cavity.

Mass sensitivity

The mass sensitivity is estimated as follows: A small mass change δm of the effective mass m_{eff} of the resonator will lead to an eigenfrequency shift

$$\frac{\delta f}{f_m} = \frac{\delta m}{m_{eff}}.$$

We assume that a resonance frequency shift $\delta f = 2.5\,\mathrm{Hz}$ equaling half the self-oscillation linewidth can be resolved. The effective mass of an oscillating string with a sinusoidal mode profile is

$$m_{eff} = \frac{m}{2} = \frac{\rho \cdot l \cdot w \cdot t}{2} = 1.9 \cdot 10^{-12}\,\mathrm{g}$$

using the densitiy of silicon nitride $\rho = 2,600\,\mathrm{kg/m^3}$, the beam length $l = 55\,\mu\mathrm{m}$, width $w = 260\,\mathrm{nm}$ and thickness $t = 100\,\mathrm{nm}$. For a resonance frequency $f_m = 6.6\,\mathrm{MHz}$, the mass sensitivity thus is $\delta m = 7 \cdot 10^{-19}\,\mathrm{g}$ in the center of the beam. By monitoring several harmonics of the beam, it should also be possible to detect the position of the added mass [38].

SUPPLEMENTARY REFERENCES

[37] Hutter, J. L. & Bechhoefer, J. Calibration of atomic-force microscope tips. *Review of Scientific Instruments* **64**, 1868–1873 (1993).

[38] Dohn, S. & Svendsen, W. & Boisen, A. & Hansen, O. Mass and position determination of attached particles on cantilever based mass sensors. *Review of Scientific Instruments* **78**, 103303 (2007).

3.2 Frequency and Q-factor control of nanomechanical resonators

Published as *Applied Physics Letters* **101**, 103110 (2012), reference [Rie12].

Frequency and Q factor control of nanomechanical resonators

Johannes Rieger, Thomas Faust, Maximilian J. Seitner, Jörg P. Kotthaus, and Eva M. Weig[a)]
Center for NanoScience (CeNS) and Fakultät für Physik, Ludwig-Maximilians-Universität, Geschwister-Scholl-Platz 1, München 80539, Germany

(Received 12 July 2012; accepted 24 August 2012; published online 6 September 2012)

We present an integrated scheme for dielectric drive and read-out of high-Q nanomechanical resonators that enable tuning of both the resonance frequency and quality factor with an applied dc voltage. A simple model for altering these quantities is derived, incorporating the resonator's complex electric polarizability and position in an inhomogeneous electric field, which agrees very well with experimental findings and finite element simulations. Comparing two sample geometries demonstrates that careful electrode design determines the direction of frequency tuning of flexural modes of a string resonator. Furthermore, we show that the mechanical quality factor can be voltage reduced sixfold. © *2012 American Institute of Physics*.
[http://dx.doi.org/10.1063/1.4751351]

Control of small-scale mechanical systems is essential for their application. Resonant micro- and nanoelectromechanical systems (M/NEMS) have both proven themselves technologically viable (frequency filtering in cell phones,[1] gyroscopes,[2] atomic force microscope (AFM) cantilevers[3]) as well as shown great promise for next-generation sensor applications (mass sensors,[4–6] resonant bio sensors,[7] and ultra sensitive force sensors[8,9]). Three areas of development are central to realizing the potential of high performance resonant micro- and nanomechanics: advancement of high Q geometries and materials; improved readout schemes for mechanical motion, including compactness and integrability; and increased control of the resonant behavior of the mechanics. In the field of nanomechanics, the last years have seen the advent of high Q silicon nitride strings under high tensile stress.[10,11] Efficient integrated drive and read-out schemes have been developed to detect the sub-nanoscale motion of small-scale resonant mechanics.[12] Very good tunability of the resonance frequency can be achieved by capacitive coupling of the nanomechanical element to a side electrode.[13] However, the required metalization of the resonant structure reduces the room temperature quality factor significantly[14] via Ohmic losses. In our lab, an efficient, room-temperature microwave mixing scheme has been developed for readout[15] as well as a dielectric drive mechanism to actuate mechanics regardless of their material make-up,[16] importantly obviating the necessity to metallize otherwise low-loss dielectrics.

Here, we present a continuation of this development that enables tuning of both the frequency and quality factor of nanomechanical resonators in the context of this highly applicable and integrable scheme.[15] Using the combined dielectric actuation and microwave readout schemes, we theoretically develop the means to controllably raise and lower the resonant frequency of various flexural modes of our mechanics as well as to broaden the mechanical resonance linewidth. This represents a scheme for Q factor control,[17–19] a technique widely used in AFM measurements to increase scan speed by decreasing the mechanical response time.[20,21] The theoretical relationship between the design of the electrodes and the resulting control of a given mode is validated both by experiment and simulation.

Our system is depicted in Fig. 1. A nanomechanical silicon nitride string is situated between a pair of near-lying electrodes (Fig. 1(a)). They are used to dielectrically actuate the mechanical resonance[16] as well as to couple the mechanical resonator to an external microwave cavity. An equivalent circuit diagram is shown in Fig. 1(b). Deflection of the string translates into a change of the capacitance $C_m(t)$ between the two electrodes and thereby modulates the cavity

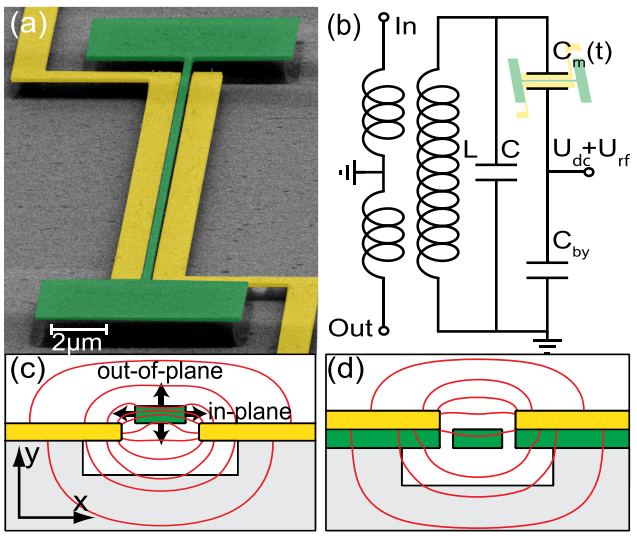

FIG. 1. (a) SEM micrograph of a 55 μm long silicon nitride resonator in the configuration depicted in (c). (b) Equivalent circuit diagram of the transduction scheme with an inductively coupled microwave cavity – represented by the capacitance C and inductance L – for dielectric readout. $C_m(t)$ is the capacitance of the gold electrodes which is modulated by resonator displacement. The microwave bypass capacitor C_{by} allows the additional application of a dc and rf voltage. (c) and (d) Schematic cross section with simulated field lines for the elevated and lowered geometry. The arrows in (c) describe the directions of the in-plane and out-of-plane oscillation.

[a)]Electronic mail: weig@lmu.de.

transmission signal. The mechanical oscillation can then be detected by demodulating this signal.[15] To enable direct actuation of the mechanical resonator, we introduce a microwave bypass between ground and one of the electrodes using the single layer capacitor (SLC)[22] C_{by}. Thus, a dc and rf voltage can be applied to this electrode, whereas the other electrode is grounded via the microstrip cavity (compare Fig. 1(b)).

For this study, two sample geometries for obtaining optimized gradient field coupling are fabricated from high-stress silicon nitride films deposited on fused silica. The geometries are schematically shown in Figs. 1(c) and 1(d). Referring to the string's position with respect to the electrodes, the two structures will from now on be referenced as "elevated" (Fig. 1(c)) and "lowered" (Fig. 1(d)). The centerpiece of each structure is the 55 μm long silicon nitride string resonator with a rectangular cross section of width 260 nm and height 100 nm. The freely suspended resonator is bordered by two vertically offset gold electrodes, one of which is connected to the microstrip cavity with a resonance frequency of 3.5 GHz and a quality factor of 70, while the other electrode leads to the SLC. The essential difference between the geometries is the vertical positioning of the string with respect to the gold electrodes. This affects the dielectric environment and thereby the electric field lines as depicted in Figs. 1(c) and 1(d). The simulated electric field lines for both geometries are obtained from finite element simulations using *COMSOL MULTIPHYSICS* and allow us to extract the electric field along the x- and y-direction. These inhomogeneous electric fields cause force gradients for the in- and out-of-plane modes of the resonator. They thus alter the restoring force of the respective mode and thereby its resonance frequency.[16] At the same time, the mechanical quality factor can be altered with the dc voltage, as the strong electric field and high field gradient lead to velocity-dependent dielectric losses in the string material. This frequency and linewidth tuning can be described by a simple model, which agrees very well with our experimental findings and finite element simulations. The resonance frequency can be tuned over 5% and the resonance linewidth can be increased by a factor of six for a dc voltage of 10 V.

We find the force gradient to be proportional to the square of the voltage and thus expect a quadratic dependence of the resonator resonance frequency on the applied dc voltage. This can be derived from the energy of the induced dipolar moment $\vec{p}$ of the dielectric resonator in an external electric field $\vec{E}$. Using a scalar, complex polarizability $\alpha = \alpha' + i\alpha''$ and introducing a dependence of the electric field on the variable coordinate ξ, the energy W reads

$$W = \vec{p} \cdot \vec{E} = pE = \alpha E^2 = (E(\xi))^2(\alpha' + i\alpha''). \quad (1)$$

Here ξ can be the x- or y-coordinate (compare Fig. 1(c)), so the following considerations apply to both the in- and out-of-plane mode. Assuming $E(\xi) = E_0 + E_1\xi$ for small displacements, the total energy can be separated into a real (stored) and an imaginary (dissipative) part

$$W_{\text{stored}} = \alpha'(E_0^2 + 2E_0E_1\xi + E_1^2\xi^2), \quad (2)$$

$$W_{\text{loss}} = \alpha''(E_0^2 + 2E_0E_1\xi + E_1^2\xi^2). \quad (3)$$

The second derivative of the stored energy provides an additional force gradient, i.e. an electrically induced spring constant k_e

$$k_e = -\frac{\partial F_e}{\partial \xi} = \frac{\partial^2 W_{\text{stored}}}{\partial \xi^2} = \alpha' E_1^2. \quad (4)$$

The shift in resonance frequency caused by k_e can be expressed as

$$f = \sqrt{\frac{k_0 + k_e}{m}} \approx f_0 + \frac{k_e}{2mf_0} = f_0 + \frac{\beta^2 U_{\text{dc}}^2 \alpha'}{2mf_0}, \quad (5)$$

with a geometry-dependent proportionality between applied voltage and field gradient $E_1 = \beta U_{\text{dc}}$. Moreover, as predicted by our finite-element simulations, the sign of the gradient depends on the chosen geometry such that the out-of-plane mode changes its tuning direction between the elevated and the lowered design, which does not occur for the in-plane mode.

The quadratic tuning behavior with dc voltage is found to agree very well with the experimental data, as displayed in Fig. 2. All measurements are conducted at room temperature and a pressure of 10^{-4} mbars. For each mode and geometry, the mechanical spectrum is taken for different dc

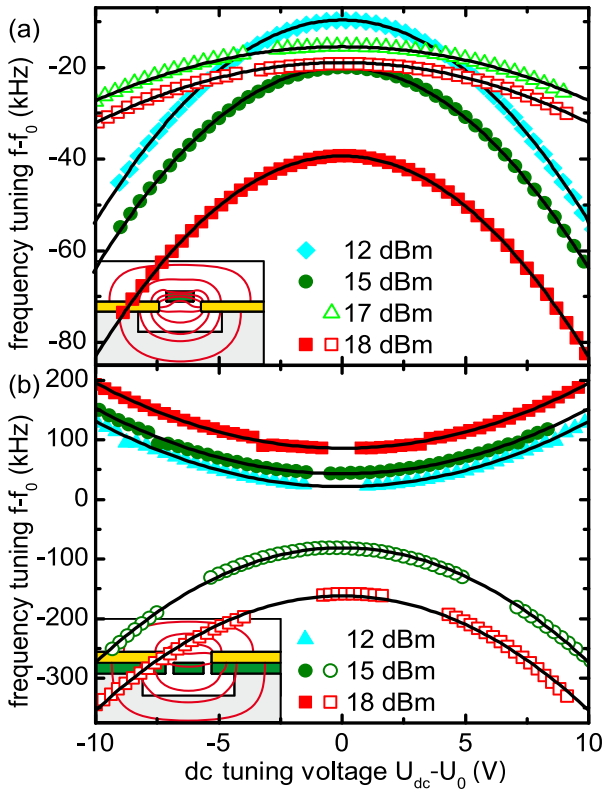

FIG. 2. Quadratic tuning of the mechanical resonance frequency with dc voltage U_{dc} for the two different geometries. The graphs show the deviation of the resonance frequency f from the natural resonance frequency f_0 of the resonator's respective mode (in- or out-of-plane, depicted as open and filled symbols) for different microwave cavity pump powers (in dBm). The solid lines are a fit of the model. (a) The force gradient has the same parity for the in-plane- as well as the out-of-plane mode. (b) With increasing $|U_{\text{dc}} - U_0|$, the out-of-plane mode tunes upwards and the in-plane-mode downwards in frequency.

voltages and microwave powers. The driving voltage U_{rf} is kept constant in every measurement. The values for U_{rf} lie within 80 μV and 1 mV depending on the particular mode and geometry.

A Lorentzian fit to each mechanical spectrum yields the resonance frequency and the quality factor for each parameter set. The resonance frequencies lie around 6.5 MHz and the highest quality factor is 340 000 for the out-of-plane mode in the elevated design. Note that the tuning with microwave power is a result of the effective microwave voltage[15] and so is analogous to the tuning with a dc voltage. Subsequently, we fit $f = f_0 + c_{dc}(U_{dc} - U_0)^2 + c_{mw}U_{mw}^2$ to the tuning curves shown in Fig. 2, using the natural resonance frequency f_0 and two tuning parameters for the dc voltage and the effective microwave voltage, as the dc and high frequency polarizability might differ. We also introduce the dc offset U_0 to account for a shift (typically less than 1 V) of the vertex of the tuning parabola, which is most likely caused by trapped charges in the dielectric resonator material. As the influence of the microwave field on static dipoles averages out, there is no such shift resulting from the microwave voltage U_{mw}. Consequently, we can extract the tuning parameters for each geometry and oscillation direction. With increasing voltage U_{dc} and for the elevated geometry depicted in Fig. 2(a), both the in- and out-of-plane mode tune to lower frequencies, whereas for the lowered design (Fig. 2(b)), the out-of-plane mode tunes to higher frequencies, as predicted by our simulations. The solid black lines in Fig. 2 show the fit of our model with a single set of parameters for each mode in excellent agreement with the data. In the case of opposite frequency tuning, the initial frequency difference of the in- and out-of-plane modes can be evened-out, which leads to an avoided crossing caused by a coupling between the modes.[23] As the data points in this coupling region deviate from normal tuning behavior, they have been omitted in Fig. 2(b).

Altering the dc or effective microwave voltage does not only shift the resonance frequency, but also influences the damping $\Gamma = 2\pi f/Q = 2\pi\Delta f$ of the mechanical resonance and thereby the measured linewidth Δf by adding a dielectric damping contribution Γ_e. The dielectrically induced damping Γ_e also varies quadratically with increasing voltage. This can be understood by analyzing the dissipated energy W_{loss} given by Eq. (3): A time average of this quantity over one period of mechanical vibration $\xi(t) = \xi_0\cos(\omega t)$ gives

$$\overline{W_{loss}} = \frac{1}{T}\int_0^T W_{loss}(\xi(t))dt = \frac{1}{2}\alpha'' E_1^2 \xi_o^2. \tag{6}$$

Here, we omit the E_0^2 term (as $\alpha''(\omega = 0) = 0$, otherwise static electric fields would lead to dissipation). As the mechanical stored energy $W_{mech} = \frac{1}{2}m\omega_0^2\xi_0^2$ is much larger than the electrical energy W_{stored}, one can approximate the additional electrical damping to be

$$\Gamma_e(U_{dc}) = \frac{\overline{W_{loss}}\omega_0}{2\pi W_{mech}} = \frac{\beta^2 U_{dc}^2 \alpha''}{2\pi m\omega_0}. \tag{7}$$

The measured damping versus dc voltage is shown in Fig. 3. It displays the quadratic behavior of the damping constant

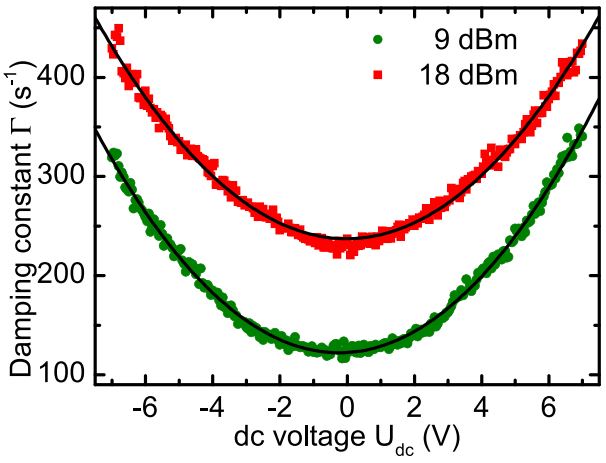

FIG. 3. Damping constant versus dc voltage for two different microwave powers, exhibiting a quadratic behavior. The solid lines are a fit of the model.

$\Gamma = \Gamma_0 + \Gamma_e(U_{dc}) = \Gamma_0 + c_\Gamma U_{dc}^2$ of the out-of-plane mode in the elevated design for two different microwave powers. Here, Γ_0 is the intrinsic damping of the resonator[11] and $\Gamma_e(U_{dc})$ is given by Eq. (7). Again, the vertical offset between the two curves is explained by the effective microwave voltage acting analogously to a dc voltage. The solid lines in Fig. 3 are a fit of the model to the data, from which the curvature c_Γ can be extracted.

Using this curvature and Eq. (7), the imaginary part of the polarizability can be expressed as $\alpha'' = 2\pi c_\Gamma m\omega_0/\beta^2$. Similarly, employing the curvature c_{dc} of the parabolic frequency shift and using Eq. (5), the real part α' reads $\alpha' = 2c_{dc}mf_0/\beta^2$. The ratio $\alpha''/\alpha' = \tan(\phi) = c_\Gamma/2c_{dc}$ is then independent of all resonator parameters and can be determined from the two curvatures. The measured values for damping and tuning curvatures are $c_\Gamma = 5.2\,\frac{1}{V^2 s}$ and $c_{dc} = 438\,\frac{Hz}{V^2}$, leading to $\tan(\phi) = 0.037$. By using the Clausius-Mossotti-Relation to first calculate the (lossless) α using $\epsilon = 7.5$, one can determine the dielectric loss tangent to be $\tan(\delta) = \epsilon''/\epsilon' = 0.016$, a value well within the range of loss tangents reported for silicon nitride thin films.[24] Note that the time-varying capacitance $C_m(t)$ induces a dissipative current in the electrodes, which also leads to a quadratically increasing damping.[13] However, using values obtained from FEM simulations for the electrode capacitance and its variation with string deflection,[16] we estimate that this damping is three orders of magnitude smaller than that caused by dielectric losses. The relevant effect for the additional damping with increasing dc voltage is thus the dissipative reorientation of the dipoles in the resonator caused by its motion in a static, inhomogeneous electric field described by Eq. (6).

The dc voltage dependence of the mechanical damping Γ was also measured at zero microwave power using an optical detection technique.[25] The resulting Γ_0 was within a few percent of the value extracted from the 9 dBm curve in Fig. 3, demonstrating that a measurement at low microwave powers induces only negligible additional damping to the mechanical resonator.

In conclusion, we show dielectric frequency tuning of over 5% of the natural resonance frequency for nanomechanical resonators in an all-integrated setup that requires no metallization of the resonant mechanical structure itself. This

scheme thus maintains an excellent quality factor of up to 340 000 at 6.5 MHz and 300 K. Furthermore, by careful design of the geometry, one can choose the tuning behavior of the out-of-plane mode to be either upward or downward in frequency and thus tune the two orthogonal resonator modes both in the same or in opposite directions. We demonstrate that dielectric losses become highly relevant when using nanoscale electrode geometries generating large field gradients providing high tunability. This allows to directly measure the ratio of the real and the imaginary part of the resonator's polarizability by monitoring the mechanical resonance. The resulting loss tangent agrees very well with material properties of silicon nitride. We demonstrate that the dielectric losses cause additional damping of the mechanical resonance, which increases quadratically with the applied dc bias. This could be used as a Q factor control[17,18,26] that does not require any active electronics such as a phase-locked loop but rather a single dc voltage. Such a Q factor control can be employed to increase the bandwidth of NEMS sensors significantly, leading to much more adaptable devices. Without the need for active electronics, this could prove to be very well suited for integrated designs. A full-fledged Q factor control however requires the possibility to also increase the quality factor. A possible realization – again without the need for external, active feedback – is the backaction caused by the read-out microwave cavity. This allows to reduce the mechanical resonance linewidth and even enter the regime of self-oscillation.[15] Backaction can also be used to broaden the linewidth, but we find the effect of dielectric losses to be more pronounced in our setup (a factor of six in linewidth broadening rather than a factor of two). Thus, together with microwave cavity backaction the mechanical resonance linewidth can be controlled from a few Hz up to more than 100 Hz, thereby tuning the mechanical bandwidth by about two orders of magnitude. Finally, we imagine that the scheme presented can also be employed to build self-sensing AFM cantilevers[27] with tunable bandwidth and resonance frequency that are not subject to the bandwidth limitations of the normally employed piezo drive and could thus be used in multifrequency force microscopy schemes.[28]

Financial support by the Deutsche Forschungsgemeinschaft via Project No. Ko 416/18, the German Excellence Initiative via the Nanosystems Initiative Munich (NIM) and LMUexcellent, as well as the European Commission under the FET-Open project QNEMS (233992) is gratefully acknowledged. We thank Darren R. Southworth for critically reading the manuscript.

[1]J. Bouchaud and H. Wicht, in *Society of Photo-Optical Instrumentation Engineers (SPIE) Conference Series*, edited by A. K. Henning (2005), Vol. 5717, pp. 50–54.
[2]R. Dean and A. Luque, IEEE Trans. Ind. Electron. **56**, 913 (2009).
[3]G. Binnig, C. F. Quate, and C. Gerber, Phys. Rev. Lett. **56**, 930 (1986).
[4]A. K. Naik, M. S. Hanay, W. K. Hiebert, X. L. Feng, and M. L. Roukes, Nat. Nanotechnol. **4**, 445 (2009).
[5]M. Li, E. B. Myers, H. X. Tang, S. J. Aldridge, H. C. McCaig, J. J. Whiting, R. J. Simonson, N. S. Lewis, and M. L. Roukes, Nano Lett. **10**, 3899 (2010).
[6]J. Chaste, A. Eichler, J. Moser, G. Ceballos, R. Rurali, and A. Bachtold, Nat. Nanotechnol. **7**, 301 (2012).
[7]T. P. Burg, M. Godin, S. M. Knudsen, W. Shen, G. Carlson, J. S. Foster, K. Babcock, and S. R. Manalis, Nature **446**, 1066 (2007).
[8]H. J. Mamin and D. Rugar, Appl. Phys. Lett. **79**, 3358 (2001).
[9]C. A. Regal, J. D. Teufel, and K. W. Lehnert, Nat. Phys. **4**, 555 (2008).
[10]S. S. Verbridge, J. M. Parpia, R. B. Reichenbach, L. M. Bellan, and H. G. Craighead, J. Appl. Phys. **99**, 124304 (2006).
[11]Q. P. Unterreithmeier, T. Faust, and J. P. Kotthaus, Phys. Rev. Lett. **105**, 027205 (2010).
[12]K. Ekinci, Small **1**, 786 (2005).
[13]I. Kozinsky, H. W. C. Postma, I. Bargatin, and M. L. Roukes, Appl. Phys. Lett. **88**, 253101 (2006).
[14]P.-L. Yu, T. P. Purdy, and C. A. Regal, Phys. Rev. Lett. **108**, 083603 (2012).
[15]T. Faust, P. Krenn, S. Manus, J. P. Kotthaus, and E. M. Weig, Nat. Commun. **3**, 728 (2012).
[16]Q. P. Unterreithmeier, E. M. Weig, and J. P. Kotthaus, Nature **458**, 1001 (2009).
[17]T. Sulchek, R. Hsieh, J. D. Adams, G. G. Yaralioglu, S. C. Minne, C. F. Quate, J. P. Cleveland, A. Atalar, and D. M. Adderton, Appl. Phys. Lett. **76**, 1473 (2000).
[18]T. R. Rodriguez and R. Garcia, Appl. Phys. Lett. **82**, 4821 (2003).
[19]*Springer Handbook of Nanotechnology*, edited by B. Bhushan (Springer, 2010), p. 754 ff.
[20]J. Mertz, O. Marti, and J. Mlynek, Appl. Phys. Lett. **62**, 2344 (1993).
[21]T. Sulchek, G. G. Yaralioglu, C. F. Quate, and S. C. Minne, Rev. Sci. Instrum. **73**, 2928 (2002).
[22]Single layer capacitor, part number 500U04A182KT4S from Johanson Technology.
[23]T. Faust, J. Rieger, M. J. Seitner, P. Krenn, J. P. Kotthaus, and E. M. Weig, Phys. Rev. Lett. **109**, 037205 (2012).
[24]R. Gould, Thin Solid Films **433**, 309 (2003).
[25]T. Kouh, D. Karabacak, D. H. Kim, and K. L. Ekinci, Appl. Phys. Lett. **86**, 013106 (2005).
[26]W. J. Venstra, H. J. R. Westra, and H. S. J. van der Zant, Appl. Phys. Lett. **99**, 151904 (2011).
[27]M. Li, H. X. Tang, and M. L. Roukes, Nat. Nanotechnol. **2**, 114 (2007).
[28]R. Garcia and E. T. Herruzo, Nat. Nanotechnol. **7**, 217 (2012).

Chapter 4

Coupled mechanical resonators

The two fundamental flexural modes of the nanomechanical resonators used throughout this work are the out-of-plane mode, oscillating perpendicular to the surface of the chip, and the in-plane mode, with an oscillation direction parallel to the chip. Chapter 3.2 already discussed the different behaviour of these two modes when a dc voltage is applied to the electrodes alongside the beam: If the arrangement of the electrodes is chosen just right, the in-plane mode will decrease its frequency with increasing voltage, while the out-of-plane mode increases in frequency. As the width of the beam exceeds its thickness, the in-plane mode is stiffer and thus has a higher resonance frequency at zero bias voltage.

At a certain voltage, the resonance frequencies of the two modes should be identical. Instead of a crossing, we observe a pronounced avoided crossing, indicating a strong coupling between these two modes. Similar behaviour could be observed before in other nanomechanical systems [Koz06, Oka09, Per11, Kar11], but these schemes suffered from insensitive detection, slow tuning speeds or weak coupling.

In the following chapter, this system of two coupled mechanical resonances is used to present the first nanomechanical Landau-Zener transition [Lan32, Zen32, Stu32, Maj32]. After characterizing the avoided crossing and the underlying coupling strength, one mode is first initialized far away from the avoided crossing by an ac drive signal and then the tuning voltage is ramped up to let the system cross through the coupling region. The resulting behaviour depends on the tuning speed used in the experiment: At very low speeds, the system is always in its adiabatic energy eigenstate and thus stays on the branch it was initialized in, thereby transforming an in-plane motion to an out-of-plane motion and vice-versa. In contrast to that, very high speeds lead to a diabatic crossing of the coupling region, where no energy is exchanged between the two different oscillation directions. By measuring the energy in the two modes after the passage through the avoided crossing, this can be verified and a very good agreement with a classical Landau-Zener theory [Nov10] is established.

Besides more details of the data analysis and a theoretical treatment of the mode frequencies and quality factors in the vicinity of the avoided crossing (created by J. Rieger), chapter 4.1.1 presents a calculation of the oscillation directions of the coupled modes and

an explanation of the coupling mechanism. It can be shown that the two coupled modes exhibit a diagonal oscillation at the point of minimal frequency separation between the modes, thus the adiabatic passage through the coupling region corresponds to a slow tilting of the real-space oscillation direction by $90°$. Furthermore, the inhomogeneous electric field generated by the side electrodes not only leads to the frequency and quality factor tuning described in chapter 3.2, but it is also responsible for the observed coupling: If the mixed partial derivatives of the field in both oscillation directions are non-zero, they lead to a cross-coupling between the modes which exerts a force gradient on one mode depending on the beam displacement in the direction of the other mode.

The Landau-Zener experiment in chapter 4.1 demonstrates that the voltage pulses applied to the system can be much shorter than the energy relaxation time of the mechanical oscillation. This already indicates that it might be possible to perform coherent experiments with such a nanoelectromechanical system (a different realization of a coherent micromechanical system was created simultaneously at NTT in Japan [Oka12]). To test this, a new, clean sample with a higher quality factor connected to an improved microstrip resonator [Kra12] are placed inside the cryostat described in chapter 2.2. As the measurement is performed using the heterodyne microwave setup presented in chapter 3, no more positioning problems arise. But there are several benefits from the low temperatures: The quality factor of the microwave cavity is increased, as the conductivitiy of the copper strips is rising. Furthermore, the fluctuations of the mechanical resonance frequency are now very small. Such effects, mostly caused by temperature variations, which change the prestress of the SiN layer, and charge fluctuations in the beam, altering the magnitude of the dielectric forces, were a rather large problem for the room temperature measurement of the Landau-Zener transitions and sometimes caused the frequency tracking algorithm to loose the resonance. To further improve the stability of the experiment, a lower microwave power of 15 dBm (instead of the usual 18 dBm as in the previous chapters) is applied. This lowers the amplitude of the microwave power fluctuations and thus their impact on the effective electric field (which influences the mechanical frequency and coupling strength). Although the lower power also leads to a lower detection sensitivity, the reduced drift is more important for measurements possibly spanning multiple days.

The chip design is slightly different from the one used in the Landau-Zener experiment of chapter 4.1. The two electrodes are intentionally fabricated with a 20 nm asymmetry in the gap sizes d (see Fig. 1b of chapter 3.1) to increase the in-plane gradient of the electric field, which leads to an increase in coupling strength Ω (denoted as $\Gamma/2\pi$ throughout chapter 4.1) from 8 to 24 kHz.

Usually, coherent experiments are performed using two discrete energy levels of a system [Van05]. With suitable pulses, any superposition state between the two levels can be obtained, and the readout is performed by measuring the population of one level after the pulse sequence. A common example is the spin of a nucleus or electron in an external magnetic field [Pet05, Han07, Rei08, Blu11]. The Zeeman energy leads to the formation of two discrete energy levels, while radio frequency pulses can be used to manipulate the spin orientation. The two states used in the mechanical two-level system

presented here are the two hybrid oscillation modes created at the avoided crossing. In contrast to e. g. a spin system, none of the states is occupied at the beginning of the experiment (if the very small Brownian motion of both modes is neglected). Thus, the first step is always to actuate the lower-frequency mechanical mode (corresponding to the ground state) and then adiabatically tune the system to the point of maximal coupling. Furthermore, coherent experiments are usually performed on quantum systems where only one single particle or excitation is present at any given time, whose state is destroyed during a measurement. To obtain information about the time-evolution in such a system, the identical experiment has to be repeated multiple times, while the measurement is conducted at different points in time. The mechanical resonator used here is excited to a classical state containing billions of phonons (analogous to a system of many spins at elevated temperature), which enables a continous measurement of its time evolution.

Other than that, the behaviour of the mechanical system is very similar to most other coherent systems and the same pulsed experiments can be performed. In chapter 4.2, the measurement of Rabi oscillations [Rab37], the energy relaxation rate, Ramsey fringes [Ram50] and Hahn echo [Hah50] signals is demonstrated. The energy relaxation time T_1 and the two phase relaxation times T_2 and T_2^* (where $T_2^* \leq T_2$ includes reversible phase diffusion processes) can be extracted from these measurements. The results clearly show that there are no temporal or spatial fluctuations of the coupling strength or spatial inhomogeneities in the system, as $T_2^* = T_2$. Furthermore, the average energy relaxation time is identical to the phase relaxation time, revealing that decoherence is solely induced by energy decay [Dra06]. Chapter 4.2.1 provides additional details about the definition of the relaxation times in the decaying system presented here, shows the exact pulse calibration schemes used in the experiments and presents a comparison of the phase relaxation processes in different coherent nanoscale systems.

Using the cavity backaction effects described in chapter 3.1, the energy decay rate of the system can be controlled. By detuning the microwave pump frequency with respect to the microstrip cavity resonance, the "opto"mechanical effects lead to the creation or anihilation of phonons. As demonstrated in chapter 4.3, the phase coherence time can not only be reduced but also increased by this pumping scheme, indicating that the backaction phonon generation is a coherent process similar to the stimulated emission in a laser.

Another experiment showing the coherent behaviour of the nanoelectromechanical system is presented in chapter 4.4. The so-called Stückelberg oscillations [Stu32, She10] arise if the system is tuned through the avoided crossing multiple times, and not only once as in the Landau-Zener experiment. After the first passage through the coupling region, the energy which was initially only in one mode is distributed between both modes, while the exact ratio depends on the tuning speed. Both modes pick up a different phase during this time, which can be visualized by reversing the tuning direction and thus bringing the system back to the coupling region. There, both modes once more interact with each other, thus visualizing the phase difference. If the energy in one mode after this double passage is monitored, an oscillation depending on the tuning speed or tuning amplitude can be observed.

4.1 Nonadiabatic Dynamics of Two Strongly Coupled Nanomechanical Resonator Modes

Published as *Physical Review Letters* **109**, 037205 (2012), reference [Fau12c].

Nonadiabatic Dynamics of Two Strongly Coupled Nanomechanical Resonator Modes

Thomas Faust, Johannes Rieger, Maximilian J. Seitner, Peter Krenn, Jörg P. Kotthaus,* and Eva M. Weig†

Center for NanoScience (CeNS) and Fakultät für Physik, Ludwig-Maximilians-Universität, Geschwister-Scholl-Platz 1, München 80539, Germany

(Received 19 January 2012; published 17 July 2012)

The Landau-Zener transition is a fundamental concept for dynamical quantum systems and has been studied in numerous fields of physics. Here, we present a classical mechanical model system exhibiting analogous behavior using two inversely tunable, strongly coupled modes of the same nanomechanical beam resonator. In the adiabatic limit, the anticrossing between the two modes is observed and the coupling strength extracted. Sweeping an initialized mode across the coupling region allows mapping of the progression from diabatic to adiabatic transitions as a function of the sweep rate.

DOI: 10.1103/PhysRevLett.109.037205 PACS numbers: 85.85.+j, 05.45.Xt, 62.25.Fg

The time dynamics of two strongly coupled harmonic oscillators follows the Landau-Zener model [1–4], which is used to describe the quantum mechanical mode tunneling in a nonadiabatic transition. This phenomenon is observed and utilized in many areas of physics, e.g., atomic resonances [5], quantum dots [6], superconducting qubits [7], and nitrogen-vacancy centers in diamond [8]. It is also possible to create classical model systems exhibiting the same time evolution, which until now have been restricted to optical configurations [9,10]. Such systems are well suited for the study of diabatic behavior over a wide parameter space; for example, nonlinearities could be readily introduced, potentially leading to chaotic behavior [9,11].

Nanomechanical resonators with frequencies in the MHz range can be realized with high mechanical quality factors [12,13] and easily tuned [14] in frequency. This makes them particularly well suited for exploration of their coupling to other mechanical, optical, or electrical microwave resonators. Strong cavity coupling in the optical or microwave regime has been widely studied as it enables both cooling and self-oscillation of the mechanical modes [15–18]. In addition, the time-resolved Rabi oscillations between a strongly coupled two-level system and a micromechanical resonator have been observed [19].

Purely mechanical, static coupling between different resonators [20–23] and between different harmonic modes of the same resonator [24] has also been demonstrated. Here, we explore the coupling between the two fundamental flexural modes [25] of a single nanomechanical beam vibrating in plane and out of plane, respectively. We study the adiabatic to nonadiabatic transitions between the two strongly coupled classical mechanical modes in time-dependent experiments, in correspondence to the Landau-Zener transition.

The nanomechanical high-stress silicon nitride string used in this work is shown in Fig. 1. Two parallel gold electrodes vertically offset to the beam are used to dielectrically couple the beam oscillation to an external microwave cavity with a quality factor of ≈ 70 at a resonance frequency of 3.44 GHz [26]. Displacement of the resonator leads to a change in capacitance between the two electrodes, thereby detuning the resonance frequency of the microwave circuit and creating sidebands with a frequency offset equal to the mechanical eigenfrequency. The inductively coupled microwave cavity is driven by a signal generator; the transmission signal is demodulated and fed to a spectrum analyzer as depicted in Fig. 1 and described in more detail in [26]. In addition, a microwave bypass capacitor is used in the ground connection of one electrode which allows application of additional dc bias and rf voltages to the electrodes. This is used to actuate the mechanical resonator via the dielectric driving mechanism [14,27]. At the same time, the dielectric coupling

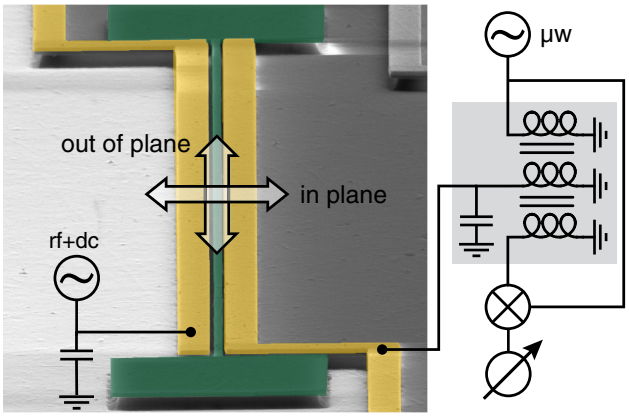

FIG. 1 (color online). The SEM micrograph of the 55 μm long and 260-nm wide silicon nitride string resonator [green (dark gray)] taken at an angle of 85° also depicts the two adjacent gold electrodes [yellow (light gray)] used to dielectrically drive, tune, and read out the resonator motion. The arrows denote the two mechanical modes, one oscillating parallel and the other perpendicular to the plane of the chip. The simplified measurement scheme [26] shows the connection of the electrodes to the readout cavity (gray box) and the microwave bypass capacitor in the bottom left.

provides a way to tune the resonance frequency of the two mechanical modes: The static electric field between the electrodes polarizes the dielectric resonator material which is then attracted to high electric fields, thereby changing the spring constant of the modes via the resulting force gradient [14]. In the chosen geometry, where the bottom of the electrodes is flushed with the top of the beam [26], a rising dc bias voltage causes the frequency of the in-plane mode to decrease and the out-of-plane frequency to increase [28]. All experiments are performed at room temperature at pressures below 5×10^{-4} mbar.

At low dc bias voltages, the in-plane mode of the 55 μm long beam has a higher resonance frequency than the out-of-plane mode. This is a result of the 260 nm beam width exceeding the beam's thickness of 100 nm, which leads to a higher rigidity for the in-plane mode [13]. Thus, by increasing the dc bias voltage, we are able to tune the two modes into resonance at a common frequency of approximately 6.63 MHz. The coupling between the modes has been observed for several resonators on various chips and is at least partially caused by the spatially inhomogeneous electric field [29]. There might also be an additional, purely mechanical coupling mediated by the prestress in the beam. The characteristic avoided crossing diagram of two coupled oscillators can be obtained by measuring the driven response of the two modes at different dc bias voltages, as shown in Fig. 2.

Splitting this diagram into an upper and lower branch and fitting each data set with a Lorentzian allows the extraction of the resonance frequencies and quality factors for each dc bias voltage applied to the electrodes. Both modes exhibit a quality factor of approximately 80 000, somewhat lower than in previous measurements [26], presumably caused by fabrication imperfections. The eigenfrequencies extracted from the anticrossing diagram are depicted in Fig. 3. A few data points around 6.5 and 7.4 V in the upper branch were omitted because of an insufficient signal to noise ratio.

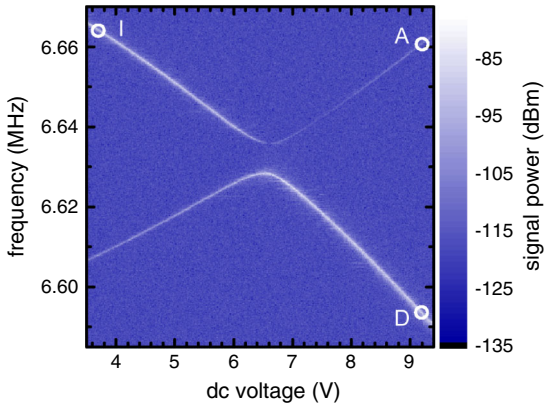

FIG. 2 (color online). Both mechanical modes can be tuned in opposite direction by increasing the dc bias voltage applied to the electrodes. The signal power of the driven resonances is shown color-coded versus dc voltage and drive frequency. Note the clear avoided crossing between the two modes. The three circles denote the initial state (I) and two possible final states after an adiabatic (A) or diabatic (D) transition through the coupling region, as described in the text.

For our system, the standard model of two coupled harmonic oscillators [30] needs to be expanded, as both oscillators react differently to the tuning parameter (the dc bias voltage). We use the generalized differential equation for the displacement u_n of each mode n ($n = 1, 2$)

$$m_{\mathrm{eff}} u_n'' + m_{\mathrm{eff}} \gamma u_n' + k_{nm} u_n = 0 \tag{1}$$

with

$$k_{nm} = \begin{pmatrix} k_1 + k_c & -k_c \\ -k_c & k_2 + k_c \end{pmatrix}, \tag{2}$$

where m_{eff} denotes the effective mass and $\gamma = \omega/Q$ the damping constant of the resonator (identical for both modes), k_c the coupling between the two modes, and k_n the spring constant of the respective mode. As the dc bias voltage polarizes the resonator material and creates an electric field gradient, the additional force gradient seen by the beam depends on the square of the voltage. We use a second-order series expansion around U_0 to describe the tuning behavior: $k_n = k_0 + \kappa_n(U - U_0) + \lambda_n(U - U_0)^2$ with κ_n and λ_n as linear and quadratic tuning constants, assuming that both modes have the same spring constant k_0 at the voltage U_0 corresponding to zero detuning. Note that the influence of the quadratic term is less than 15% in the whole voltage range [29]. The two solutions of the differential equation (1) describe the two branches, and their fit to the experimental data is shown as solid lines in Fig. 3. The extracted frequency splitting

$$\frac{\Gamma}{2\pi} = \frac{1}{2\pi}\left(\sqrt{\frac{k_0 + 2k_c}{m_{\mathrm{eff}}}} - \sqrt{\frac{k_0}{m_{\mathrm{eff}}}}\right) = 7.77\ \mathrm{kHz} \tag{3}$$

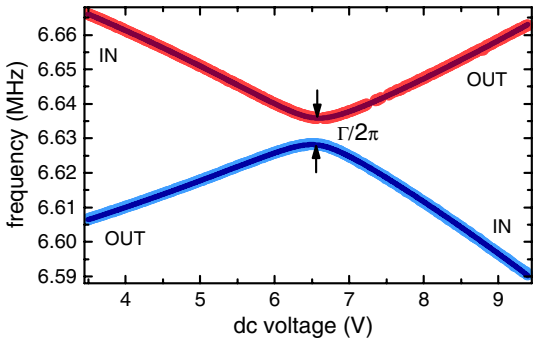

FIG. 3 (color online). Frequency of the upper (red) and lower (blue) branch versus dc bias voltage. Each dot represents a value extracted from a Lorentzian fit of the data shown in Fig. 2, and the solid lines are a fit of the theoretical model described in the text. IN and OUT denote the in- and out-of-plane mode of the beam.

at $U_0 = 6.547$ V is much larger than the linewidth of $\gamma/2\pi = 82$ Hz; thus, the system is clearly in the strong-coupling regime.

When slowly (adiabatically) tuning the system through the coupling region, the system energy will remain in the branch in which it was initialized, thereby transforming an out-of-plane oscillation to an in-plane motion (and vice-versa for the other mode). At high tuning speeds, the diabatic behavior dominates and there is no mixing between the modes. This classical behavior [30] is analogous to the well-known quantum mechanical Landau-Zener transition. The transition probabilities are identical in the quantum and classical case:

$$P_{\mathrm{dia}} = \exp\left(-\frac{\pi\Gamma^2}{2\alpha}\right), \qquad P_{\mathrm{adia}} = 1 - P_{\mathrm{dia}}, \tag{4}$$

where the change of the frequency difference between the two modes in time

$$\alpha = \frac{\partial(\omega_1 - \omega_2)}{\partial t} \quad \text{using } \omega_n = \sqrt{\frac{k_n}{m_{\mathrm{eff}}}} \tag{5}$$

denotes the tuning speed [29].

The measurement sequence is depicted in Fig. 4(a): the system is initialized at point I (see Fig. 2) by applying a 6.6647 MHz tone and a dc bias voltage of 3.6 V to the electrodes. At $t = 0$, the voltage (blue line) is now ramped up to 9.1 V within time τ. As the start and stop frequencies are kept constant throughout the experiment, changing τ changes the tuning speed α and, therefore, the transition probability. Thus, the system's energy is distributed between point A or D (see Fig. 2), depending on the ramp time τ. At $t = 0$, the mechanical resonator gets detuned from the constant drive frequency. Therefore, its energy starts to decay as reflected by the decreasing signal power [green dashed line in Fig. 4(a)]. After a short additional delay of δ (to avoid transient artifacts in the measurement), the decay of the mechanical oscillation is recorded with the spectrum analyzer. An exponential fit to the signal power, symbolized by the dotted black line in Fig. 4(a) allows the extraction of the oscillation magnitude at $t = \tau$, which is normalized to the magnitude measured before the transition at point I to account for slight variations in the initialization. This experiment is repeated with many different ramp times τ and with the detection frequency of the spectrum analyzer set to monitor either point A or D. The results of these measurements are shown in Fig. 4(b). The data clearly show the expected behavior: For short ramp times below 0.2 ms, the diabatic behavior dominates. For long ramp times, the adiabatic transition prevails, even though mechanical damping decreases the signal for large τ.

As can be seen in the inset of Fig. 4(b), the sum of the two curves perfectly follows the exponential decay of the mechanical energy (solid line). This decay in amplitude between $t = 0$ and $t = \tau$ has to be accounted for in the theoretical model and, therefore, an additional decay term $e^{-\gamma t}$ is introduced to Eqs. (4). The solid lines in Fig. 4(b) show the resulting transition probabilities to point A and D and are calculated by using the α and Γ obtained from the data in Fig. 3. The measured data was rescaled by a constant factor with no free parameters to represent the probability distribution of the resonator's energy after a transition [29]. A third state, representing the probability that the mechanical energy decays, is required to keep the sum of the probabilities at one. It is determined from the inset and shown as a green dashed line in Fig. 4(b). The corresponding decay constant $1/\gamma = 1.92$ ms is identical to the one extracted from the spectrally measured quality factor. Note that dynamics with a time constant much smaller than $1/\gamma$ are observed, demonstrating coherent control of the system.

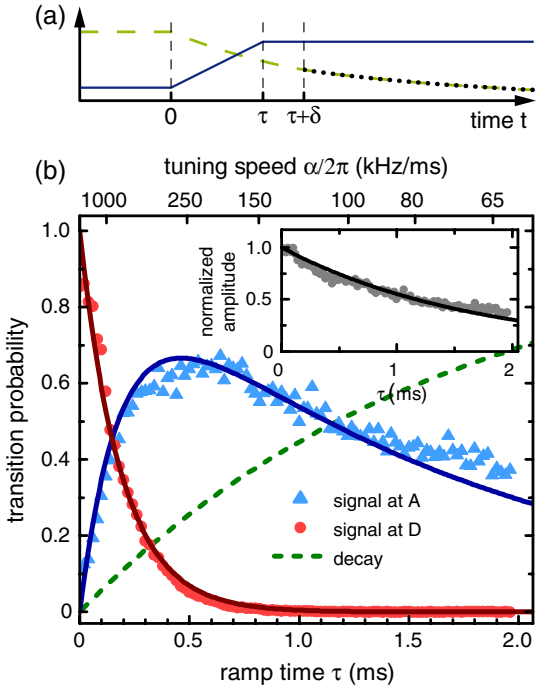

FIG. 4 (color online). The measurement sequence of the time-resolved experiment is shown in (a). At $t = 0$, the dc bias voltage (blue line) is ramped up in the timespan τ, after the delay δ the measurement of the mechanical signal power (green dashed line) starts at point A or D in Fig. 2 and a fit (black dotted line) is used to extract the magnitude of the beam oscillation at $t = \tau$. The normalized signal power at $t = \tau$ and, thus, the transition probability obtained for different ramp times τ measured at point A in Fig. 2 (blue triangles) or point D (red dots) is plotted in (b) together with the theoretical model described in the text (solid lines). The inset shows the sum of both measurements and displays a clear exponential decay. The corresponding decay probability is represented by a green dashed line in the main plot.

In conclusion, we utilize the strong coupling between two orthogonal modes of the same nanomechanical resonator by tuning these two modes into resonance to analyze their time-dependent dynamics. After characterizing the coupling, we are able to model the time-resolved transition

behavior between the two modes. The entire dynamic range between fast and coherent diabatic and slow adiabatic passages is accessible in the experiment, and a good agreement between theory and experiment is observed.

The experiment is conducted with approximately 10^9 phonons in the vibrational mode of the resonator; thus, not the single-particle probability function but the energy distribution of the ensemble is measured in the classical limit. Since the (strongly) nonlinear regime of the utilized nanomechanical resonator can be easily accessed, the presented system could also be used to study the coupling and the time-dependent transitions of two nonlinear oscillators [31,32] and the development of chaotic behavior [11,32] in the classical regime. Combining cavity-pumped self-oscillation [16] with the coupled resonator modes presented here allows the study of synchronization and collective dynamics in nanomechanical systems, as theoretically predicted [33,34]. Furthermore, after the recent breakthrough in the ground state cooling of mechanical resonators [17–19], the coupling between two quantum mechanical elements becomes accessible.

Financial support by the Deutsche Forschungsgemeinschaft via Project No. Ko 416/18, the German Excellence Initiative via the Nanosystems Initiative Munich (NIM) and LMUexcellent, as well as the European Commission under the FET-Open project QNEMS (233992) is gratefully acknowledged. We thank Andreas Isacsson for stimulating discussions and Darren R. Southworth for critically reading the manuscript.

*kotthaus@lmu.de
†weig@lmu.de

[1] L. D. Landau, Phys. Z. Sowjetunion **2**, 46 (1932).
[2] C. Zener, Proc. R. Soc. A **137**, 696 (1932).
[3] E. C. G. Stueckelberg, Helv. Phys. Acta **5**, 369 (1932).
[4] E. Majorana, Nuovo Cimento **9**, 43 (1932).
[5] J. R. Rubbmark, M. M. Kash, M. G. Littman, and D. Kleppner, Phys. Rev. A **23**, 3107 (1981).
[6] J. R. Petta, H. Lu, and A. C. Gossard, Science **327**, 669 (2010).
[7] M. Sillanpää, T. Lehtinen, A. Paila, Y. Makhlin, and P. Hakonen, Phys. Rev. Lett. **96**, 187002 (2006).
[8] G. D. Fuchs, G. Burkard, P. V. Klimov, and D. D. Awschalom, Nature Phys. **7**, 789 (2011).
[9] R. J. C. Spreeuw, N. J. van Druten, M. W. Beijersbergen, E. R. Eliel, and J. P. Woerdman, Phys. Rev. Lett. **65**, 2642 (1990).
[10] D. Bouwmeester, N. H. Dekker, F. E. V. Dorsselaer, C. A. Schrama, P. M. Visser, and J. P. Woerdman, Phys. Rev. A **51**, 646 (1995).
[11] J. Kozłowski, U. Parlitz, and W. Lauterborn, Phys. Rev. E **51**, 1861 (1995).
[12] S. S. Verbridge, J. M. Parpia, R. B. Reichenbach, L. M. Bellan, and H. G. Craighead, J. Appl. Phys. **99**, 124304 (2006).
[13] Q. P. Unterreithmeier, T. Faust, and J. P. Kotthaus, Phys. Rev. Lett. **105**, 027205 (2010).
[14] Q. P. Unterreithmeier, E. M. Weig, and J. P. Kotthaus, Nature (London) **458**, 1001 (2009).
[15] S. Gröblacher, K. Hammerer, M. R. Vanner, and M. Aspelmeyer, Nature (London) **460**, 724 (2009).
[16] E. Verhagen, S. Deléglise, S. Weis, A. Schliesser, and T. J. Kippenberg, Nature (London) **482**, 63 (2012).
[17] J. D. Teufel, T. Donner, D. Li, J. W. Harlow, M. S. Allman, K. Cicak, A. J. Sirois, J. D. Whittaker, K. W. Lehnert, and R. W. Simmonds, Nature (London) **475**, 359 (2011).
[18] J. Chan, T. P. Mayer Alegre, A. H. Safavi-Naeini, J. T. Hill, A. Krause, S. Gröblacher, M. Aspelmeyer, and O. Painter, Nature (London) **478**, 89 (2011).
[19] A. D. O'Connell, M. Hofheinz, M. Ansmann, R. C. Bialczak, M. Lenander, E. Lucero, M. Neeley, D. Sank, H. Wang, M. Weides, J. Wenner, J. M. Martinis, and A. N. Cleland, Nature (London) **464**, 697 (2010).
[20] H. Okamoto, T. Kamada, K. Onomitsu, I. Mahboob, and H. Yamaguchi, Appl. Phys. Express **2**, 062202 (2009).
[21] R. B. Karabalin, M. C. Cross, and M. L. Roukes, Phys. Rev. B **79**, 165309 (2009).
[22] R. B. Karabalin, R. Lifshitz, M. C. Cross, M. H. Matheny, S. C. Masmanidis, and M. L. Roukes, Phys. Rev. Lett. **106**, 094102 (2011).
[23] S. Perisanu, T. Barois, P. Poncharal, T. Gaillard, A. Ayari, S. T. Purcell, and P. Vincent, Appl. Phys. Lett. **98**, 063110 (2011).
[24] H. J. R. Westra, M. Poot, H. S. J. van der Zant, and W. J. Venstra, Phys. Rev. Lett. **105**, 117205 (2010).
[25] I. Kozinsky, H. W. Ch. Postma, I. Bargatin, and M. L. Roukes, Appl. Phys. Lett. **88**, 253101 (2006).
[26] T. Faust, P. Krenn, S. Manus, J. P. Kotthaus, and E. M. Weig, Nature Commun. **3**, 728 (2012).
[27] S. Schmid, M. Wendlandt, D. Junker, and C. Hierold, Appl. Phys. Lett. **89**, 163506 (2006).
[28] J. Rieger, T. Faust, M. J. Seitner, J. P. Kotthaus, and E. M. Weig, arXiv:1207.2403.
[29] See Supplemental Material at http://link.aps.org/supplemental/10.1103/PhysRevLett.109.037205 for the solution of the coupled differential equations, details of the tuning behavior, the data analysis, and the coupling mechanism.
[30] L. Novotny, Am. J. Phys. **78**, 1199 (2010).
[31] J. Liu, L. Fu, B.-Y. Ou, S.-G. Chen, D.-I. Choi, B. Wu, and Q. Niu, Phys. Rev. A **66**, 023404 (2002).
[32] Q. Zhang, P. Hänggi, and J. Gong, New J. Phys. **10**, 073008 (2008).
[33] G. Heinrich, M. Ludwig, J. Qian, B. Kubala, and F. Marquardt, Phys. Rev. Lett. **107**, 043603 (2011).
[34] R. Lifshitz, E. Kenig, and M. C. Cross, in *Fluctuating Nonlinear Oscillators*, edited by M. T. Dykman (Oxford University Press, Oxford, to be published).

4.1.1 Supplement

Published as the Supplemental Material to *Physical Review Letters* **109**, 037205 (2012), reference [Fau12c].

Supplemental Material to "Non-adiabatic dynamics of two strongly coupled nanomechanical resonator modes"

T. Faust, J. Rieger, M. J. Seitner, P. Krenn, J. P. Kotthaus,* and E. M. Weig†
Center for NanoScience (CeNS) and Fakultät für Physik,
Ludwig-Maximilians-Universität, Geschwister-Scholl-Platz 1, München 80539, Germany
(Dated: May 2, 2012)

MODELING AND DATA ANALYSIS

Modeling the anticrossing

The two coupled differential equations for the displacements u_n (n=1,2) are

$$m_{\text{eff}}\frac{d^2u_1}{dt^2} + m_{\text{eff}}\gamma_1\frac{du_1}{dt} + k_1u_1 + k_c(u_1 - u_2) = 0 \tag{S1}$$

$$m_{\text{eff}}\frac{d^2u_2}{dt^2} + m_{\text{eff}}\gamma_2\frac{du_2}{dt} + k_2u_2 + k_c(u_2 - u_1) = 0, \tag{S2}$$

using the effective mass of the resonator (which, for a doubly clamped beam, is half its total mass) m_{eff}, the spring constants k_n, the coupling constant k_c and the two different damping constants γ_n. They are solved using an oscillatory ansatz $u_n = a_n e^{i\omega t}$. This leads to

$$-\omega^2 m_{\text{eff}}a_1 + k_1a_1 + k_c(a_1 - a_2) + im_{\text{eff}}\omega\gamma_1a_1 = 0 \tag{S3}$$

$$-\omega^2 m_{\text{eff}}a_2 + k_2a_2 + k_c(a_2 - a_1) + im_{\text{eff}}\omega\gamma_2a_2 = 0 \tag{S4}$$

which can be rewritten as

$$\begin{pmatrix} -\omega^2 m_{\text{eff}} + im_{\text{eff}}\omega\gamma_1 & 0 \\ 0 & -\omega^2 m_{\text{eff}} + im_{\text{eff}}\omega\gamma_2 \end{pmatrix}\vec{a} + \begin{pmatrix} k_1 + k_c & -k_c \\ -k_c & k_2 + k_c \end{pmatrix}\vec{a} = 0 \tag{S5}$$

$$\boldsymbol{\Omega}\vec{a} + \boldsymbol{K}\vec{a} = 0 \tag{S6}$$

using $\vec{a} = \begin{pmatrix} a_1 \\ a_2 \end{pmatrix}$ and by defining the two matrices $\boldsymbol{\Omega}$ and $\mathbf{K}$. By solving the eigenwert problem

$$\boldsymbol{\Omega}^{-1}\boldsymbol{K}\vec{a} = \lambda\vec{a} \tag{S7}$$

one can obtain the two (rather complicated) analytical solutions. The real part of these solutions contains the frequencies while the imaginary part describes the damping constants of the two branches.

Fitting the measured anticrossing

These two solutions are then simultaneously fitted to the measured frequencies and Q factors. We approximate $k_n = k_0 + \kappa_n(U - U_0) + \lambda_n(U - U_0)^2$. This is a second order series expansion of the parabolic frequency tuning [1, 2] around the crossing voltage U_0. The fit shown in Fig. 3 yields the following values: $k_0 = 3.2\,\frac{\text{N}}{\text{m}}$, $\kappa_1 = 9.3{\cdot}10^{-3}\,\frac{\text{N}}{\text{Vm}}$, $\kappa_2 = -12.5\cdot10^{-3}\,\frac{\text{N}}{\text{Vm}}$, $\lambda_1 = 0.41\cdot10^{-3}\,\frac{\text{N}}{\text{V}^2\text{m}}$, $\lambda_2 = -0.57\cdot10^{-3}\,\frac{\text{N}}{\text{V}^2\text{m}}$, $k_c = 3.76\cdot10^{-3}\,\frac{\text{N}}{\text{m}}$ and $U_0 = 6.547\,\text{V}$ using an effective mass of $m_{\text{eff}} = 1.85\cdot10^{-15}$g. As $|U - U_0|$ is always less than 3 V in the experiment, the maximal relative influence of the quadratic term $\frac{|U-U_0|\lambda_n}{\kappa_n}$ is below 15 %.

The fit in Fig. 3 shows only the measured frequencies, as the quality factors of the two modes are nearly identical. A resonator on a different chip which was tuned using the microwave power instead of the DC voltage [2], exhibited higher, dissimmilar, quality factors and thus allowed to simultaneously fit frequencies and quality factors. The resulting graphs are shown in Fig. S1. One can clearly see how the quality factors of the red and blue branch change as the system is tuned through the coupling region and the oscillation transforms from an in plane to an out of plane motion and vice versa.

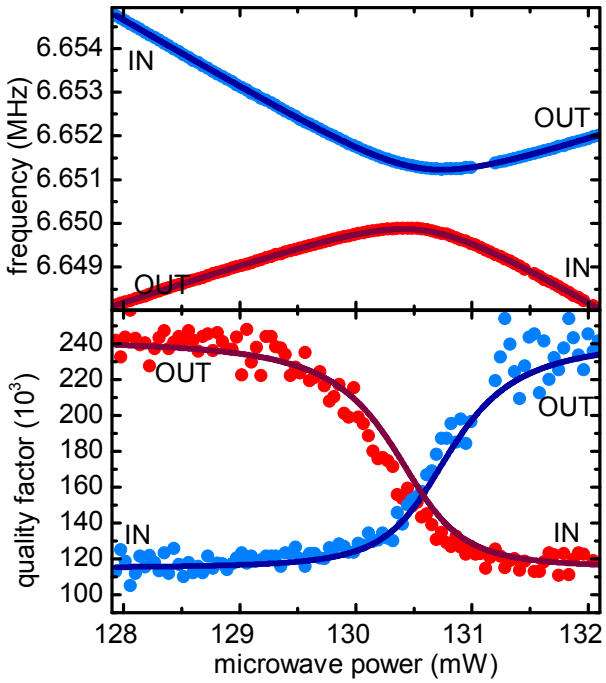

FIG. S1. Avoided crossing data and corresponding fit of a second resonator tuned via the microwave power, showing the coupling behavior of both frequency and quality factor. As the resonator modes are swept through the coupling region, the two branches transform from the high quality factor of the out of plane mode to the lower quality factor of the in plane mode and vice versa.

Analyzing the time-resolved data displayed in Fig. 4

For each ramp time τ, we measure the time-dependent power spectral density at points A and D of Fig. 2 with a bandwidth of 1 kHz to have sufficient time resolution. The measurement is started at $t = \tau$, but the data used for the analysis is the one taken after time $\delta = 3$ ms to avoid transient spikes in the measurement (as illustrated in Fig. 4a). The resulting exponential decays are then fitted using $S^{A,D}(t,\tau) = S_0^{A,D}(\tau)e^{-\gamma t} + S_{\text{Noise}}$, yielding the noise floor S_{Noise}, the damping constant γ, identical to the one determined from spectral measurements, and the mode energy at time τ $S_0^{A,D}(\tau)$ at points A and D.

Converting the measured data into transition probabilities

The transition probabilities of a classical Landau-Zener-Transition [3] are

$$P_{\text{dia}} = e^{\frac{-\pi\Gamma^2}{2\alpha}} \text{ and } \mathrm{P}_{\text{adia}} = 1 - \mathrm{P}_{\text{dia}}. \tag{S8}$$

By rewriting the change of the frequency difference between the two unperturbed states $\omega_n(U) = \sqrt{\frac{k_0+k_n(U)}{m_{\text{eff}}}}$

$$\alpha = \frac{\partial(\omega_1 - \omega_2)}{\partial t} = \frac{(\omega_1(U_i) - \omega_2(U_i)) - (\omega_1(U_f) - \omega_2(U_f))}{\tau} = \frac{\Delta\omega}{\tau}, \tag{S9}$$

P_{diab} can be expressed as a function of the ramp time τ and the measured frequency differences $\Delta\omega$ between the initial voltage U_i and the final voltage U_f, as the two voltages are kept constant throughout the experiment and only τ is varied. By introducing the mechanical damping term $e^{-\gamma t}$ at $t = \tau$, the probability is transformed into a normalized state population

$$S_{\text{dia}}(\tau) = e^{\frac{-\pi\Gamma^2\tau}{2\Delta\omega} - \gamma\tau} \tag{S10}$$

$$S_{\text{adia}}(\tau) = \left(1 - e^{\frac{-\pi\Gamma^2\tau}{2\Delta\omega}}\right) e^{-\gamma\tau}. \tag{S11}$$

The amplitudes of the two datasets $S_0^A(\tau)$ and $S_0^D(\tau)$ are then rescaled to fit these two equations. Both are shown in Fig. 4b of the main text along with the theoretical curves given in (S10). Note that Γ, γ and $\Delta\omega$ are already known from previous measurements and are no fit parameters.

COUPLING MECHANISM

Hybrid mode shapes

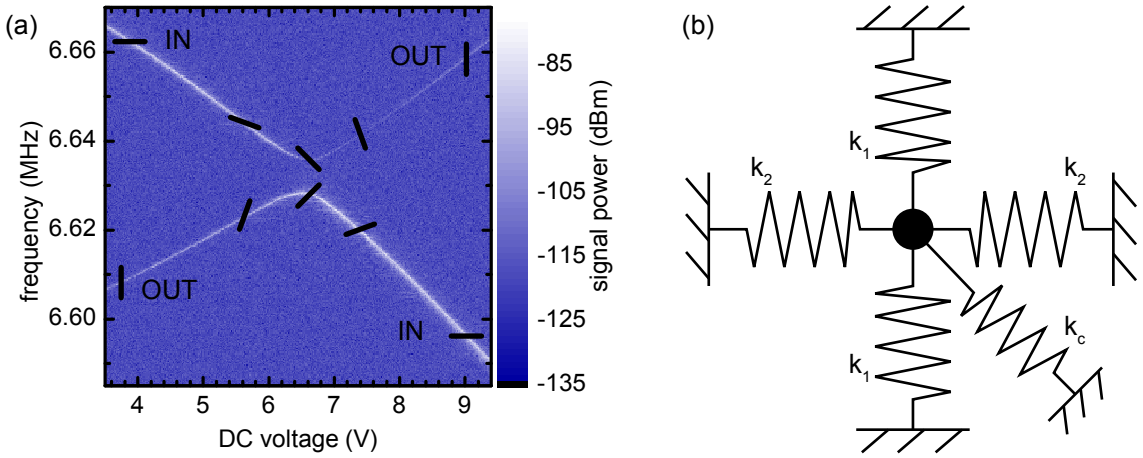

FIG. S2. The polarizations of the hybrid modes in the coupling region are sketched as black lines in the anticrossing diagram shown in (a). A horizontal line represents the in-plane and a vertical line represents the out-of-plane mode. The two hybrid modes exhibit polarization directions rotating in the plane perpendicular to the resonator. A mass on a spring model of the resonator with an asymmetric "coupling spring" is displayed in (b).

To learn more about the coupling and to understand how the transformation from an in-plane to an out-of-plane motion (or vice versa) takes place during an adiabatic transition, it is interesting to look at the spatial mode profiles in the anticrossing region. The solutions of the differential equations S1 and S2 are an in phase ($\omega = \sqrt{\frac{k}{m_{\mathrm{eff}}}}$) and an out of phase ($\omega = \sqrt{\frac{k+2k_c}{m_{\mathrm{eff}}}}$) combination of the fundamental mechanical modes. The mode polarizations and their qualitative evolution throughout the coupling region is sketched in Fig. S2(a), showing the transition between the pure in- and out-of-plane modes via the diagonal hybrid modes.

These two diagonal hybrid modes have different frequencies and thus different energies. In a perfectly symmetric beam with a rectangular cross section one would not expect any difference between the two diagonal modes, thus the coupling between the modes has to be connected to some asymmetry. This is visualized in Fig. S2(b): the two springs labeled k_1 provide the restoring force of the out-of-plane mode, the springs k_2 correspond to the in-plane mode. One can directly see from the schematic that the coupling spring k_c introduces an asymmetry into the system. One coupling mechanism, related to the asymmetric beam position between the electrodes, is discussed in the next section.

Electrical field coupling

A mechanical resonator chip with different gaps between the side electrodes and each beam exhibits different coupling constants Γ for each resonator. The smallest gap (of about 60 to 70 nm) yields $\Gamma = 7.77$ kHz (as presented in the main paper). Fitting the frequencies of the other beams in their respective coupling region gives a Γ of 7.27 ± 0.09 kHz, 6.10 ± 0.02 kHz and 5.31 ± 0.03 kHz with increasing gap size up to roughly 150 nm. As the electric field between the electrodes decreases with their increasing separation d (and the voltage is approximately constant), the coupling seems to be mediated by the electric field, even though the exact gap sizes are unknown and thus a quantitative relation can not be established.

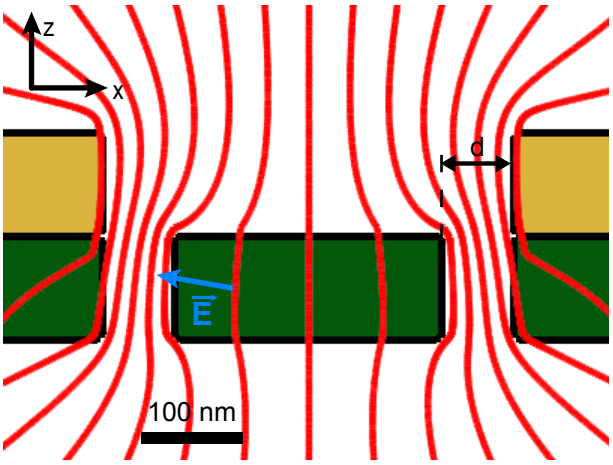

FIG. S3. The red lines of equal electric potential between the two electrodes (calculated using COMSOL finite element simulation) demonstrate the inhomogenous electric field (blue arrow) in x as well as z direction.

This electrical coupling between the in-plane mode (oscillating in x direction) and the out-of-plane mode (oscillating in z direction) can also be shown using the following simple model:
Starting from one undamped coupled equation (a simpler version of equation (S1))

$$F_x = k_x x + k_c(x - z), \tag{S12}$$

the coupling constant is just the derivative of F_x in z-direction:

$$\frac{\partial F_x}{\partial z} = -k_c \tag{S13}$$

The electric force on the dielectric beam is the gradient of its energy W in an external electric field $\vec{E}$

$$\vec{F_{\text{el}}} = -\vec{\nabla} W = -\vec{\nabla}(\vec{p} \cdot \vec{E}) = -\vec{\nabla}(\alpha E^2) \tag{S14}$$

using the polarizability α. Thus, the derivative of the x component of $\vec{F_{\text{el}}}$ in z direction yields a dielectric coupling term

$$\frac{\partial}{\partial z}\left(-\frac{\partial \alpha E^2}{\partial x}\right) = -\alpha \frac{\partial^2 E^2}{\partial z \partial x} = -k_{c,el} \tag{S15}$$

As there is a gradient of the electric field in z direction (the electrodes are above the beam) and in x direction (from asymmetry, otherwise the in-plane mode would not tune with the applied DC voltage), $k_{c,el}$ is not zero and contributes at least partially of the observed coupling strength. This is visualized in Fig. S3: if the beam is not perfectly aligned between the two electrodes, the resulting effective electric field exhibits a gradient in x and z direction. The field-dependent coupling mechanism also explains why the data shown in Fig. S1, measured with a DC voltage of 0 V, exhibits a weaker coupling of less than 2 kHz (the microwave field used to detect the beam motion also leads to an electric field, but the effective voltage is smaller). As the two modes can not be tuned into resonance without applying a (DC or microwave) electric field, it is not possible to test if there is also any purely mechanical coupling, e. g. caused by interactions between the modes mediated by the prestress of the beam or coupling effects in the shared clamping points of the two modes.

* kotthaus@lmu.de
† weig@lmu.de

[1] Q. P. Unterreithmeier, E. M. Weig, and J. P. Kotthaus, Nature **458**, 1001 (2009).
[2] T. Faust, P. Krenn, S. Manus, J. P. Kotthaus, and E. M. Weig, Nature Communications **3**, 728 (2012).
[3] L. Novotny, American Journal of Physics **78**, 1199 (2010).

4.2 Coherent control of a nanomechanical two-level system

Currently under review at *Nature Physics*, preprint available as *arXiv*:1212.3172 [cond-mat.mes-hall] (2012), reference [Fau12b].

Coherent control of a nanomechanical two-level system

Thomas Faust, Johannes Rieger, Maximilian J. Seitner, Jörg P. Kotthaus, and Eva M. Weig
Center for NanoScience (CeNS) and Fakultät für Physik,
Ludwig-Maximilians-Universität, Geschwister-Scholl-Platz 1, München 80539, Germany

The Bloch sphere is a generic picture describing a coupled two-level system and the coherent dynamics of its superposition states under control of electromagnetic fields [1]. It is commonly employed to visualise a broad variety of phenomena ranging from spin ensembles [2] and atoms [3] to quantum dots [4] and superconducting circuits [5]. The underlying Bloch equations [6] describe the state evolution of the two-level system and allow characterising both energy and phase relaxation processes in a simple yet powerful manner [2, 7, 8].

Here we demonstrate the realisation of a nanomechanical two-level system which is driven by radio frequency signals. It allows to extend the above Bloch sphere formalism to nanoelectromechanical systems. Our realisation is based on the two orthogonal fundamental flexural modes of a high quality factor nanostring resonator which are strongly coupled by a dielectric gradient field [9]. Full Bloch sphere control is demonstrated via Rabi [10], Ramsey [11] and Hahn echo [12] experiments. This allows manipulating the classical superposition state of the coupled modes in amplitude and phase and enables deep insight into the decoherence mechanisms of nanomechanical systems. We have determined the energy relaxation time T_1 and phase relaxation times T_2 and T_2^*, and find them all to be equal. This not only indicates that energy relaxation is the dominating source of decoherence, but also demonstrates that reversible dephasing processes are negligible in such collective mechanical modes. We thus conclude that not only T_1 but also T_2 can be increased by engineering larger mechanical quality factors. After a series of ground-breaking experiments on ground state cooling and non-classical signatures of nanomechanical resonators in recent years [13–17], this is of particular interest in the context of quantum information processing [1, 18] employing nanomechanical resonators [19, 20].

While the dynamics of a two-level system under the influence of a pulsed external electromagnetic field was observed in atomic and nuclear spin physics decades ago, a mechanical analogon to such a system remained elusive for a long time. Only recently, coherent exchange of energy quanta between a mechanical and an electrical mode was achieved: In 2010, O'Connell et al. [13] managed to control the swapping of a single quantum of energy between a qubit and a mechanical resonator, while Palomaki et al. [17] demonstrated the temporary storage of itinerant microwave photons in a mechanical resonator in 2012. At the same time, several approaches were employed to achieve purely mechanical resonant coupling either between separate resonators [21–23] or different modes of the same resonator [9, 24] in the classical regime. So far, the pulsed coherent control of the system was prevented by weak coupling, low quality factors or the lack of a sufficiently strong and fast tuning mechanism.

We present the successful implementation of a purely mechanical two-level system with coherent time-domain control (see also the experiments independently performed at NTT using parametric coupling [26]). To this end, we use a 250 nm wide and 100 nm thick, strongly stressed [27] silicon nitride beam resonator with a length of 50 µm dielectrically coupled to a pair of electrodes used for detection [25] as well as actuation and tuning [28]. The two fundamental flexural modes of the mechanical resonator oscillating in the out-of-plane and in-plane direction (see Fig. 1) are coupled by cross-derivatives of the strong inhomogeneous electric field generated between the electrodes [9]. A constant dc voltage of -15 V is used to dielectrically tune the system close to the resulting avoided crossing, while the signals generated by an arbitrary waveform generator (AWG) enable time-resolved control vicinal to the anticrossing (see Fig. 1b,c). Both voltages are added and combined with the rf actuation of the beam via a bias-tee and applied to one electrode. The other electrode is connected to a 3.6 GHz microstrip cavity, enabling heterodyne detection of the beam deflection [25] after addition of a microwave bypass capacitor at the first electrode [28]. These components as well as the mechanical resonator are placed in a vacuum of $\leq 10^{-4}$ mbar and cooled to 10.00 ± 0.02 K to improve the temperature stability as well as cavity quality factor. The microwave cavity is interfaced to the readout with a single coaxial cable and a circulator.

When the system is driven by an external white noise source and the AWG output voltage is swept, the avoided crossing of the two modes shown in Fig. 1c can be mapped out, exhibiting a frequency splitting $\Omega = 24,249 \pm 4$ Hz. With a quality factor $Q = \frac{f}{\Delta f} \approx 2 \cdot 10^5$ and a linewidth of $\Delta f \approx 40$ Hz at the resonance frequency f, the system is clearly in the strong coupling regime of $\Delta f \ll \Omega$. For all measurements discussed in the following, an rf drive of -59 dBm at 7.539 MHz, resonantly actuating the beam at an AWG voltage of 0 V, is applied, which initialises the system in its in-plane mode (see black circle in Fig. 1c).

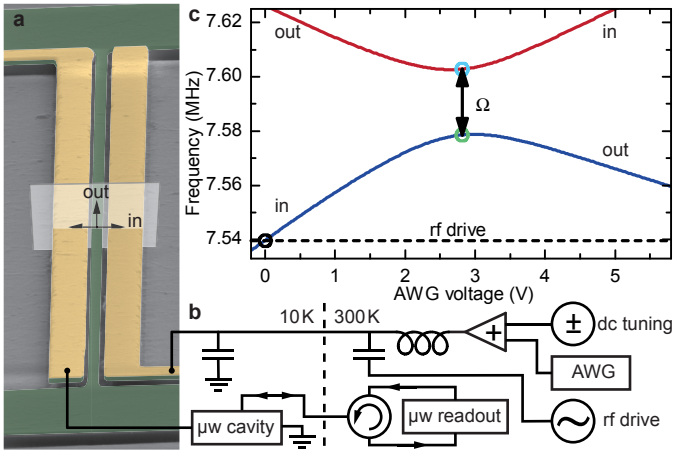

FIG. 1. **Nanoelectromechanical system.** **a**, SEM micrograph showing oblique view of the 50 μm long silicon nitride beam (green) and the adjacent, 1 μm wide gold electrodes (yellow), processed on top of the SiN. **b**, Electrical setup: the output of the arbitray waveform generator (AWG) and a dc tuning voltage are added and combined with the rf drive via a bias-tee. The second capacitor acts as a bypass providing a μw ground path for the microwave detection [25], which is connected to the other electrode. **c**, Resonance frequencies of the out-of-plane (out) and in-plane (in) mode of the resonator controlled by the AWG voltage at a constant dc tuning voltage of -15 V. The black circle marks the initialisation state at 0V and the frequency of the rf drive, while the green and blue circles correspond to the lower and upper state of the two-level system, respectively, separated by the frequency splitting Ω.

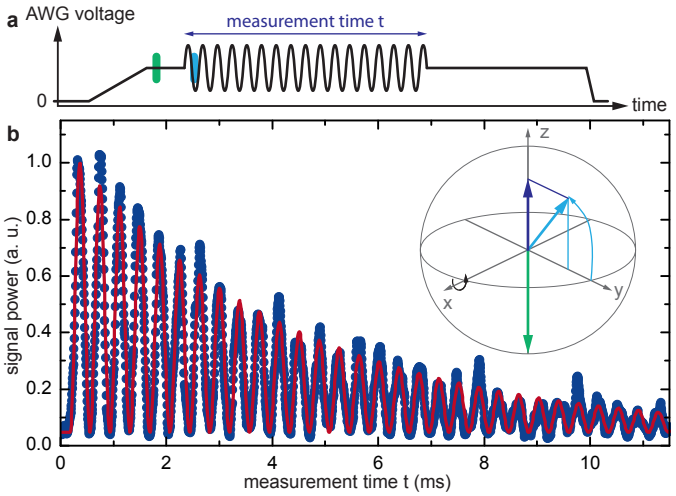

FIG. 2. **Rabi oscillations.** **a**, Pulse scheme: the system is adiabatically tuned from the initialisation to the lower state, then a constant drive with frequency Ω is turned on. **b**, The z projections of the decaying Rabi oscillations (data: dark blue; fit: red) can be directly measured with a spectrum analyser. The Bloch sphere in the inset shows the state of the Bloch vector at selected times, which are marked in the same colour in **a**.

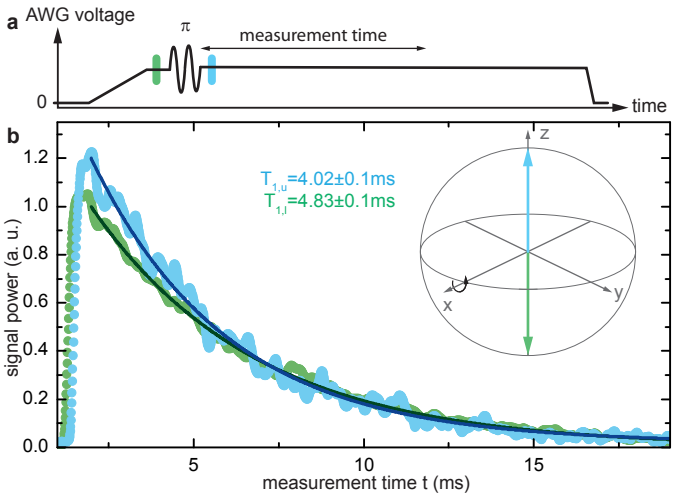

FIG. 3. **Energy relaxation.** **a**, Pulse scheme: the system is adiabatically tuned from the initialisation to the lower state. An additional π-pulse is used to rotate it to the upper state. **b**, Measured exponential decay of the lower (data: green; fit: dark green) and upper (data: blue; fit: dark blue) state. The Bloch sphere in the inset shows the state of the Bloch vector at selected times, which are marked in the same colour in **a**.

A 1 ms long, adiabatic voltage ramp up to 2.82 V brings the state to the point of minimal frequency splitting Ω between the coupled modes. Here, the system dynamics is described by two hybrid modes formed by the in-phase and out-of-phase combinations of the fundamental flexural modes. The adiabatic ramp thus transforms all the energy of the in-plane mode into the lower hybrid state, such that the two-level system, consisting of the two hybrid modes, is prepared in its lower state. As the drive frequency remains constant (dashed line in Fig. 1c), the beam is no longer actuated and its energy is slowly decaying.

Now, the application of a continuous pump tone with frequency Ω will start Rabi oscillations [2, 10] between the lower and upper state, as shown in Fig. 2. They can be measured directly by monitoring the time evolution of the output power spectrum at the frequency of one of the hybrid modes, here shown for the upper state at 7.6028 MHz, and measured with a bandwidth of 10 kHz. All time-resolved measurements are averaged over 20 (Rabi oscillations and T1 measurement) or 10 pulse sequences (Ramsey fringes and Hahn echo). For a drive amplitude of 100 mV (half peak-to-peak) we find a Rabi frequency of 8.3 kHz (see section II.A of the Supplementary Information for the frequency dependence of the Rabi oscillations). In principle, the decay of these oscillations is governed by both energy relaxation, characterised by a rate $1/T_1$, and phase decoherence, characterised by $1/T_2$ or $1/T_2^*$, where $T_2^* \leq T_2$ includes reversible processes caused by slow fluctuations or spatial inhomogeneity of the coupling. For clarity, we use these well-known phenomenological constants in the same way as, e. g., in spin systems [2], as discussed in more detail in the Supplementary Information section I.

The exponential decay of a state's energy defines T_1. The corresponding measurement is shown in Fig. 3 for both lower and upper state: The system is once again prepared in the lower hybrid state. To reach the upper state, a subsequent π-pulse is applied, thus performing one half of a Rabi cycle which transfers the system to the upper state (see Supplementary Information section II for details on the frequency and amplitude calibration of the applied pulses). The exponential decay is then measured directly with a spectrum analyser at a bandwidth of 3 kHz, exhibiting different relaxation times $T_{1,l} = 4.83 \pm 0.1$ ms and $T_{1,u} = 4.02 \pm 0.1$ ms for the lower and upper mode, respectively. They correspond to the spectrally measured quality factors. Previously, it has been shown that, at maximum coupling, the two hybrid modes should have the same quality factor and thus T_1 time [9]. However, both modes are affected by dielectric damping [28], leading to the observed difference.

To measure the T_2^* time, a $\pi/2$-pulse is used after the preparation in the lower state to bring the system into a superposition state between lower and upper hybrid mode. The frequency of the pulse is detuned to $\Omega + 500$ Hz, leading to a slow precession of the state vector around the z-axis of the Bloch sphere [2, 11]. As a result, a second $\pi/2$-pulse after time τ does not always bring the system into the upper state, but a slow oscillation, the so-called Ramsey fringes, is observed when the delay τ between the two pulses is varied and the z-projection of the state vector is measured after the second pulse, as shown in Fig. 4. The decay constant of this oscillation is T_2^*, while the decay of the mean value corresponds to an effective T_1 of both modes. The fit in Fig. 4b results in $T_2^* = 4.44 \pm 0.1$ ms and $T_1 = 4.31 \pm 0.1$ ms. The energy relaxation time of the superposition state T_1 is identical to the reciprocal rate average of the two hybrid modes

$$\overline{T_1} = 2\left(\frac{1}{T_{1,l}} + \frac{1}{T_{1,u}}\right)^{-1} = 4.39\,\text{ms},$$

as the mechanical energy oscillates between the two modes with frequency Ω (see Supplemental Video).

By including an additional π-pulse at $\tau/2$ into the Ramsey pulse scheme and replacing the final $\pi/2$-pulse by an $3\pi/2$-pulse to once again rotate to the upper state (see Fig. 5), the T_2 time can be measured in a Hahn echo experiment [2, 12]. The 180° rotation flips the state vector in the xy-plane of the Bloch sphere, thus reversing the effects of a fluctuating or inhomogeneous coupling strength Ω in the second delay interval of $\tau/2$ and thereby canceling their contribution. The frequency of the pulses is once again exactly Ω, as all three pulses need to be applied exactly around the same axis. The resulting decay curve represents T_2, for which a value of $T_2 = 4.35 \pm 0.1$ ms can be extracted from the fit in Fig. 5b.

The good agreement between T_2 and T_2^* clearly shows that reversible elastic dephasing, e. g. caused by tem-

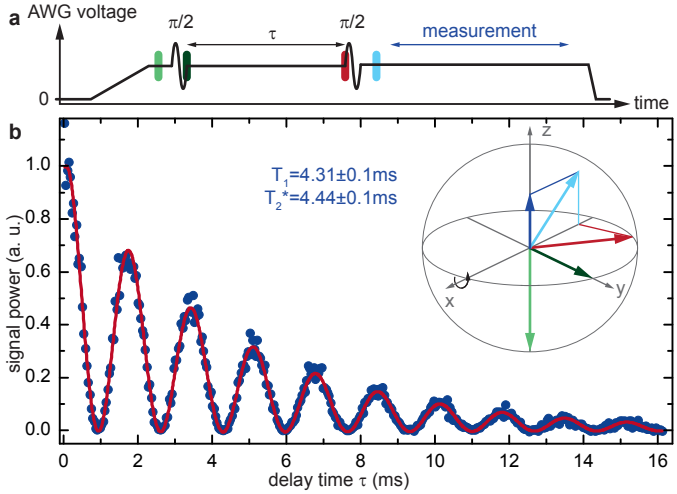

FIG. 4. **Ramsey fringes.** **a**, Pulse scheme: the system is adiabatically tuned from the initialisation to the lower state. A $\pi/2$-pulse creates a superposition state, and after a delay τ a second $\pi/2$-pulse is applied. **b**, A 500 Hz detuning between drive and precession frequency leads to a slow rotation of the superpostion state in the equator plane of the Bloch sphere, giving rise to a beating pattern in the measured z component after the second pulse (data: dark blue; fit: red). The Bloch sphere in the inset shows the state of the Bloch vector at selected times, which are marked in the same colour in **a**.

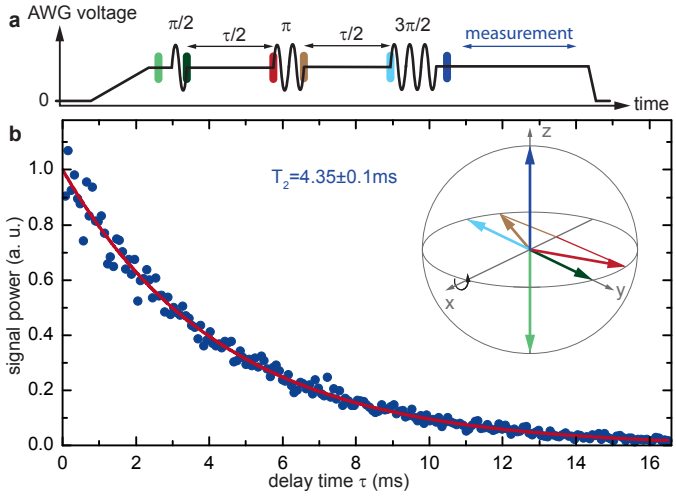

FIG. 5. **Hahn echo.** **a**, Pulse scheme: the system is adiabatically tuned from the initialisation to the lower state. A $\pi/2$-pulse creates a superposition state, and after a delay $\tau/2$ a π-pulse mirrors the state vector to the other half of the Bloch sphere. After another delay of $\tau/2$ a $3\pi/2$-pulse is used to rotate to the upper state. **b**, The inverse evolution of the system during the two delay times cancels out any broadening or slow precession effects, thus the system always ends up along the z-axis and no oscillation is observed (data: dark blue; fit: red). The Bloch sphere in the inset shows the state of the Bloch vector at selected times, which are marked in the same colour in **a**.

poral and spatial enviromental fluctuations or spatial inhomogeneities, does not noticeably increase decoherence. Although the experiment is performed with billions of phonons, they all reside in the same collective mechanical mode and thus all experience an identical environment. This strongly constrasts the behaviour found e. g. in spin qubits, where the hyperfine interaction with energetically degenerate nuclear spins causes $T_2^* \ll T_2$ (see Supplemental Information section III).

It is more surprising that the phase coherence time T_2 is equal to the average energy relaxation time T_1. This indicates the absence of measurable elastic phase relaxation processes in the nanomechanical system, such that the observed loss of coherence is essentially caused by the energy decay of the mechanical oscillation (see also Supplemental Information section III). Earlier research [27] suggests that the dominant relaxation mechanism in silicon nitride strings is mediated by localised defect states of the amorphous resonator material, described as two-level systems at low temperature. They facilitate energy relaxation by providing the momentum required to transform a resonator phonon into a bulk phonon. For this process to lead to elastic phase relaxation, an excited defect state would have to re-emit the phonon back into the resonator mode, which is extremely unlikely due to the weak coupling between the two. In conclusion, we demonstrate coherent electrical control of a strongly coupled ($\Omega \gg \frac{f}{Q}$) nanomechanical two-level system, employing the pulse techniques well-known from coherent spin dynamics in the field of nanomechanics. Each superposition state of the two hybrid modes on the Bloch sphere can be addressed by a sequence of the described pulses. The presented system stands out by the finding that the elastic phase relaxation rate Γ_φ is negligible compared to the energy decay rate $\frac{2\pi f}{Q}$, leaving room for improvement of the coherence via increased quality factors.

In light of the recent breakthrough in ground-state cooling of nanomechanical resonators [13–16], the coherent manipulation schemes presented here open new applications for nanomechanical systems in quantum information. Not only can they be used as efficient interfaces for quantum state transfers in hybrid quantum systems [19, 29], but by creating coupled, quantised resonators [30] quantum computations can be carried out directly using nanoelectromechanical two-level systems [20].

ACKNOWLEDGEMENTS

Financial support by the Deutsche Forschungsgemeinschaft via Project No. Ko 416/18, the German Excellence Initiative via the Nanosystems Initiative Munich (NIM) and LMUexcellent, as well as the European Commission under the FET-Open project QNEMS (233992) is gratefully acknowledged. We thank G. Burkard for his comments on decoherence in a three-level system and H. Okamoto, I. Mahboob and H. Yamaguchi for critically reading the manuscript.

COMPETING INTERESTS

The authors declare that they have no competing financial interests.

AUTHOR CONTRIBUTIONS

J.R. and M.J.S. designed and fabricated the sample, T.F. conducted the measurements and analysed the data. T.F., J.P.K. and E.M.W. wrote the paper with input from the other authors, the results were discussed by all authors.

CORRESPONDENCE

Correspondence and requests for materials should be addressed to E.M.W. (email: weig@lmu.de).

[1] Nielsen, M. A. & Chuang, I. L. *Quantum Computation and Quantum Information* (Cambridge University Press, 2000).
[2] Vandersypen, L. M. K. & Chuang, I. L. NMR techniques for quantum control and computation. *Rev. Mod. Phys.* **76**, 1037–1069 (2005).
[3] Haroche, S. & Raimond, J.-M. *Exploring the Quantum: Atoms, Cavities, and Photons* (Oxford University Press, USA, 2006).
[4] Hanson, R. & Awschalom, D. D. Coherent manipulation of single spins in semiconductors. *Nature* **453**, 1043–1049 (2008).
[5] You, J. Q. & Nori, F. Atomic physics and quantum optics using superconducting circuits. *Nature* **474**, 589–597 (2011).
[6] Bloch, F. Nuclear Induction. *Phys. Rev.* **70**, 460–474 (1946).
[7] Yafet, Y. g Factors and Spin-Lattice Relaxation of Conduction Electrons. *Solid State Physics* **14**, 1–98 (1963).
[8] Burkard, G., Koch, R. H. & DiVincenzo, D. P. Multilevel quantum description of decoherence in superconducting qubits. *Phys. Rev. B* **69**, 064503 (2004).
[9] Faust, T. *et al.* Nonadiabatic Dynamics of Two Strongly Coupled Nanomechanical Resonator Modes. *Phys. Rev. Lett.* **109**, 037205 (2012).
[10] Rabi, I. I. Space Quantization in a Gyrating Magnetic Field. *Phys. Rev.* **51**, 652–654 (1937).
[11] Ramsey, N. F. A Molecular Beam Resonance Method with Separated Oscillating Fields. *Phys. Rev.* **78**, 695–699 (1950).
[12] Hahn, E. L. Spin Echoes. *Phys. Rev.* **80**, 580–594 (1950).

[13] O'Connell, A. D. *et al.* Quantum ground state and single-phonon control of a mechanical resonator. *Nature* **464**, 697–703 (2010).

[14] Teufel, J. D. *et al.* Sideband cooling of micromechanical motion to the quantum ground state. *Nature* **475**, 359–363 (2011).

[15] Chan, J. *et al.* Laser cooling of a nanomechanical oscillator into its quantum ground state. *Nature* **478**, 89–92 (2011).

[16] Safavi-Naeini, A. H. *et al.* Observation of Quantum Motion of a Nanomechanical Resonator. *Phys. Rev. Lett.* **108**, 033602 (2012).

[17] Palomaki, T. A., Harlow, J. W., Teufel, J. D., Simmonds, R. W. & Lehnert, K. W. State Transfer Between a Mechanical Oscillator and Microwave Fields in the Quantum Regime. *ArXiv e-prints* (2012). 1206.5562.

[18] Ladd, T. D. *et al.* Quantum computers. *Nature* **464**, 45–53 (2012).

[19] Stannigel *et al.* Optomechanical transducers for long-distance quantum communication. *Phys. Rev. Lett.* **105**, 220501 (2010).

[20] Rips, S. & Hartmann, M. J. Quantum Information Processing with Nanomechanical Qubits. *ArXiv e-prints* (2012). 1211.4456.

[21] Perisanu, S. *et al.* The mechanical resonances of electrostatically coupled nanocantilevers. *Applied Physics Letters* **98**, 063110 (2011).

[22] Okamoto, H., Kamada, T., Onomitsu, K., Mahboob, I. & Yamaguchi, H. Optical Tuning of Coupled Micromechanical Resonators. *Applied Physics Express* **2**, 062202 (2009).

[23] Karabalin, R. B., Cross, M. C. & Roukes, M. L. Nonlinear dynamics and chaos in two coupled nanomechanical resonators. *Phys. Rev. B* **79**, 165309 (2009).

[24] Kozinsky, I., Postma, H. W. C., Bargatin, I. & Roukes, M. L. Tuning nonlinearity, dynamic range, and frequency of nanomechanical resonators. *Applied Physics Letters* **88**, 253101 (2006).

[25] Okamoto, H. *et al.* Coherent phonon manipulation in coupled mechanical resonators. *submitted to Nature* (2012).

[26] Unterreithmeier, Q. P., Faust, T. & Kotthaus, J. P. Damping of Nanomechanical Resonators. *Phys. Rev. Lett.* **105**, 027205 (2010).

[27] Faust, T., Krenn, P., Manus, S., Kotthaus, J. P. & Weig, E. M. Microwave cavity-enhanced transduction for plug and play nanomechanics at room temperature. *Nat Commun* **3**, 728 (2012).

[28] Rieger, J., Faust, T., Seitner, M. J., Kotthaus, J. P. & Weig, E. M. Frequency and Q factor control of nanomechanical resonators. *Applied Physics Letters* **101**, 103110 (2012).

[29] Meystre, P. A short walk through quantum optomechanics. *arXiv:1210.3619* (2012).

[30] Brown, K. R. *et al.* Coupled quantized mechanical oscillators. *Nature* **471**, 196–199 (2011).

4.2.1 Supplement

Supplemental Material to *arXiv*:1212.3172 [cond-mat.mes-hall] (2012), reference [Fau12b].

I. RELAXATION TIMES

In the main text, the relaxation constants T_1 and T_2 are introduced phenomenologically to define the exponential decay times extracted from the energy relaxation and Hahn echo experiments. But different from the two-state spin systems associated with experiments on the Bloch sphere, the mechanical system investigated here actually has three states: the two coupled hybrid modes, i. e. the lower and upper state as well as the ground state (the thermally occupied phonon bath) into which a phonon can relax from either mode, see Figure S1.

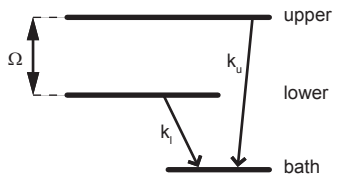

FIG. S1. **Levels of the mechanical system:** Schematic representation of the phonon bath and the upper and lower hybrid state of the mechanical system, separated by the frequency splitting Ω, with respective decay constants k_u and k_l.

For one, this makes it necessary to prepare the lower state prior to any measurement, as none of the states of the nanomechanical two-level system is automatically populated (except for the comparatively weak thermal excitation). Furthermore, it introduces additional terms to the Bloch equations: Assuming two independent decay rates k_u and k_l for the upper and lower state and following reference [31], the rotating-frame Bloch equations can be written as

$$\dot{M}_x(t) = -\underbrace{\left(\frac{1}{T_\perp} + \overline{k}\right)}_{1/T_2} M_x(t) + \Delta M_y(t) \tag{S1}$$

$$\dot{M}_y(t) = -\underbrace{\left(\frac{1}{T_\perp} + \overline{k}\right)}_{1/T_2} M_y(t) - \Delta M_x(t) - \omega_R M_z(t) \tag{S2}$$

$$\dot{M}_z(t) = -\underbrace{\left(\frac{1}{T_\parallel} + \overline{k}\right)}_{1/T_1} M_z(t) + \omega_R M_y(t) \tag{S3}$$

Here, Δ is the detuning between drive frequency and coupling strength Ω and ω_R reflects the drive strength and corresponds to the frequency of Rabi oscillations. $\overline{k} = \frac{k_u + k_l}{2}$ is the average decay rate, $T_\perp$ the relaxation time in the equator plane of the Bloch sphere, $T_\parallel$ the relaxation time along the z direction and M_x, M_y and M_z denote the respective components of the state vector. The phenomenological parameters $1/T_1$ and $1/T_2$ can be identified as the sum of the respective rates.

The measured values of T_1 are consistent with the quality factors of the corresponding modes, which are only limited by k_u and k_l. This implies a negligibly small $1/T_\parallel$. As the measurements show that T_1 is equal to T_2, $1/T_\perp$ must also be negligible. Thus, the two coherence times T_1 and T_2 are solely limited by the average mechanical damping of the two resonator modes.

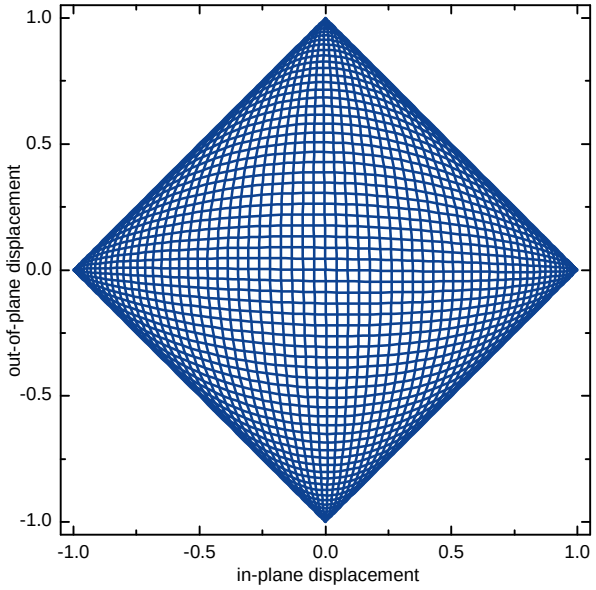

FIG. S2. **Oscillation in the superposition state:** The normalized displacement of the resonator is calculated for one full precession period in the superposition state, i. e. for equal amplitudes of the lower and upper state. This phase trajectory is plotted in the basis of the in-plane and out-of-plane mode (horizontal and vertical axis of the plot).

Reference 31 also introduces an additional term in equation S3 taking into account the difference between the two decay rates k_u and k_l. It leads to a slow tilt of the state vector of a superposition state away from the equator plane towards the state with the smaller decay rate. However, this effect plays no role in the classical system presented here: In a classical superposition state, the energy is distributed between both modes. The system performs an oscillation between its two fundamental modes, changing the direction of rotation with the precession frequency. Thus, the time spent in each mode is equal, and the state just experiences the average decay constant. A plot of the phase space trajectory for one precession cycle is shown in Figure S2, using a 10 times exaggerated coupling strength. The horizontal and vertical axes correspond to an in-plane and out-of-plane oscillation, while a diagonal motion is associated with the lower and upper hybrid mode. An animated version of this plot is available as a Supplementary Video.

II. PULSE CALIBRATION

The first step in characterising the system is to measure an avoided crossing as shown in Figure 1 of the main text. From its fit, the approximate frequency splitting Ω and the AWG voltage required to adiabatically tune to the lower state is extracted [9].

A. Pulse frequency

To precisely determine the correct pump tone, the fitted frequency splitting is not accurate enough. Instead, the frequency of Rabi oscillations is monitored while sweeping the pump frequency. The quadratic dependence for small detunings [2], as shown in Figure S3, allows to fit the measured points and extract the lowest Rabi frequency and thus the exact pump frequency corresponding to zero detuning.

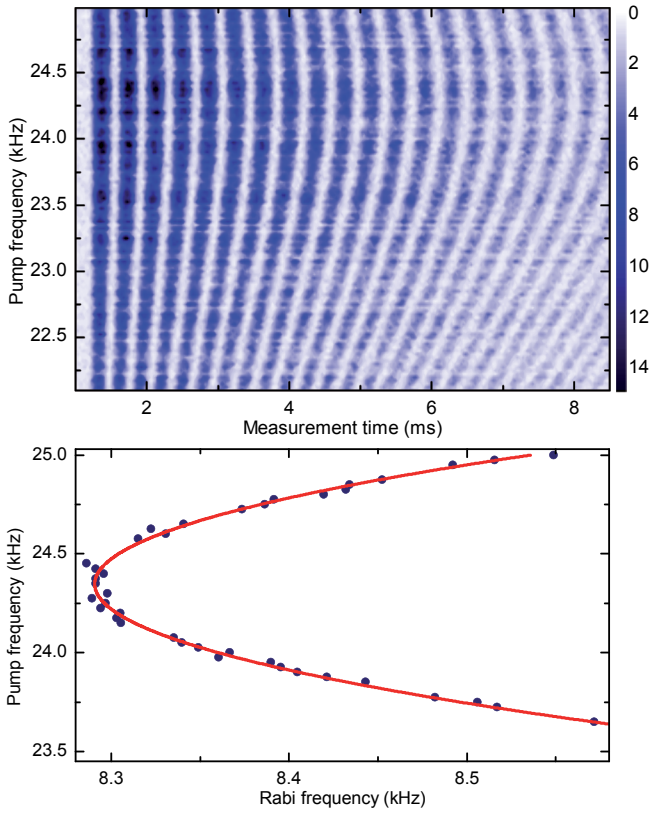

FIG. S3. **Pump frequency tuning:** The frequency of Rabi oscillations depends quadratically on the pump frequency detuning. The upper plot displays the measured signal power colour-coded versus pump frequency and measurement time. The extracted Rabi frequencies (blue points: data; red line: parabolic fit) are shown in the lower plot. The minimum of the parabola corresponds to the zero-detuning pump frequency.

B. Pulse length and spacing

The pulses applied to the system should be as short as possible to allow fast control sequences. The lower limit of the pulse length is one period of the pump signal, as abrupt voltage jumps of a chopped up sine wave will disturb the system. The shortest applied pulse (a $\pi/2$ pulse) is thus set to a duration of 1/(pump frequency) so that it consists of exactly one sine wave. The other pulses are correspondingly longer, as shown in the pulse schemes in Figures 3-5 of the main text.

The delay time between two pulses in Figure 4 and 5 also needs to be a multiple of 1/(pump frequency), as otherwise the second rotation will not be carried out along the same axis. This is apparent from the Ramsey fringe experiment, where the observed beating pattern, and thus the effective rotation angle, is caused by an intentional detuning of 500 Hz.

C. Pulse amplitude

After both length and frequency of a pulse are fixed as described above, its amplitude has to be adjusted to define the rotation angle achieved with each pulse. To this end, four sine periods (i. e. a $4 \cdot \pi/2 = 2\pi$ pulse at the desired amplitude) are applied to the system, varying the amplitude. The population of the upper state is measured. At zero amplitude, the pulse has no effect and all energy remains in the lower state. With increasing amplitude, the achieved rotation angle increases, and the first minimum corresponds to the desired 2π character of the pulse. The population P_u of the upper state can be described as

$$P_u = \sin\left(\frac{\pi A}{A_0}\right)^2, \tag{S4}$$

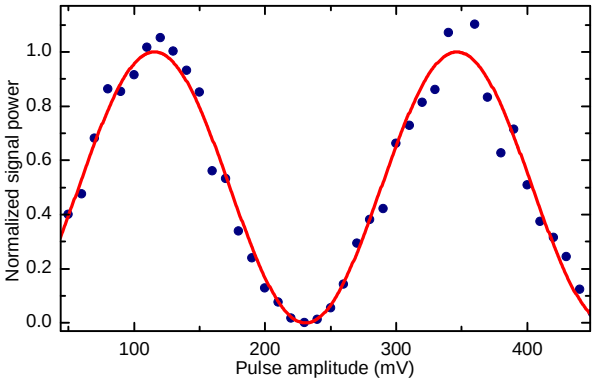

FIG. S4. **Pulse amplitude sweep:** The population of the upper state after quadruple-sine-wave pulses of different amplitudes (blue points: data; red line: fit) demonstrates the correct behaviour for an amplitude of 231 mV.

where A is the pulse amplitude and A_0 the amplitude corresponding to a rotation of 2π. A fit to the measured data, as shown in Figure S4, can be used to extract the correct pulse amplitude. This measurement has to be repeated with the detuned pump frequency used for the Ramsey fringes experiment, as the slightly different frequency also leads to a small shift in the amplitude of the pulse.

III. PHASE RELAXATION

To define the elastic phase relaxation rate Γ_φ two situations have to be distinguished: In systems where energy relaxation occurs only from the upper to the lower level (e.g. references [8,32]) the phase relaxation rate is defined as[31,33,34]

$$\Gamma_\varphi = \frac{1}{T_2} - \frac{1}{2T_1}. \tag{S5}$$

In contrast to that, in a system dominated by spontaneous decay to a third state and no relaxation between the upper and lower level [33,34] (i. e. $1/T_\parallel = 0$ and finite $\overline{k}$, see equation S3), the phase relaxation rate Γ_φ, in this case equal to $1/T_\perp$ (defined in equation S1 and equation S2), is given as

$$\Gamma_\varphi = \frac{1}{T_2} - \frac{1}{T_1}. \tag{S6}$$

This is the case for the system presented here. As T_1 and T_2 are equal within the measurement accurracy, Γ_φ can not be determined from the experiment. This shows that the measured phase decoherence is solely caused by energy relaxation. Processes changing the phase but preserving the state's energy seem to play no role.

To compare this mechanical two-level system to other coherent systems, it helps to take a general look at the possible decay processes: Inelastic processes in which energy is transfered to a thermal bath are irreversible. They are directly represented in the T_1 time and also pose a limit to T_2 via the two above equations S5 or S6. Irreversible elastic interactions lead to a non-zero Γ_φ and thus reduce T_2, whereas reversible phase decay processes can be measured and controlled e. g. by a Hahn echo experiment and only decrease T_2^*.

In most coherent nanoscale solid-state systems, the coupling to a fluctuating thermal bath of phonons, photons, two-level systems or (nuclear) spins leads to one or more of the above processes. For example, superconducting qubits [35–37] suffer from flux, charge and photon noise. In gate-defined spin qubits e. g. nuclear spin [38–40] and phonon [41] interactions limit the performance, whereas NV centres in diamond [42] couple to the surrounding nuclear spin bath. In the amorphous dielectric system presented here, relevant loss mechanisms occur via defect states with a broad energy spectrum often associated with two-level systems [43], and the phononic environment, as long as no additional electronic noise is introduced via the measurement devices and tuning voltages. As the mechanical modes under investigation are situated within the suspended beam, they effectively reside inside a phonon cavity and couple extremely weakly to the phonon bath of the bulk sample via the narrow clamping points [44]. The exchange of energy of the discrete long-wavelength resonator modes and the continous shorter-wavelength phonon spectrum of the beam is found to be mediated by the defects. As only higher energy phonons with small wavelengths can effectively transmit energy through the clamps to the bath, scattering of thermally excited higher energy phonons at defect states in a three particle interaction is the most likely process. These inelastic processes destroy energy as well as phase and likely explain why we find $T_1 = T_2$.

SUPPLEMENTARY REFERENCES

2. Vandersypen, L. M. K. & Chuang, I. L. NMR techniques for quantum control and computation. *Rev. Mod. Phys.* **76**, 1037–1069 (2005).

8. Burkard, G., Koch, R. H. & DiVincenzo, D. P. Multilevel quantum description of decoherence in superconducting qubits. *Phys. Rev. B* **69**, 064503 (2004).

9. Faust, T. *et al.* Nonadiabatic Dynamics of Two Strongly Coupled Nanomechanical Resonator Modes. *Phys. Rev. Lett.* **109**, 037205 (2012).

31. Pöttinger, J. & Lendi, K. Generalized Bloch equations for decaying systems. *Phys. Rev. A* **31**, 1299–1309 (1985).

32. Hu, X., de Sousa, R. & Sarma, S. D. Decoherence and dephasing in spin-based solid state quantum computers. *Proceedings of the 7th International Symposium on Foundations of Quantum Mechanics in the Light of New Technology, eds. Yoshimasa A. Ono, K. Fujikawa und Kazuo Fujikawa, World Scientific (or: cond-mat/0108339)* 3–11 (2002).

33. Drake, G. W. F. (ed.) *Springer Handbook of Atomic, Molecular, and Optical Physics*, page 1004 (Springer, 2006).

34. Burkard, G. *Private communication* (2012).

35. Houck, A., Koch, J., Devoret, M., Girvin, S. & Schoelkopf, R. Life after charge noise: recent results with transmon qubits. *Quantum Information Processing* **8**, 105–115 (2009).

36. McDermott, R. Materials origins of decoherence in superconducting qubits. *IEEE Transactions on Applied Superconductivity* **19**, 2 – 13 (2009).

37. Rigetti, C. *et al.* Superconducting qubit in a waveguide cavity with a coherence time approaching 0.1 ms. *Phys. Rev. B* **86**, 100506 (2012).

38. Petta, J. R. *et al.* Coherent manipulation of coupled electron spins in semiconductor quantum dots. *Science* **309**, 2180–2184 (2005).

39. Reilly, D. J. *et al.* Suppressing spin qubit dephasing by nuclear state preparation. *Science* **321**, 817–821 (2008).

40. Bluhm, H. *et al.* Dephasing time of GaAs electron-spin qubits coupled to a nuclear bath exceeding 200 µs. *Nat Phys* **7**, 109–113 (2011).

41. Hanson, R., Kouwenhoven, L. P., Petta, J. R., Tarucha, S. & Vandersypen, L. M. K. Spins in few-electron quantum dots. *Rev. Mod. Phys.* **79**, 1217–1265 (2007).

42. Takahashi, S., Hanson, R., van Tol, J., Sherwin, M. S. & Awschalom, D. D. Quenching spin decoherence in diamond through spin bath polarization. *Phys. Rev. Lett.* **101**, 047601 (2008).

43. Pohl, R. O., Liu, X., Thompson, E. Low-temperature thermal conductivity and acoustic attenuation in amorphous solids. *Rev. Mod. Phys.* **74**, 991–1013 (2002).

44. Cole, G. D., Wilson-Rae, I., Werbach, K., Vanner, M. R. & Aspelmeyer, M. Phonon-tunnelling dissipation in mechanical resonators. *Nat Commun* **2**, 231 (2011).

4.3 Coherence time manipulation via cavity backaction

As demonstrated in the previous chapter, there is no measurable phase decoherence in the system presented here, the observed phase relaxation is solely caused by the energy relaxation of the system. In return, this means that an increase of the energy relaxation time should directly correspond to an increase in the phase relaxation time. However, the intrinsic quality factor of the beam can not be changed so easily, in the experiments described in this chapter it is most likely limited by the dielectric damping effect. The high electric fields are necessary to tune the system to the avoided crossing, thus this energy loss mechanism can only be reduced by using a different resonator material (or maybe even lower temperatures, see chapter 5.1).

Another way to influence the mechanical quality factor was already presented in chapter 3.1. By detuning the microwave pump frequency $f_{\mu\mathrm{w}}$ with respect to the resonance frequency f_c of the microstrip resonator, backaction forces act on the mechanical resonator [Mar07, Teu08]. In the blue-detuned regime, where the detuning $\Delta = f_{\mu\mathrm{w}} - f_c$ is positive, these forces are in phase with the oscillation of the beam and thus create aditional phonons in the resonator mode. This corresponds to an effective increase of the quality factor, see also Fig. 3 in chapter 3.1. The opposite efffect takes place for $\Delta < 0$. A detailed analysis of the detuning-dependent quality factor $Q(\Delta)$ can be found in chapter 3.1.1. This way of altering the quality factor can be easily implemented using the existing sample and setup, as only the microwave generator frequency needs to be detuned from the resonant pumping used in the previous measurements.

To quantify the effect, the T_1 times and Ramsey fringes are measured at different microwave pump frequencies. A Hahn echo experiment was performed only at selected points, as it requires an exact (and time-consuming) calibration of the pulse frequency to avoid slow oscillations in the echo signal. Upon a change in the microwave frequency, the power in the cavity and the electrical environment of the beam are altered, creating slight variations of the coupling strength. Thus, this calibration is necessary for every data point where a Hahn echo measurement is performed, while the exact detuning is not critical for a Ramsey experiment and thus allows for a much faster measurement.

The results of the measurements for microwave detunings Δ ranging from +3.5 to -12 MHz are shown in Fig. 4.1. The possible detunings are limited to this interval: At more positive values, cavity-induced self-oscillation (see chapter 3.1) of the lower mode sets in very close to the point of minimum frequency separation, making it impossible to capture the whole avoided crossing and extract the necessary tuning voltages (as described in chapter 4.2.1). For large negative detunings, the power circulating in the microwave cavity significantly decreases, and thus the sideband amplitude is too small for a reliable measurement. This also explains the rather large errror bars of the leftmost datapoints in Fig. 4.1b.

Looking at Fig. 4.1a, one can clearly see how the cavity backaction has a strong influence on the energy relaxation time of the lower state, while the properties of the upper state are changed only very slightly. This can be attributed to a much weaker coupling of

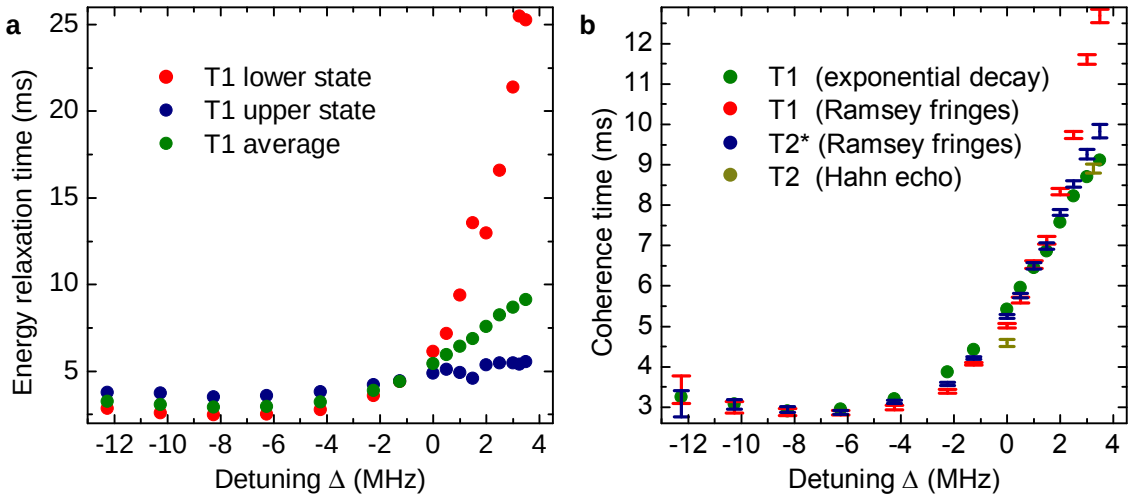

Figure 4.1: Coherence times versus microwave detuning: The measurement of the lower and upper state energy relaxation time shown in **a** demonstrates how the upper state has a much higher coupling to the microwave cavity, while the lower state is only slightly affected by the detuned microwave pump tone. Panel **b** depicts the average T_1 time (same as in **a**), T_1 and T_2^* times extracted from the Ramsey fringes and two measurements of the T_2 time extracted from Hahn echo experiments. Datapoints with no error bars have an error smaller than the plot marker size.

this mode to the electric field gradients. As the side electrodes are positioned asymetrically with respect to the beam, one of the two diagonal hybrid modes (see chapter 4.1.1) has a much weaker coupling constant g than the other one. This is also visible in the detection sensitivity: The traces in Fig. 3 of chapter 4.2 are normalized, but the measured power in the upper state (at almost identical mechanical amplitudes) is a factor of five smaller. The rate average of the two energy relaxation times thus increases only by about a factor of two for the maximal positive detuning.

In return, this should also lead to a doubling of the phase coherence time, if it is still solely dominated by energy relaxation. This behaviour can be seen in Fig. 4.1b. The T_2^* times follow the average T_1 time extracted from the exponential decay (green points in Fig. 4.1a&b), the Hahn measurements lead to a similar result. But the T_1 times obtained from the same Ramsey fringe measurements significantly exceed the calculated average times. The most likely explanation is the effect already described in the first part of chapter 4.2.1: Between the two $\pi/2$ pulses of the Ramsey experiment, the system is in a superposition state between the lower and upper state. As the lower state has a much larger lifetime than the upper one, the Bloch vector starts to slowly tilt downwards towards the lower state. As the state is no more in the equator plane of the Bloch sphere, the second $\pi/2$ pulse can never rotate it to the upper or lower state. The Ramsey fringes thus do not reach zero anymore (see Fig. 4.2a), which in turn looks like a larger T_1 time. But the "real" T_1 time is the energy relaxation time of a state on the equator plane of the Bloch sphere, which can also be seen from the T_2 and T_2^* measurements, which are in good agreement with the average T_1 time calculated for the equator plane.

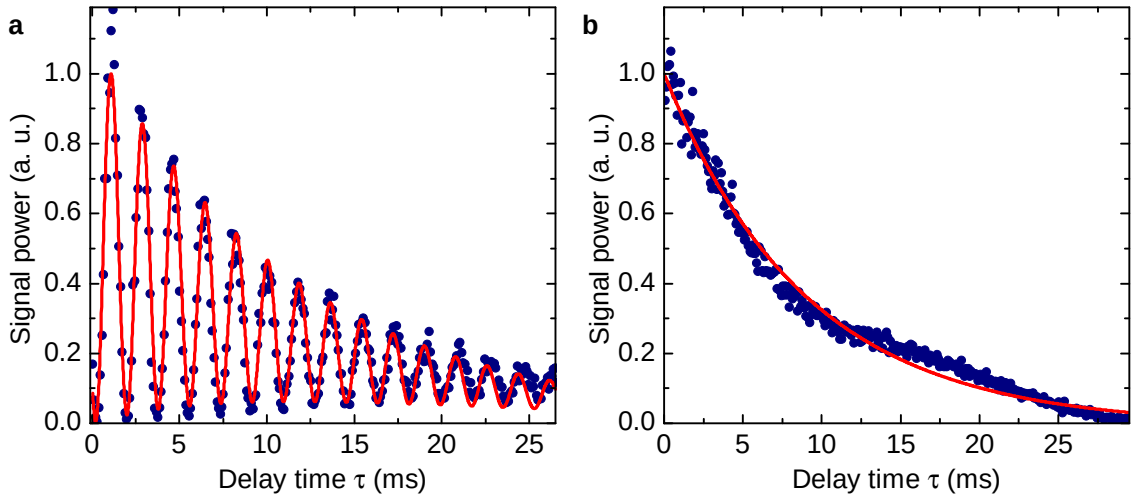

Figure 4.2: Time-resolved experiments at positive microwave detuning: Ramsey fringes (**a**) and Hahn echo (**b**) at a positive microwave detuning $\Delta = 3.25\,\mathrm{MHz}$.

The Hahn echo at a positive detuning of 3.25 MHz exhibits a strange effect. As can be seen in Fig. 4.2b, the time evolution of the measured power in the upper state after the pulse sequence does not follow a pure exponential decay anymore. Instead, there is a non-exponential plateau-like region between delay times of approximately 10 and 15 ms. The experiment was repeated multiple times to rule out errors in the pulse calibration. Furthermore, the appearance of this plateau is independent of the measurement direction as the results are the same if the measurement is started with a long delay time which is then gradually shortened. The origin of the observed behaviour is not yet understood.

4.4 Stückelberg oscillations

Stückelberg oscillations are another coherent experiment which can be performed using a system that exhibits an avoided crossing [Oli05, Hei10, Ste12]. They are based on the Landau-Zener transition: A passage through the avoided crossing distributes the energy of the system (which was initialized in one branch) among the two branches, in a ratio depending on the tuning speed (as discussed in chapter 4.1). If the system is now tuned to a certain point beyond the avoided crossing, and then the tuning direction is reversed, the two branches once more interact with each other and exchange energy as they pass through the avoided crossing. At this second interaction, the relative phase of the two branches, which depends on the tuning speed and the distance of the reversal point to the point of maximum coupling, determines the final energy distribution. A multiple passage of the coupling region is also possible, but here only the double passage will be examined.

The concept of the experiment is sketched in Fig. 4.3a: It starts with an initilization in the lower (blue) branch at a voltage of U_i. As the system is tuned through the avoided crossing, some of its energy is transferred to the upper (red) branch, the exact amount depends on the tuning speed. Upon reaching the voltage U_r, the tuning direction is reversed, the avoided crossing is passed once more and the experiment stops at the voltage U_f, where the energy in the lower (blue) branch is measured. U_f is chosen slightly larger than U_i such that the system is not tuned to the frequency of the constant actuation signal and thereby driven once more.

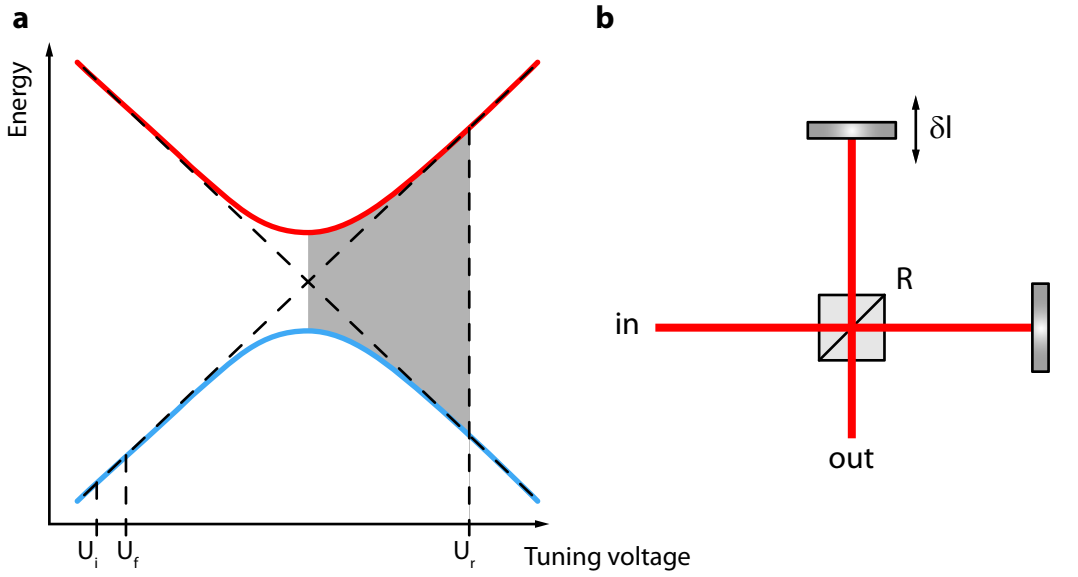

Figure 4.3: Sketch of the Stückelberg experiment: Panel **a** depicts a schematic avoided crossing and the initial voltage $\mathrm{U_i}$, final voltage $\mathrm{U_f}$ and reversal voltage $\mathrm{U_r}$. The gray area illustrates the frequency difference between the two branches. A sketched Michelson interferometer is shown in **b**, which is an optical analogon. Its two parameters are the path length difference δl and the reflectivity R of the mirror.

The phase difference between the two branches is the integral of their instantaneous frequency difference (shown in gray in Fig. 4.3a) over time in the region between the point of maximal coupling and U_r. This integral can be influenced via two parameters. Either the tuning speed is increased, and thus the gray region is passed more quickly, or the reversal voltage U_r can be decreased and the gray area becomes smaller.

The characteristics of this experiment are analogous to an optical Michelson interferometer, which is sketched in Fig. 4.3b. The magnitude of U_r corresponds to the path length difference δl, while the tuning speed influences the Landau-Zener transition probability, which corresponds to the reflectivity R of the beamsplitter mirror. It is thus easy to see that no interference effect can be expected for very fast or very slow tuning speeds, as this corresponds to a mirror reflectivity of 0 or 100 % (or all of the system's energy remains in the lower branch or is transferred to the upper branch, respectively).

A very thorough theoretical treatment of Stückelberg interferometry can be found in [She10]. There, the probability to return to the same branch as one started in before the double passage is given as

$$P = 1 - 4P_\mathrm{LZ}(1 - P_\mathrm{LZ}) \sin^2\left(\xi + \varphi_\mathrm{s} - \frac{\pi}{2}\right). \tag{4.1}$$

P_LZ is the Landau-Zener transition probability (introduced as $P_\mathrm{dia} = e^{\frac{-\pi\Omega^2}{2\alpha}}$ in chapter 4.1), ξ denotes the accumulated phase difference and φ_s is the so-called Stückelberg phase, caused by the passage through the coupling region itself. In the optical analogy of Fig. 4.3b, this would (loosely) correspond to the $180°$ phase jump induced by the reflection on the beam splitter. It is given as

$$\varphi_\mathrm{s} = \frac{\pi}{4} + \delta(\ln\delta - 1) + \arg\Gamma(1 - i\delta), \tag{4.2}$$

where $\delta = \frac{\Omega^2}{4\alpha}$ and Γ is the Gamma function.

Equation 4.1 has two free parameters, the tuning speed δ and the phase pickup ξ, which is inversely proportional to δ (as faster tuning leads to less accumulated phase difference). The other parameters like φ_s and $P_\mathrm{LZ} = e^{-2\pi\delta}$ all solely depend on δ. For a certain reversal voltage, this makes P a function of δ (which is known from the experimental parameters) and a "phase pickup constant" $\beta = \delta \cdot \xi$, which depends on the shape of the avoided crossing and the reversal voltage.

To measure these oscillations, the identical mechanical resonator and measurement setup as in chapter 4.2 and 4.3 are used. The system's avoided crossing is shown in Fig. 4.4a: After an initialization at 0 V, the voltage is ramped up to three different reversal points, shown as black lines. The downward ramps ends at 0.2 V, where a fit to the measured exponential decay allows to extract the oscillation energy after the triangular pulse (similar to chapter 4.1). This experiment is performed with different voltage sweep rates, and plotted in Fig. 4.4 versus the inverse of this sweep rate. To calculate the expected behaviour, the voltage sweep rate can be transformed into the tuning speed α with a conversion factor of 55 kHz/V, estimated from the avoided crossing. The two branches

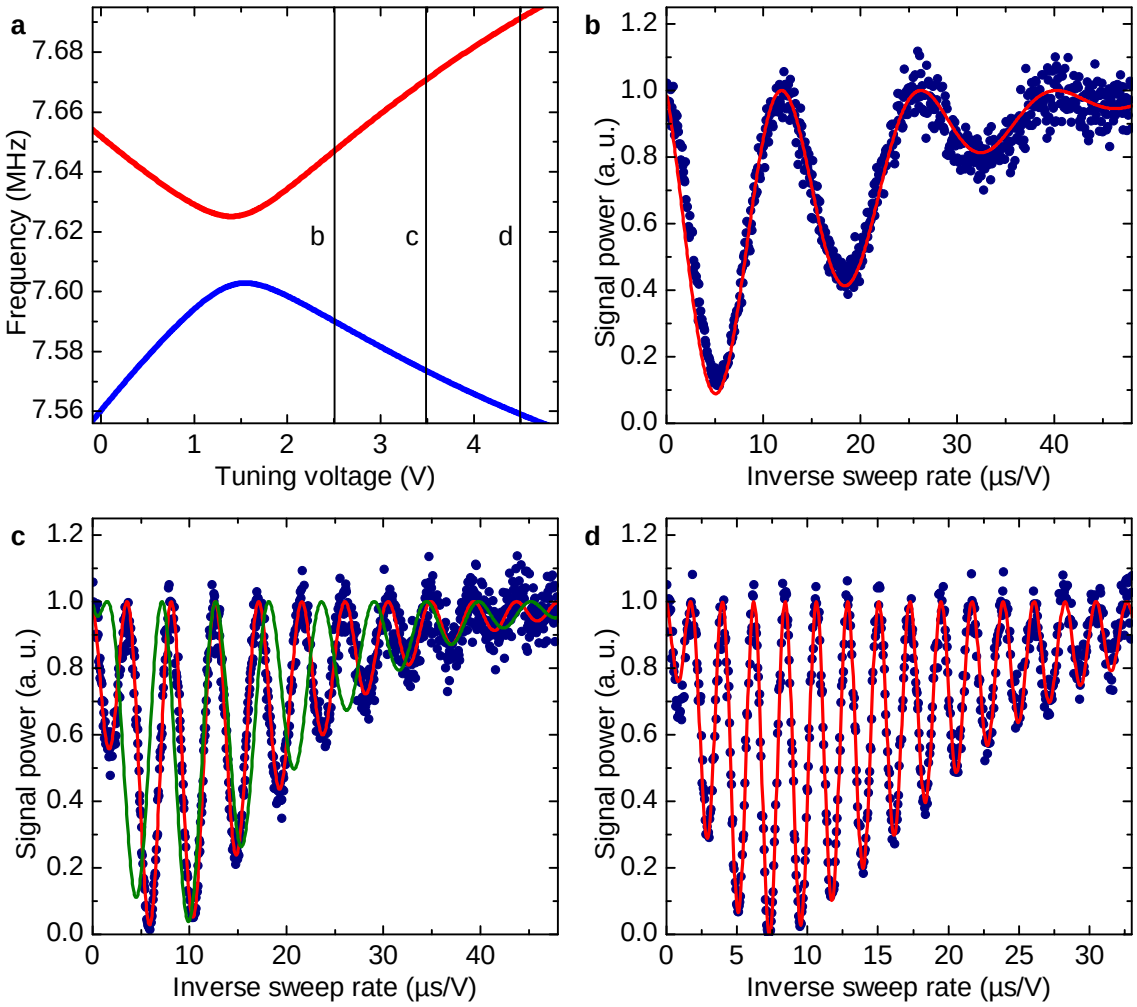

Figure 4.4: Measured Stückelberg oscillations for different reversal voltages: The measured avoided crossing as well as the three different reversal voltages are shown in **a**. Panels **b-d** depict the measured oscillation patterns for reversal voltages of 2.5, 3.5 and 4.5 V and the corresponding fit. The green line in **c** is a fit with the unmodified equation 4.1, while the red lines use a function without the constant phase factor of $\pi/2$.

actually have a parabolic shape, so the frequency tuning speed is not constant, and only an average value can be given. Together with the coupling strength $\Omega = 22.614\,\text{kHz}$, δ can be calculated. Apart from an overall scaling factor, this leaves β as the only fit parameter. In principle, β could also be calculated from the avoided crossing diagram and the tuning speed, but the complex parabolic shape of the two branches makes this rather difficult. The red lines in Fig. 4.4 demonstrate the excellent agreement between theory and experiment using three different fitted values for β. To obtain these curves, the factor of $\pi/2$ in equation 4.1 has to be omitted. A fit using the unmodified equation is shown in Fig. 4.4c as a green line, clearly not reproducing the measured data points. The source of this deviation is unclear and currently under investigation [Rib12].

Chapter 5

Dissipation in silicon nitride - Part 2

In chapter 2, the interaction with two-level system defects in the resonator material is identified as the most likely microscopic damping mechanism in silicon nitride resonators. As the measured data points are only taken at temperatures around 4 K and at 300 K, the typcial absorption peak related to such two-level systems [Arc09] expected somewhere around 50 K could not be investigated in this first experiment.

In the first part of this chapter, a measurement using the microwave detection inside the VERICOLD cryostat at multiple temperatures reveals the expected temperature dependence of the mechanical damping, exhibiting a broad peak at approximately 50 K.

The second part of the chapter presents a different approach to combine a microwave cavity with a silicon nitride nanomechanical resonator. To achieve a much better performance in the low-temperature regime, the cavity is fabricated using the superconductor niobium and is situated on the same silicon chip as the mechanical resonators. At temperatures below the critical temperature, the coplanar waveguide resonators can achieve quality factors far beyond 10,000, enabling very sensitive measurements and strong backaction effects at negligible dissipated power. But the integration of superconducting waveguides and mechanical resonators on the same chip presents quite a few challenges, thus only first steps towards a sucessful fabrication can be presented.

5.1 Temperature-dependent dielectrical and mechanical losses

Glasses (like silica or silicon nitride) do not have a long-range order, making it very likely that the solid can undergo small changes in its microscopic configuration [Jäc72, Poh02, Tie92]. These, for simplicity bistable, systems can be modeled by a particle moving in a double-well potential (see Fig. 5.1) with a barrier height V and an asymmetry of the wells Δ (in the following used in temperature units, i. e. as the respective energy divided by k_B). Their interaction with the strain field e of a sound wave $\gamma = \partial\Delta/2\partial e$ modulates the energy difference Δ between the two levels. Depending on the temperature, several interaction regimes between acoustic excitations and those two-level systems (TLS) are possible [Jäc72, Tie92, Vac05, Riv11]: At very low temperatures in the mK range, where no thermal excitation takes place, the predominant mechanism is resonant absorption and a saturation behaviour can be observed. Around a few K, tunneling-assisted relaxation of the only partially occupied TLS takes place, while thermally activated relaxation dominates above approximately 10 K, where all TLS are thermally activated. The following analysis will only treat the latter case, as the lower temperature regimes are not acessible in the current experimental setup. At elevated temperatures, the thermally excited levels will not necessarily be limited to only the two lowest states, but for simplicity the systems will still be called TLS.

5.1.1 Theoretical model

The following section and its notation follows references [Vac05, Ane10a]. All articles concerning dissipation due to TLS do not calculate the mechanical damping $\Gamma = \omega/Q$ but rather the inverse quality factor Q^{-1}. The same notation will be used here, but it should be noted that (as already mentioned in chapter 2.1) such values must not be compared between stressed and unstressed systems, as otherwise an unexpected deviation will result [Sou09] (since the stress increases Q but has no significant influence on Γ). As we only consider stressed systems, the following section will also use Q^{-1} and call it the dissipation to conform to the existing literature.

In its most general form, the relaxation dissipation can be written as

$$Q_\mathrm{rel}^{-1} = \frac{\gamma^2}{\rho v^2 T} \int_{-\infty}^{\infty} d\Delta \int_{0}^{\infty} dV P(\Delta, V) \operatorname{sech}^2\left(\frac{\Delta}{2T}\right) \frac{\omega\tau}{1+\omega^2\tau^2} \,, \tag{5.1}$$

where ρ and v denote the density and sound velocity of the material and ω the angular frequency of the mechanical oscillation.

$$\tau = \tau_0 e^{\frac{V}{T}} \operatorname{sech}\left(\frac{\Delta}{2T}\right) \tag{5.2}$$

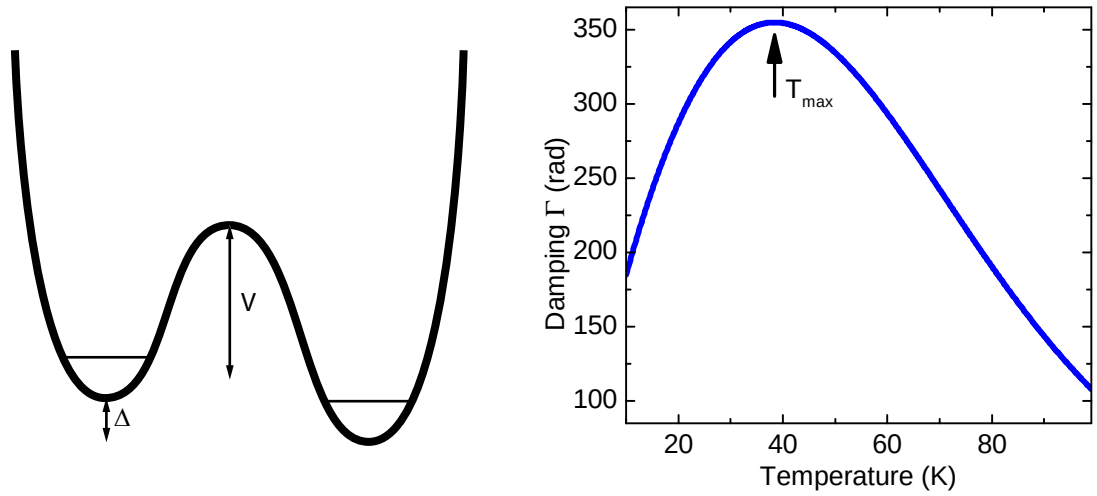

Figure 5.1: Two-level systems: Sketch of a double-well potential with asymmetry Δ and barrier height V and calculated mechanical damping for a 8 MHz resonator using the parameters for silica found in [Vac05].

is the relaxation time for hopping within the double well, using the inverse attempt frequency τ_0.

$P(\Delta, V)d\Delta dV$ is the volume density of TLS with their parameters in the ranges $d\Delta$ and dV. It is a reasonable assumption [Vac05] to approximate it as

$$P(\Delta, V) \propto \frac{1}{V_0}\left(\frac{V}{V_0}\right)^{-\zeta} \exp\left(-\frac{V^2}{2V_0^2}\right) \exp\left(-\frac{\Delta^2}{2\Delta_C^2}\right) \tag{5.3}$$

using the cutoff parameters V_0 and Δ_C and an exponent $\zeta < 1$. By inserting equation 5.2 and equation 5.3, merging all constants into $\mathcal{C}$ and approximating $\mathrm{sech}(x) \cong 1$ for $|x| \leq 1$ and 0 otherwise, one can rewrite equation 5.1 as

$$Q_{\mathrm{rel}}^{-1} = \mathcal{C}\,\Phi\left(\frac{\sqrt{2}\,T}{\Delta_C}\right)\frac{1}{T}\int_0^\infty \left(\frac{V}{V_0}\right)^{-\zeta} \exp\left(-\frac{1}{2}\frac{V^2}{V_0^2}\right)\ \frac{\omega\tau_0 \exp(V/T)}{1+\omega^2\tau_0^2 \exp(2V/T)} dV\,, \tag{5.4}$$

where $\Phi(x)$ is the error function.

This function depends on the temperature T as well as the mechanical oscillation frequency ω. The typical dissipation peak at temperatures around 50 K is shown in Fig. 5.1, calculated using the parameters of silica from [Vac05] for a mechanical frequency of 8 MHz. This peak around $T_{\max}$ is a result of the last term in equation 5.4. As can be seen more clearly in equation 5.1, this term is maximized if $\omega\tau = 1$. This means that the jumps between the two wells occur at a frequency equal to the oscillation frequency of the mechanical strain field, making the energy absorption process as effective as possible.

At higher temperatures, defects with higher, but well-defined energy barrier can lead to additional peaks in the absorption [Lud00]. The thermally activated jump rate between their two states is given by an Arrhenius law $\tau = \tau_a \cdot \exp(V_a/T)$. In a rather simple

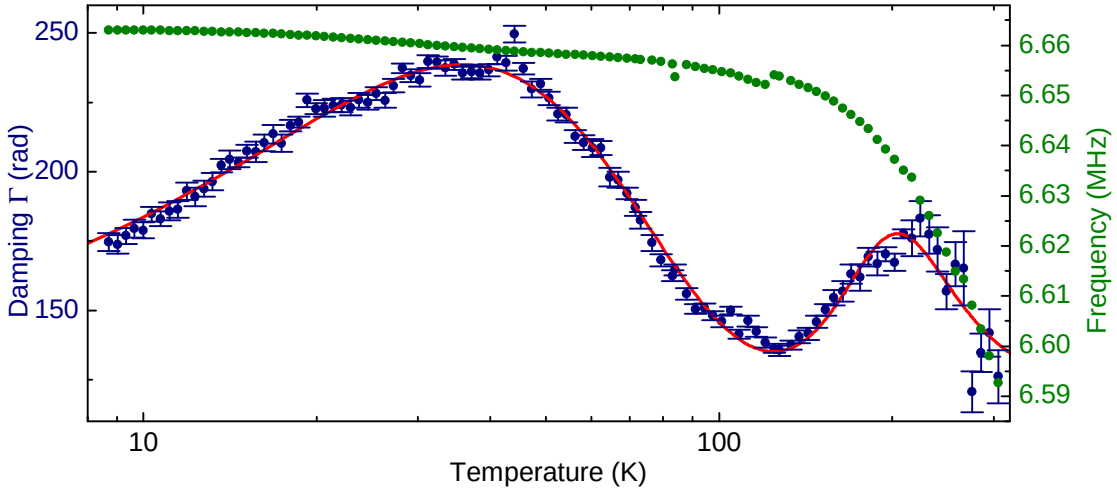

Figure 5.2: Temperature-dependent damping: Measured damping constants Γ (blue dots) versus temperature. The red line is a fit of the damping model described in the text. The influence of the two-level systems can also be seen in the resonance frequency (green points), which exhibits a slight dip around 40 K.

model, it is sufficient [Lud13] to assume a single barrier height V_a, thus removing any V-dependent terms and collapsing the integral in equation 5.4, and to neglect a possible asymmetry. This leads to a damping term due to an Arrhenius peak

$$Q_{\mathrm{a}}^{-1} = \frac{\mathcal{C}_{\mathrm{a}}}{T} \frac{\omega\tau_{\mathrm{a}} \exp(V_{\mathrm{a}}/T)}{1+\omega^2\tau_{\mathrm{a}}^2 \exp(2V_{\mathrm{a}}/T)} \tag{5.5}$$

5.1.2 Measurement and discussion

This chapter presents the measurement of the mechanical damping constant $\Gamma(T) = \frac{\omega(T)}{Q(T)}$ at different temperatures T between 8 and 330 K. The quality factors are measured at a dc voltage of 0 V to exclude any influence of the dielectric damping. At every temperature, the transmitted microwave signal is first switched to a power detector (see appendix A) and the spectrum of the microwave cavity is measured in a span of 10 MHz by sweeping the microwave generator frequency. This needs to be done using low microwave powers (0 dBm at the generator) as otherwise the detunig-dependent heating would change the temperature. A Lorentzian fit[1] is used to extract the (temperature-dependent) cavity resonance frequency and the microwave generator is set to this frequency to avoid any optomechanical cooling or heating effects while aquiring mechanical spectra. Furthermore, the measurement is conducted at a reduced microwave power of -2 dBm such that an accidental, very small microwave detuning has only negligible influence on the mechanical quality factor.

[1] A background in the form of $a + f \cdot b$ has to be used to account for the broad cable resonances superimposed with the microwave cavity reflection signal.

The measured frequencies and damping constants are shown in Fig. 5.2. The dissipation curve exhibits not only one, but two maxima at temperatures of approximately 40 K and 210 K. The lower peak can be attributed to the configurational changes common in glassy systems, its parameters are rather similar to the values found in silica [Tie92, Vac05]. The rather narrow second peak is most likely caused by a certain type of defect in the silicon nitride film with a narrow distribution of barrier heights. Likely candidates include dangling Si or N bonds [Lau89] or defects connected to the roughly 1 % of hydrogen atoms incorporated into the material during chemical vapour deposition [Cho82]. Both peaks can be fitted simultaneously with the function $\Gamma_0 + \omega(T)[Q_{\mathrm{rel}}^{-1}(T) + Q_{\mathrm{a}}^{-1}(T)]$ (shown as a red line in Fig. 5.2) using an additional, temperature-independent damping offset Γ_0.

The extracted parameters of the lower-temperature peak are $\mathcal{C} = 5.0 \pm 0.3 \cdot 10^{-6}$, $V_0 = 455 \pm 10\,\mathrm{K}$, $\Delta_C = 112 \pm 5\,\mathrm{K}$ and $\tau_0 = 9.8 \pm 2.4 \cdot 10^{-13}\,\mathrm{s}$. The Arrhenius peak is caused by defects with a barrier height $V_{\mathrm{a}} = 960 \pm 44\,\mathrm{K}$, an inverse attempt frequency $\tau_{\mathrm{a}} = 2.8 \pm 0.6 \cdot 10^{-10}\,\mathrm{s}$ and a scaling constant $\mathcal{C}_{\mathrm{a}} = 6.0 \pm 0.3 \cdot 10^{-4}$. There is a temperature-independent damping contribution $\Gamma_0 = 118 \pm 2\,\mathrm{rad}$ which can not be explained by this defect-damping model. Measurements at even lower temperatures, where all the thermally activated processes described here are vanishing, might allow a more thorough understanding of all damping effects.

5.2 Low-temperature measurements using niobium microwave resonators

The limiting factor in reaching even lower temperatures than presented in the last chapter and obtaining higher detection sensitivities is the quality factor of the copper microwave resonator. Higher quality factors will lead to lower losses in the microwave cavity and will thus reduce the heating of the cryostat, making it possible to operate in a dilution refrigerator at temperatures below 100 mK. Furthermore, the higher power circulating in the cavity will lead to larger sideband signals, increasing the detection sensitivity.

As discussed in chapter 3, it is difficult to further increase the quality factor of a cavity made from a normal conductor without loosing the ability to just connect the chip carrying the mechanical resonators with a bond wire, because most high-Q cavities are hollow 3D volume resonators. Thus, higher quality factors at low temperatures can best be achieved using planar superconducting cavities. In a cooperation with F. Hocke, M. Pernpeintner and H. Hübl from the Walther-Meissner-Institut in Garching, we choose to fabricate coplanar waveguide resonators made from niobium on the same chip as the mechanical resonators, as the losses in a bond wire would already degrade the quality factor. They can be used at temperatures below $\sim$9 K, the critical temperature of niobium, and their properties are well-known from numerous low-temperature experiments [Wal04, Ham07, Hof09, You11].

5.2.1 Layout & Fabrication

The layout of the niobium resonators is shown in Fig. 5.3: A chip with dimensions of $10 \cdot 6\,\mathrm{mm}^2$ carries four meandering coplanar $\lambda/2$ resonators with lengths ranging from 9.4 to 10.6 mm. Two feed lines are capacitively coupled to the ends of the resonators, allowing to measure the resonator transmission. The feed lines are designed as a $50\,\Omega$ system, just like the SMA connectors whose center pins are silver-glued to the two large areas on the left and right. In contrast to that, the resonators themselves use a different geometry and have an impedance of $70\,\Omega$. This helps to increase the coupling of the resonator's electric field to the two silicon nitride beams situated in the gap between the center conductor (see the left inset in Fig. 5.3) and ground plane at the lower end of the four resonators, as the electric field in a higher impedance system is increased.

The fabrication of such structures presents quite a few challenges: As the gaps in the niobium layer housing the silicon nitride beams should have a width of 500 nm and below, they can no longer be patterned using optical lithography usually used to fabricate coplanar waveguide resonators. On the other hand, there are a lot of very large features, which normally take a long time to write using electron beam lithography. This problem can be solved by using two different apertures and taking advantage of the "fixed beam moving stage" mode of an *eLine* electron beam lithography system manufactured by *Raith*. Here, the sample is moved by an interferometer-controlled stage while the electron beam is only

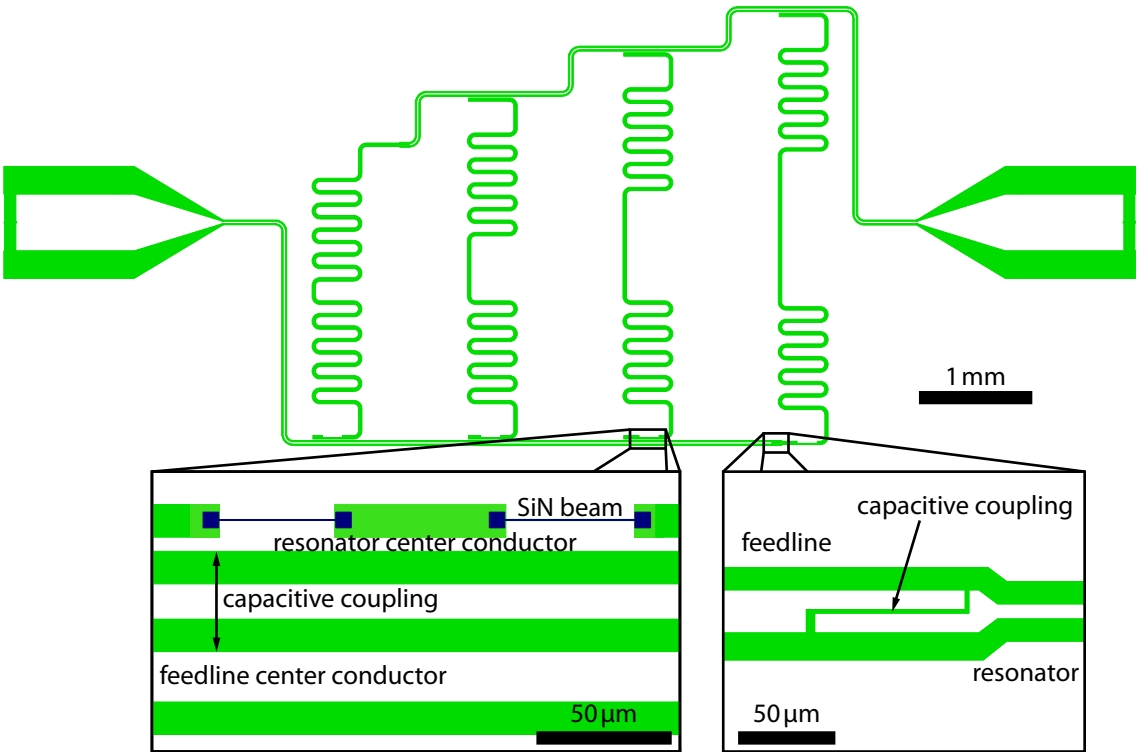

Figure 5.3: Layout of the coplanar niobium waveguide resonators: The four resonators are situated in the middle of the chip, while the two feedlines interfacing them to microwave connectors are coupled to the bottom and top ends. White parts will be covered in niobium, while green parts are etched away. The two magnified sections show the integration of two silicon nitride beams (blue) into the gap of the coplanar waveguide and the coupling between the lower feedline and the rightmost resonator.

modulated to create the width of the line. This mode is used to write the long, smooth curves necessary for the coplanar waveguide resonators. Using the large 120 µm aperture and thus a 30-fold increased electron beam current (compared to the 30 µm aperture used for high-resolution lithography), the large waveguide structures can be patterned in about half an hour.

The usual processing steps for the mechanical resonator (see appendix B) have to be modified as discussed below to integrate niobium structures onto the chip. As niobium is usually sputtered and a thick layer of 100-200 nm is required to benefit from the negligible ohmic losses, the niobium layer can not be structured using a liftoff process. Instead, the niobium layer is deposited onto the whole chip. A masking layer is structured on top of the niobium (the green parts in Fig. 5.3 are not covered by the mask) and a reactive ion etching step is used to remove the exposed niobium.

A schematic of all the process steps is shown in Fig. 5.4: At first, the SiN beam is defined using an aluminum or aluminum/cobalt mask (step **1**) and a reactive ion etch process (as in appendix B) removes the rest of the silicon nitride layer and 200 nm of the underlying silicon oxide (step **2**). This is chosen such that the top of the 200 nm thick

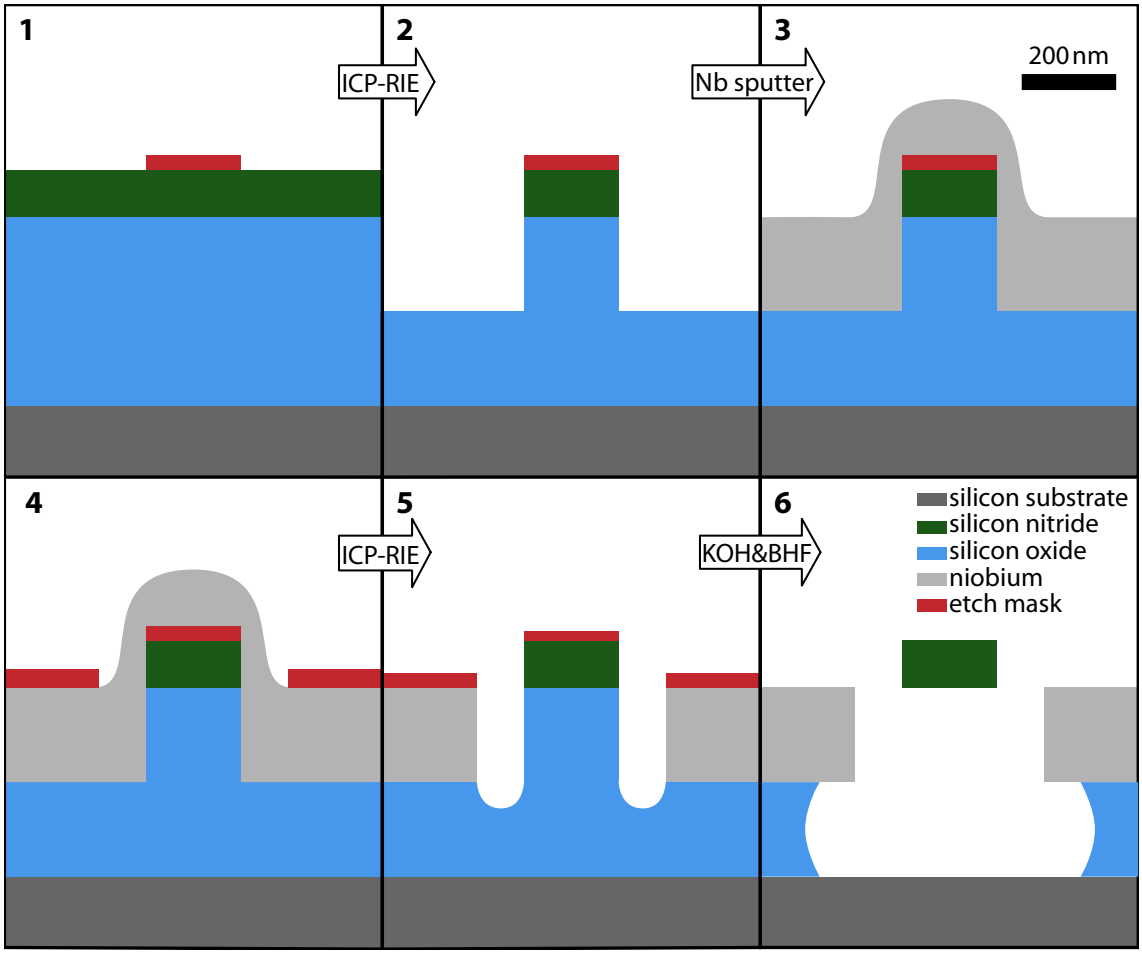

Figure 5.4: The major processing steps required to fabricate a silicon nitride beam embedded into a niobium waveguide cavity. See the text for details of the single processes.

sputtered niobium layer (step **3**) is flushed with the bottom of the beam, as this leads to a maximized capacitance change with beam deflection (cf. chapter 3.2). In step **4**, another masking layer is patterned on top of the niobium. It protects the coplanar waveguides and the ground plane during the following reactive ion etch, while the silicon nitride beam is still protected by the same metal layer as in step **2**. Finally, the etch masks are removed using KOH and the beam is underetched with a buffered hydrofluoric acid solution.

Several of these steps need some optimization to produce satisfactory devices. It would be ideal to use a resist as the mask in steps **4**&**5**, as this provides the highest resolution and minimum number of processing steps. Tests with several positive resists (PMMA 500k, AR-P 617 by *allresist* and ZEP520 by *ZEONREX*) were unsuccessful, as they can not withstand the agressive ion etch process required to remove the niobium. So instead a negative resist (MA-N 2403 by *micro resist* or AR-N 7500 by *allresist*) is used to create a liftoff mask for a 25 nm thick aluminum layer. As this liftoff usually

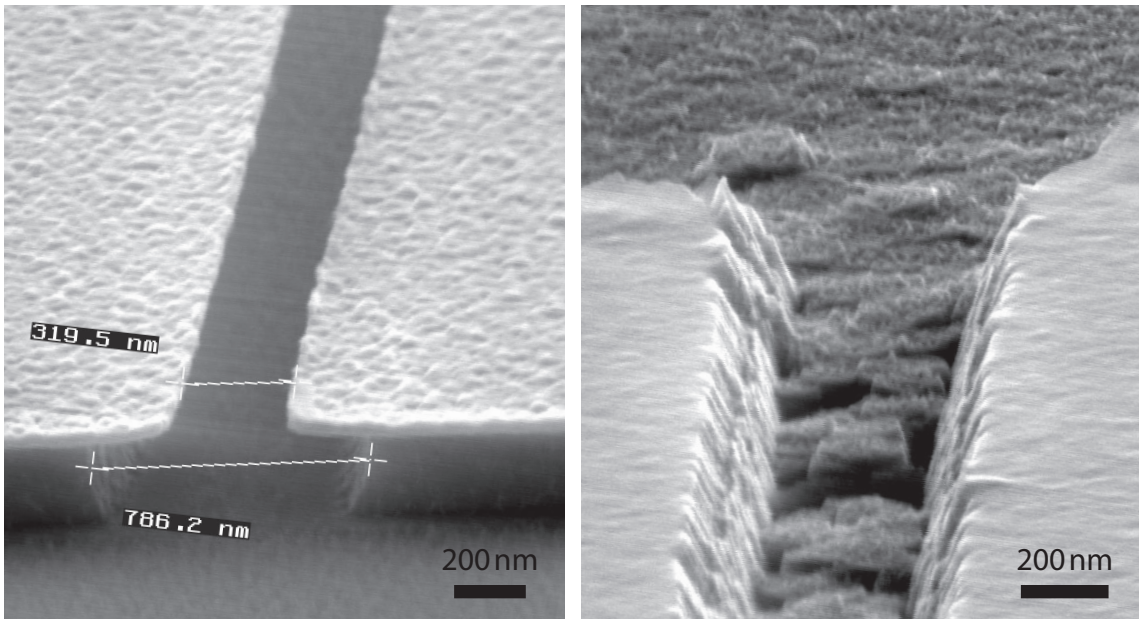

Figure 5.5: Etch results after a SF_6/Ar dry etch of 200 nm niobium: On the left, the aluminum mask is clearly underetched after a low-bias etch recipe. The right panel (mask already removed) shows an outwards angling of the lateral edges after an etch with a high bias voltage.

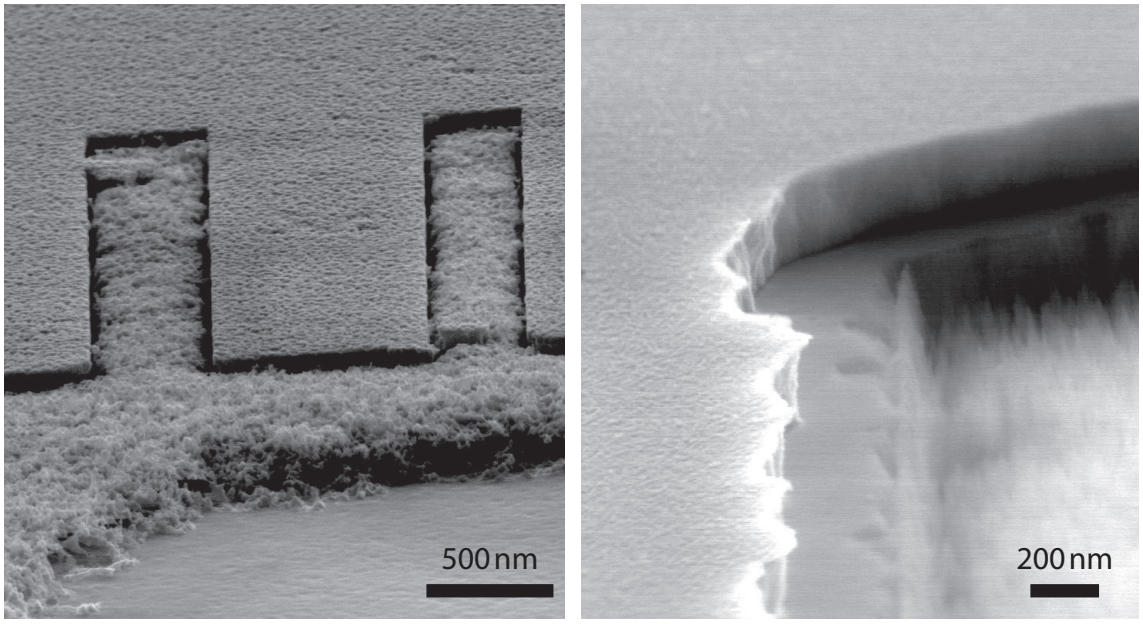

Figure 5.6: Wet etch problems: The left panel shows residues of the aluminum mask after a buffered fluoric acid etch. Right panel: Chemical etching of the niobium side wall in KOH creates a step in the etch profile.

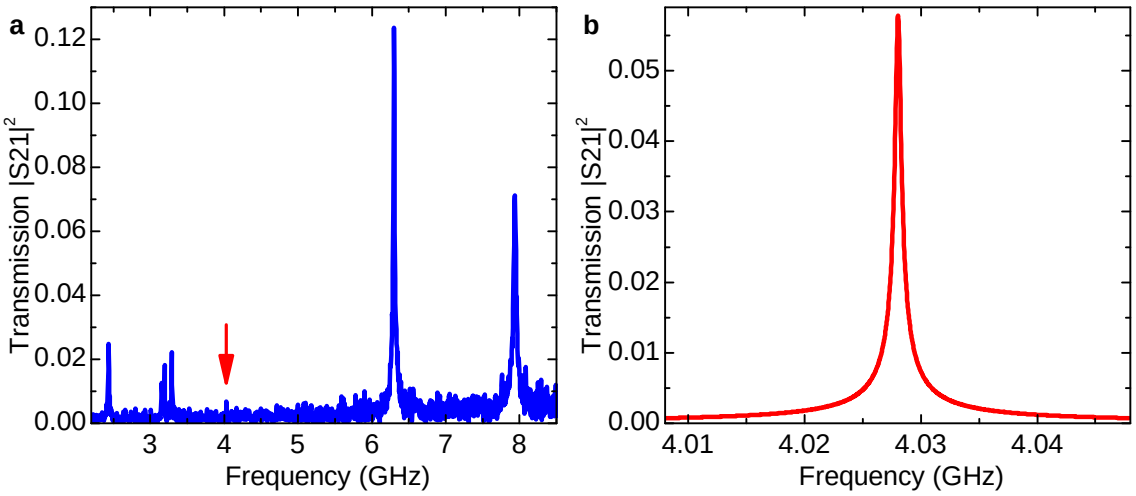

Figure 5.7: Electrical resonances at 1.5 K: Panel **a** shows a wide spectrum with several resonances, some resulting from the sample box. The red arrow marks the position of the cavity resonance with the highest quality factor (∼8000), shown in more detail in **b**.

requires sonification for a successful pattern transfer, the edges of the niobium structures are rougher compared to a resist mask.

Furthermore, the recipe for the second dry etch step is rather critical, as the etched walls should be vertical and not angled, and the mask should not be underetched. Two negative examples are shown in Fig. 5.5. It turns out that a dry etch process with a high dc bias is required to avoid any underetching (the left panel of Fig. 5.5 was etched with a bias of ∼30 V), while the ratio of Ar to SF_6 slightly influenced the wall angle in a high-bias (∼300 V) process.

In principle, the hydrofluoric acid should also remove the aluminum layer used as an etch mask and thus serve as a cleaning as well as underetching step. But, as can be seen in the left part of Fig. 5.6, some strange residue is created if the aluminum is not removed prior to the buffered oxide etch step. When removing the etch mask with KOH, another problem arises. The lateral edges of the niobium layers are attacked by the base, broadening every etched trench. It seems like they are still covered with some thin protective layer after the dry-etch step and thus do not oxidize in the air. By treating the chips in a oxygen plasma for three minutes, a sufficient passivation layer can be created that withstands the alkaline etch step.

5.2.2 Electrical test

One of the earlier chips, still suffering from the unwanted niobium etching in KOH and without any operational mechanical resonators, is used to test the electrical resonators. The chip is mounted inside the sample holder, while conductive silver glue is used to connect the ground plane and the two feed lines to the body of the sample holder and two

SMA connectors. A lid is screwed on to reduce radiation losses of the electrical cavities. The whole assembly is then cooled down to 1.5 K, and the transmission spectrum is recorded with a network analyzer. The results are shown in Fig. 5.7: One can see multiple resonances between 2.5 and 8 GHz, which result from the coplanar waveguide resonators as well as intrinsic resonances of the sample box (exhibiting rather large linewidths). The cavity resonance with the highest quality factor has a frequency of $\sim$4.03 GHz and is shown in more detail in the right panel, the fitted quality factor is slightly above 8000. This demonstrates the high potential of such superconducting resonators, as a 50-fold increase in quality factor (compared to copper resonators) can be achieved even with a chip still suffering from several fabrication problems.

Chapter 6

Conclusion and Outlook

The work presented in this thesis makes advances in three different directions. The material properties and their influence on the mechanical quality factor of silicon nitride NEMS were the initial starting point of this thesis. Chapter 2 analyzes the quality factors of prestressed silicon nitride strings and provides a theoretical model explaining their unusually high Q's compared to unstressed resonators. The stress simply increases the restoring force and thus the energy stored in the mechanical mode at a certain amplitude, while the energy loss per oscillation cycle is nearly constant. The quotient of these two quantities is the quality factor, which as a result rises with stress.

The model also assumes the energy loss to be proportional to the local bending of the beam, which corresponds to a non-elastic contribution to the Young's modulus. As silicon nitride is an amorphous, glassy material, the most likely candidate for this contribution are localized two-level defects. The characteristic temperature dependence of this loss mechanism is presented in chapter 5.1.

These low-temperature measurements were enabled by the development of a new technology to measure and control the oscillatory motion of nanomechanical resonators made from dielectric materials, presented in chapter 3. The design of a high-Q room temperature microwave cavity enables the multiplexed electrical readout of many beams with a sensitivity comparable to optical techniques. Furthermore, the coupling is sufficiently strong that cavity backaction effects can be observed, which allow to control the mechanical quality factor and can be used to drive the beam into cavity-pumped self-oscillation. By adding a microwave bypass capacitor, this detection scheme can be used simultaneously with dielectric actuation and tuning, providing a versatile transduction principle currently in use in multiple experiments in our group [Rie13, Sou13]. The strong electric gradient fields may even lead to dielectric losses inside the mechanical resonator, which can be used to characterize the resonator material.

The optimization of quality factor and transduction schemes has enables the study of coherent interactions of nanomechanical modes presented in chapter 4. Here, the in-plane and out-of-plane fundamental modes form a system of two tunable, coupled harmonic resonators. This allows to utilize nanomechanical resonators to perform coherent experi-

ments which are, to date, mostly known from quantum physics. A first step is the demonstration of Landau-Zener transitions between the two modes, while multiple transtitions clearly show coherent Stückelberg oscillations. Rabi oscillations, Ramsey fringes and Hahn echo experiments demonstrate the coherent control of the mechanical superpostion state. The measured coherence times exhibit a feature rather uncommon in two-level solid-state systems: all relaxation is caused by energy decay, there is no measurable phase relaxation process. Furthermore, the fact that all phonons reside in a collective mechanical mode leads to the absence of inhomogeneous broadening effects caused by different precession frequencies.

Samples using the on-chip superconducting niobium resonators presented in chapter 5.2 will provide superior performance at temperatures below 9 K. In combination with the low mechanical losses (and neglegible dielectric losses) of silicon nitride nanostrings at low temperatures, they will provide a nanoelectromechanical system whose performance will exceed every sample and setup presented here. This will not only enable the study of mechanical losses down to millikelvin temperatures, but will also allow to cool the mechanical resonators to temperatures far below the bath temperature of the cryostat. If an additional dc bias is connected to the superconducting cavities [Che11], the coherent experiments using the two coupled orthogonal modes can also be performed at very low temperatures, benefiting from the increased mechanical quality factor and thus increased coherence time. In the more distant future, one can also envision coupled mechanical resonators cooled close to their ground state, which might enable quantum computations using nanoelectromechanical systems [Rip12].

Appendix A

Measurement setup

The complete measurement setup used in the (latest) experiments of chapter 4.2 and chapter 5 (not all instruments are necessary for every measurement) can be seen in Fig. A.1. This is the final evolution stage of the microwave measurement setups used troughout chapters 3, 4 and 5. Depending on whether time-resolved data are taken using the spectrum analyzer or resonance curves are measured with the network analyzer, the respective connections (marked with question marks) have to be made accordingly. The green numbers throughout the figure correspond to the entries in table A.1, where detailed information about every instrument is presented. All devices with blue borders are connected to the measurement control computer, either via GPIB, the parallel port (**7**) or a PCI card (**17**). Dark red borders indicate a GPIB connection to the cryostat control computer, which can be controlled by the measurement control computer via an ethernet connection.

The power supplies are not listed in table A.1. An Agilent E3620A dual channel power supply was used to provide 12 V to **12** and 15 V to **19**, while an E3630A supplied 3.3 V to **13** and $\pm$20 V to **5**.

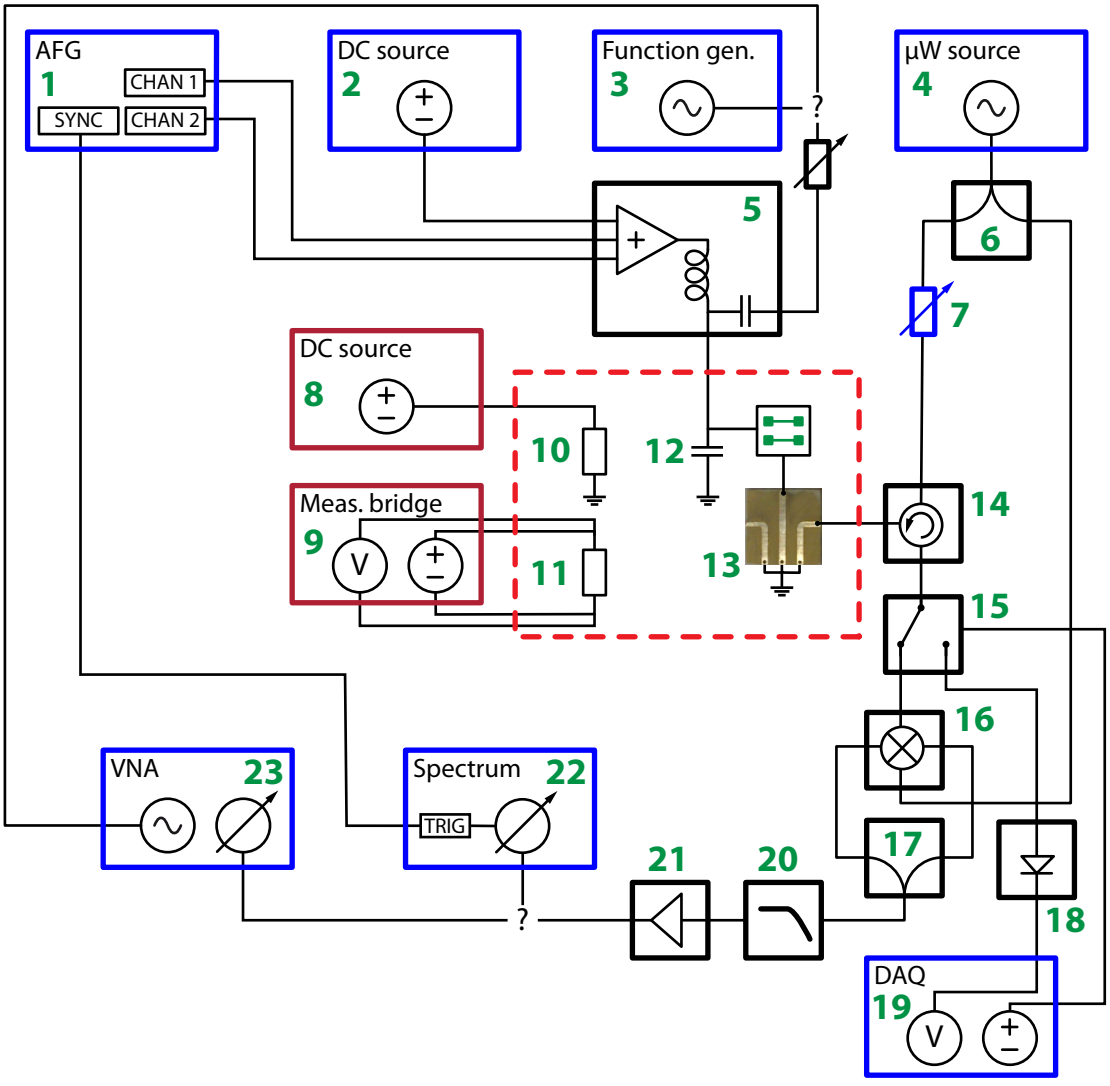

Figure A.1: Measurement setup: Schematic drawing of the complete electrical measurement setup. Blue boundaries indicate a connection to the control computer, dark red boundaries a connection to the cryostat control computer. The components inside the dashed red box are mounted inside the cryostat, and the green numbers are used as a reference in the table of used instruments.

Number	Manufacturer	Part number	Description
1	Tektronix	AFG3252	dual channel arbitrary function generator
2	Yokogawa	7651	precision voltage source
3	Agilent	33220A	waveform generator (sine&noise)
4	Rohde&Schwarz	SMA100A	low phase noise microwave signal generator
5	Stephan Manus		adding amplifier with a gain of two ($\sim$200 kHz bandwidth) and integrated bias-tee
6	Minicircuits	ZFSC-2-10G	2-10 GHz power splitter
7	Minicircuits	ZX67-15R5-PP-S	0-15.5 dB digital step attenuator
8	Agilent	E3641A	60 V computer controlled dc voltage source
9	Picowatt	AVS-47A	ac resistance bridge
10			180 Ω 1 W SMD resistor
11	Lakeshore	CX-1050-AA-1.4L	cernox thermometer
12	Johanson Tech.	500U04A182KT4S	1.8 nF ceramic single layer microwave capacitor
13	LPtec		professionally fabricated, silver-coated microstrip cavity [Kra12]
14	Lynx	15.00479.04.00	2-4 GHz circulator
15	Minicircuits	MSP2T-18-12	mechanical rf switch
16	Marki	IQ-0307-LXP	IQ mixer
17	Minicircuits	JSPQ-65W	0/90° power splitter
18	Agilent	33334C	rf detector
19	National Inst.	DAQ6014	data aquisition card
20	Minicricuits	PLP-200	200 MHz lowpass filter
21	Miteq	AU-1338	low-noise rf amplifier
22	Rohde&Schwarz	FSU26	spectrum analyzer
23	Rohde&Schwarz	ZVB4	network analyzer

Table A.1: List of instruments

Appendix B

Sample fabrication

The following section is almost identical to Appendix A.1 of [Sei12] (as the samples used in chapters 3.2, 4 and 5.1 were fabricated by M. Seitner). The different evolution steps of the fabrication are not described (see [Kre11] for the initial development of the process), but only the most recent recipe, used to fabricate the sample measured in chapters 4.2, 4.3, 4.4 and 5.1, is presented here.

The processing starts with commercially available quartz wafers coated with a 100 nm thick silicon nitride layer, already diced in $5 \cdot 5\,\mathrm{mm}^2$ chips.

- Cleaning & preparation

step	**description**
cleaning	sonificate for 3 minutes in aceton rinse in isopropanol and blow-dry with nitrogen
protective coating[1]	spin-coat with Shipley 1813 resist
marking	small scratch on top side, number on the bottom
remove coating	sonificate for 2 minutes in aceton rinse in isopropanol and blow-dry with nitrogen

- Defining the gold electrodes

step	**description**
deposit resist	spin-coat PMMA 950k A6 1 s 800 rpm, 30 s 5000 rpm bake for at least 60 min at 120°
conductive layer	evaporate 3 nm of chromium onto the resist
SEM lithography	10 kV acceleration voltage, 20 µm aperture 100 µC/cm^2 dose
chromium etch	30 s in *Merck Selectipur 111547* chromium etchant[2] rinse in water

[1] If not already applied prior to dicing the wafer.

[2] It is important to use a chromium etchant based on nitric acid, as solutions based on perchloric acid attack the resist layer and lead to over-exposed structures.

step	description
develop	50 s in isopropanol:MIBK 3:1 rinse in isopropanol, blow-dry with nitrogen
evaporation	3 nm chromium (adhesion layer) 140 nm gold
lift-off	bathe in aceton (or in 100° DMSO over night in case of liftoff problems) rinse in isopropanol, blow-dry with nitrogen

- Defining the beam

step	description
deposit resist	spin-coat PMMA 950k A6 1 s 800 rpm, 30 s 5000 rpm bake for at least 60 min at 120°
conductive layer	evaporate 3 nm of chromium onto the resist
SEM lithography	10 kV acceleration voltage, 20 µm aperture 140 µC/cm^2 dose
chromium etch	30 s in *Selectipur 111547* chromium etchant rinse in water
develop	50 s in isopropanol:MIBK 3:1 rinse in isopropanol, blow-dry with nitrogen
evaporation	30 nm cobalt
lift-off	bathe in aceton rinse in isopropanol, blow-dry with nitrogen

- Dry&wet etch

step	description
ICPRIE dry etch	4 sccm Ar and 2 sccm SF_6 at 2 mTorr with an ICP power of 70 W and an RF power of 35 W, duration 9 min
mask removal	90 s in "piranha" (H_2SO_4 : H_2O_2 1:1)
underetching	160 s in buffered HF
drying	rinse in water remove from hot isopropanol and immediately blow-dry with nitrogen

Appendix C

Supplement to "Damping of Nanomechanical Resonators"

Published as Supplemental Material to *Physical Review Letters* **105**, 027205 (2010), reference [Unt10b].

1 Damping Model

In a Zener model, an oscillating strain $\epsilon(t) = \Re[\epsilon[\omega]\exp[i\omega t]]$ and its accompanying stress $\sigma[t] = \Re[\sigma[\omega]\exp[i\omega t]]$ are out-of phase, described by a frequency-dependent, complex elastic modulus $\sigma(\omega) = E[\omega]\epsilon[\omega] = (E_1[\omega] + iE_2[\omega])\epsilon[\omega]$. This leads to an energy loss per oscillation in a test volume $\delta V = \delta A \cdot \delta s$ of cross-section δA and length δs.

$$\Delta U_{\delta V} = \int_T dt \underbrace{EA\epsilon[t]}_{\text{force}} \cdot \underbrace{\frac{\partial}{\partial t}\left(s\epsilon[t]\right)}_{\text{velocity}} = \pi \delta A \delta s E_2 \epsilon^2 \tag{1}$$

We now employ this model for our case, namely a pre-stressed, rectangular beam of length l, width w and height h, corresponding here to the x,y,z-direction, respectively. The origin of the coordinate system is centered in the beam. The resonator performs oscillations in the z-direction and, as we consider a continuum elastic model, there will be no dependence on the y-direction. For a beam of high aspect ratio $l \gg h$ and small oscillation amplitude, the displacement of the m-th mode can be approximately written $u_m[x, y, z] = u_m[x]$. During oscillation, a small test volume within the beam undergoes oscillating strain $\epsilon_m[x, z, t]$.
This strain arises because of the bending of the beam as well as its elongation as it is displaced. The stress caused by the overall elongation is quadratic in displacement, therefore it occurs at twice the oscillating frequency.

$$\begin{aligned}\epsilon_m[x,z,t] &= \underbrace{\frac{1}{2}\left(\frac{\partial}{\partial x}u_m[x]\Re[\exp[i\omega t]]\right)^2}_{\text{elongation}} + \underbrace{z\frac{\partial^2}{\partial x^2}u_m[x]\Re[\exp[i\omega t]]}_{\text{bending}} \\ &= \frac{1}{2}\left(\frac{\partial}{\partial x}u_m[x]\right)^2 \frac{1}{2}\left(1 + \Re[\exp[2i\omega t]]\right) + z\frac{\partial^2}{\partial x^2}u_m[x]\Re[\exp[i\omega t]]\end{aligned} \tag{2}$$

Inserting this into eq. 1 and integrating over the cross-section $w \cdot h$, the accompanying energy losses can be seen to separate into elongation and displacement caused terms.

$$\Delta U_{w\cdot h} = \pi s E_2[2\omega]\frac{wh}{8}\left(\frac{\partial}{\partial x}u_m[x]\right)^4 + \pi s E_2[\omega]\frac{wh^3}{12}\left(\frac{\partial^2}{\partial x^2}u_m[x]\right)^2 \tag{3}$$

Integrating over the length yields the total energy loss of a particular mode $\Delta U = \int_{-l/2}^{l/2} dx \Delta U_{w\cdot h}$. In the case that E_2 is only weakly frequency-dependent, it turns out that for our geometries the elongation term is several orders of magnitude $(10^5 - 10^7)$ smaller than the term arising from the bending. The energy loss therefore may be simplified and writes

$$\Delta U \approx \Delta U_{\text{bending}} = \pi E_2 \frac{wh^3}{12}\int_{-l/2}^{l/2} dx \left(\frac{\partial^2}{\partial x^2}u_m[x]\right)^2 \tag{4}$$

2 Elastic Energy of a Pre-Stressed Beam

A volume δV subject to a longitudinal pre-stress σ_0 stores the energy $U_{\delta V}$ when strained; E_1 is assumed to be frequency independent in the experimental range (5-100 MHz)

$$U_{\delta V} = sA\left(\sigma_0\epsilon + \frac{1}{2}E_1\epsilon^2\right) \tag{5}$$

To apply this formula to the case of an oscillating pre-stressed beam, we insert eq. $2|_{t=0}$ (maximum displacement) and integrate over the cross-section to obtain

$$U_{w\cdot h} = \frac{1}{2}E_1\left(\frac{1}{4}wh\left(\frac{\partial}{\partial x}u_m[x]\right)^4 + \frac{1}{12}wh^3\left(\frac{\partial^2}{\partial x^2}u_m[x]\right)^2\right) + \frac{1}{2}swh\sigma_0\left(\frac{\partial}{\partial x}u_m[x]\right)^2 \tag{6}$$

Analog to eq. 3 we can omit the first term in the brackets; integrating over the length yields

$$U \approx \int_{-l/2}^{l/2} dx\Big(\underbrace{\frac{1}{2}wh\sigma_0\left(\frac{\partial}{\partial x}u_m[x]\right)^2}_{\text{elongation}} + \underbrace{\frac{1}{24}E_1wh^3\left(\frac{\partial^2}{\partial x^2}u_m[x]\right)^2}_{\text{bending}}\Big) \tag{7}$$

We can therefore divide the total energy into parts arising from the elongation and the bending of the beam. Depending on the magnitude of the pre-stress, either of the two energies can dominate as seen in Fig. 3a of the main text. We have checked that the kinetic energy $U_{\mathrm{kin}} = 1/2\rho(\omega_m)^2 \int_{l/2}^{l/2} dx(u_m[x])^2$; ($\omega_m/(2\pi), \rho$: resonance frequency, material density, respectively) equals the total elastic energy, as expected.

3 Frequency-dependent Loss Modulus

There is no obvious reason that the imaginary part of Young's modulus E_2 should be completely frequency-independent. We therefore assume that E_2 obeys a (weak) power-law and chose the ansatz:

$$E_2[f] = E_2(f/f_0)^a \tag{8}$$

Fitting our data with the thus extended theory, we achieve a very precise agreement of measured and calculated quality factors, as seen in Fig. S1. The resulting exponent is $a = 0.075$; E_2 varies therefore by 20% when f changes by one order of magnitude.

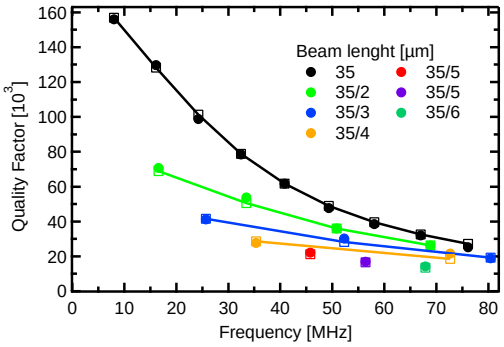

Figure 1: *Resonance frequencies and quality factors of the resonators* **a** Measured quality factor and resonance frequency of several harmonics of beams with different lengths (color-coded) are displayed as filled circles (same data as in Fig. 2 of the main text). The resonance frequencies are reproduced by a continuum model; we calculate the quality factors using a model based on the strain caused by the displacement. In contrast to Fig. 2 of the main text and Fig. S2 we here allow E_2 to be (weakly) frequency-dependent.

4 Linewidth of the Mechanical Resonance

The elastic energy of a harmonic oscillator is given by $U = 1/2 m_{\mathrm{eff}} \omega_0^2 x_0^2$ with $m_{\mathrm{eff}}, \omega_0, x_0$ being effective mass, resonance frequency and displacement, respectively. If we assume the effective mass to be energy-independent, it applies $\omega_0 \propto \sqrt{U}$. Recalling the definition of the quality factor $Q = 2\pi U/\Delta U \propto U$, one obtains for the for the Full Width at Half Max (FWHM) of the resonance

$$\Delta\omega = \frac{\omega_0}{Q} \propto \frac{\sqrt{U}}{U/\Delta U} = \frac{\Delta U}{\sqrt{U}} \tag{9}$$

As in the main text, the energy depends on the applied overall tensile stress. Figure 3 shows a numerical calculation of the resulting linewidth vs. applied stress; one can see that increase in energy loss per oscillation is dominated by the increase in energy, resulting in a decreased linewidth. The exact effective mass is included in this calculation; as it changes by less than 20%, the above assumption is justified.

5 Microscopic Damping Mechanisms

We start with clamping losses as discussed, e.g., in ref. [1, 2], i. e. the radiation of acoustic waves into the bulk caused by inertial forces exerted by the oscillating beam. With a sound velocity in silicon of $v_{\mathrm{Si}} \approx 8\,\mathrm{km/s}$, the wavelength of the acoustic waves radiated at a frequency of 10 MHz from the clamps into the bulk will be greater than 500 µm, and

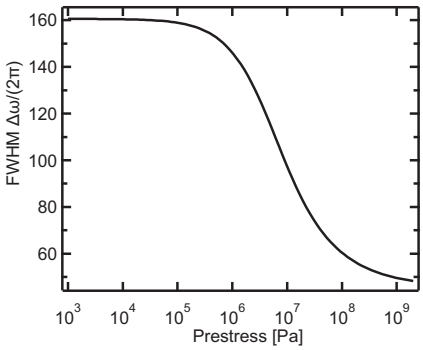

Figure 2: *Linewidth of the mechanical resonance* The calculated linewidths (FWHM) for the fundamental mode of the beam with $l = 35$µm are displayed vs. applied overall stress.

thus substantially larger than the length of our resonators. Considering each clamping point as a source of an identical wave propagating into the substrate, one would expect that mostly constructive/destructive interference would occur for in-/out-of-phase shear forces exerted by the clamping points, respectively. With clamping losses being important, one would therefore expect that spatially asymmetric modes with no moving center of mass exhibit significant higher quality factors than symmetric ones [1]. Another way to illuminate this difference is that symmetric modes give rise to a net force on the substrate, whereas asymmetric modes yield a torque. Since the measurement (Fig. 2) does not display such an alternating behavior of the quality factors with mode index m (best seen for the longest beam), clamping losses are likely to be of minor importance.

The next damping mechanism we consider are phonon-assisted losses within the beam. At elevated temperatures, at least two effects arise, the first being thermoelastic damping: because of the oscillatory bending, the beam is compressed and stretched at opposite sides. Since such volume changes are accompanied by work, the local temperature in the beam will deviate from the mean. For large aspect ratios as in our case, the most prominent gradient is in the z direction. The resulting thermal flow leads to mechanical dissipation. We extend existing model calculations [3] to include the tensile stress of our beams. Using relevant macroscopic material parameters such as thermal conductivity, expansion coefficient and heat capacity we derive Q-values that are typically three to four orders of magnitudes larger than found in the experiment. Therefore, heat flow can be safely neglected as the dominant damping mechanism. In addition, the calculated thermal relaxation rate corresponds to approximately 2 GHz, so the experiment is in the so-called adiabatic regime. Consequently, one would expect the energy loss to be proportional to the oscillation frequency, in contrast to the assumption of a frequency independent E_2 and our experimental findings.

Another local phonon-based damping effect is the Akhiezer-effect [4]; it is a consequence of the fact that phonon frequencies are modulated by strain, parameterized by the Grüneisen tensor. If different phonon modes (characterized by their wave vector and phonon branch) are affected differently, the occupancy of each mode corresponds to a different temperature. This imbalance relaxes towards a local equilibrium temperature, giving rise to mechanical damping. In a model calculation applying this concept to the oscillatory motion of nanobeams [5], the authors find in the case of large aspect ratios length/height that the thermal heat flow responsible for thermoelastic damping dominates the energy loss by the Akhiezer effect. We thus can safely assume this mechanism to be also negligible in our experiment.

6 Reduced Quality Factor

We fabricated a set of resonators, shown in Fig. S1a, that showed lower quality factors than the ones presented in the main text (Fig. 2); we attribute this reduction to a non-optimized RIE-etch step. As in the main article, it is possible to reproduce the quality factors using a single fit parameter, namely the imaginary part of Young's modulus E_2. The ratio of the two sets of quality factors is displayed in Fig. S1 b and can be seen to be around 1.4 with no obvious dependence on resonance frequency, mode index or length. A non-optimized etch step causes additional surface roughness and the addition of impurities, thereby increasing the density of defect states. As there is no obvious reason why another damping mechanism should be thereby influenced, we interpret this as another strong indication that the dominant microscopic damping mechanism is caused by localized defect states.

[1] I. Wilson-Rae, private communication

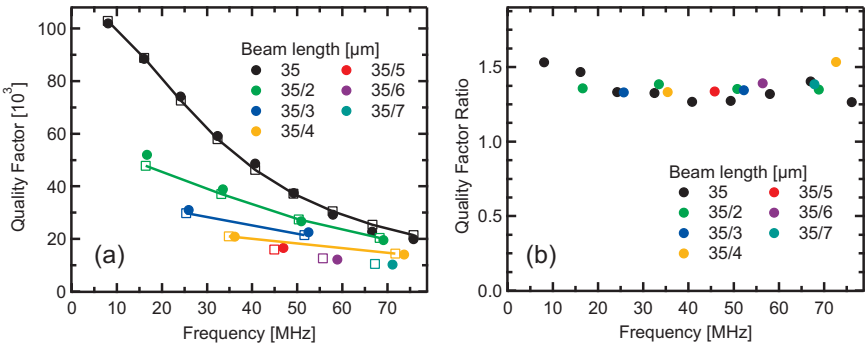

Figure 3: *Comparison of the resonance frequencies and quality factors of the sets of resonators* **a** Measured quality factor and resonance frequency of several harmonics of beams with different lengths (color-coded) are displayed as filled circles. The resonance frequencies are reproduced by a continuum model; a model based on the strain caused by the displacement allows us to calculate the quality factors, shown as hollow squares. The uniform reduction of the Q-factors is attributed to an non-optimized RIE-etch. **b** The ratio of the quality factors of the two sets resonators (Fig. 2 main article and Fig. S2a) are displayed vs. frequency, being approximately constant.

7 Spatially Inhomogeneous Loss Modulus

Our model calculation assumes a spatially homogeneous imaginary Young's Modulus E_2. In the view of thickness-dependent quality factors of Micro-Cantilevers [6] and our own experimental findings, we show that a generalization has no influence to our model.

We let E_2 now depend on the position along the direction of displacement of the resonator $E_2 = E_2[z]$. The elastic energy is obviously not affected. The energy loss now reads with $\epsilon[x,z] \equiv z\epsilon_0[x]$:

$$\Delta U = \pi \int_V E_2[z]\epsilon[x,z]^2 = \pi w \int_{-h/2}^{h/2} dz z^2 E_2[z] \cdot \int_{-l/2}^{l/2} dx \epsilon_0[x]^2 \tag{10}$$

The integral can be separated into the x and z direction; we now regard the ratio of two different modes (i,j) with the same $E_2[z]$ (irrespective of whether the indices refer to different harmonics or beam lengths):

$$\frac{\Delta U_i}{\Delta U_j} = \frac{\int_h dz z^2 E_2[z]}{\int_h dz z^2 E_2[z]} \cdot \frac{\int_l dx \epsilon_{i,0}^2}{\int_l dx \epsilon_{j,0}^2} \tag{11}$$

The ratio of the energy loss and therefore the quality factors can be seen not to be influenced by the exact z-dependence, the same applies if one regards $E_2 = E_2[y]$. In other words, our model will hold true for any variance but cannot resolve these either.

References

[1] Z. Hao, A. Erbil, and F. Ayazi, Sensors and Actuators A: Physical **109**, 156–164 (2003).

[2] I. Wilson-Rae, Phys. Rev. B **77**, 245 418 (2008).

[3] R. Lifshitz and M. L. Roukes, Phys. Rev. B **61**, 5600–5609 (2000).

[4] A. Akhieser, Journal of Physics-ussr **1**, 277–287 (1939).

[5] A. A. Kiselev and G. J. Iafrate, Phys. Rev. B **77**, 205 436 (2008).

[6] K. Y. Yasumura, T. D. Stowe, E. M. Chow, T. Pfafman, T. W. Kenny, B. C. Stipe, and D. Rugar, Journal of Microelectromechanical Systems **9**, 117–125 (2000).

Bibliography

[Ane09] G. Anetsberger, O. Arcizet, Q. P. Unterreithmeier, R. Riviere, A. Schliesser, E. M. Weig, J. P. Kotthaus, and T. J. Kippenberg. Near-field cavity optomechanics with nanomechanical oscillators. *Nature Phys.* **5**, 909 (2009).

[Ane10a] G. Anetsberger. *Novel Cavity Optomechanical Systems at the Micro- and Nanoscale and Quantum Measurements of Nanomechanical Oscillators*. Ph.D. thesis, Ludwig-Maximilians-Universität München (2010).

[Ane10b] G. Anetsberger, E. Gavartin, O. Arcizet, Q. P. Unterreithmeier, E. M. Weig, M. L. Gorodetsky, J. P. Kotthaus, and T. J. Kippenberg. Measuring nanomechanical motion with an imprecision below the standard quantum limit. *Phys. Rev. A* **82**, 061804 (2010).

[Arc06] O. Arcizet, P.-F. Cohadon, T. Briant, M. Pinard, and A. Heidmann. Radiation-pressure cooling and optomechanical instability of a micromirror. *Nature* **444**, 71 (2006).

[Arc09] O. Arcizet, R. Rivière, A. Schliesser, G. Anetsberger, and T. J. Kippenberg. Cryogenic properties of optomechanical silica microcavities. *Phys. Rev. A* **80**, 021803 (2009).

[Arl06] J. L. Arlett, J. R. Maloney, B. Gudlewski, M. Muluneh, and M. L. Roukes. Self-Sensing Micro- and Nanocantilevers with Attonewton-Scale Force Resolution. *Nano Lett.* **6**, 1000 (2006).

[Aza07] N. O. Azak, M. Y. Shagam, D. M. Karabacak, K. L. Ekinci, D. H. Kim, and D. Y. Jang. Nanomechanical displacement detection using fiber-optic interferometry. *Appl. Phys. Lett.* **91**, 093112 (2007).

[Bhu11] H. Bhugra, S. Lee, W. Pan, Y. Wang, and D. Lei. Reliability of next generation high performance pMEMS™ resonator oscillators. In *Frequency Control and the European Frequency and Time Forum (FCS), 2011 Joint Conference of the IEEE International*, pages 1–4 (2011).

[Blu11] H. Bluhm, S. Foletti, I. Neder, M. Rudner, D. Mahalu, V. Umansky, and A. Yacoby. Dephasing time of GaAs electron-spin qubits coupled to a nuclear bath exceeding 200 µs. *Nature Phys.* **7**, 109 (2011).

[Cha11] J. Chan, T. P. M. Alegre, A. H. Safavi-Naeini, J. T. Hill, A. Krause, S. Groblacher, M. Aspelmeyer, and O. Painter. Laser cooling of a nanomechanical oscillator into its quantum ground state. *Nature* **478**, 89 (2011).

[Cha12] J. Chaste, A. Eichler, J. Moser, G. Ceballos, R. Rurali, and A. Bachtold. A nanomechanical mass sensor with yoctogram resolution. *Nature Nano.* **7**, 301 (2012).

[Che11] F. Chen, A. J. Sirois, R. W. Simmonds, and A. J. Rimberg. Introduction of a dc bias into a high-Q superconducting microwave cavity. *Appl. Phys. Lett.* **98**, 132509 (2011).

[Cho82] R. Chow, W. A. Lanford, W. Ke-Ming, and R. S. Rosler. Hydrogen content of a variety of plasma-deposited silicon nitrides. *J. Appl. Phys.* **53**, 5630 (1982).

[Cho10] A. Cho. The First Quantum Machine. *Science* **330**, 1604 (2010).

[Cle96] A. N. Cleland and M. L. Roukes. Fabrication of high frequency nanometer scale mechanical resonators from bulk Si crystals. *Appl. Phys. Lett.* **69**, 2653 (1996).

[Dea09] R. Dean and A. Luque. Applications of Microelectromechanical Systems in Industrial Processes and Services. *IEEE T. Ind. Electron.* **56**, 913 (2009).

[Dra06] G. W. F. Drake, editor. *Springer Handbook of Atomic, Molecular, and Optical Physics*. Springer (2006).

[E05] K. E. Electromechanical Transducers at the Nanoscale: Actuation and Sensing of Motion in Nanoelectromechanical Systems (NEMS). *Small* **1**, 786 (2005).

[Fau12a] T. Faust, P. Krenn, S. Manus, J. P. Kotthaus, and E. M. Weig. Microwave cavity-enhanced transduction for plug and play nanomechanics at room temperature. *Nature Commun.* **3**, 728 (2012).

[Fau12b] T. Faust, J. Rieger, M. J. Seitner, J. P. Kotthaus, and E. M. Weig. Coherent control of a nanomechanical two-level system. *ArXiv e-prints* **1212.3172** (2012).

[Fau12c] T. Faust, J. Rieger, M. J. Seitner, P. Krenn, J. P. Kotthaus, and E. M. Weig. Nonadiabatic Dynamics of Two Strongly Coupled Nanomechanical Resonator Modes. *Phys. Rev. Lett.* **109**, 037205 (2012).

[Fen08] X. L. Feng, C. J. White, A. Hajimiri, and M. L. Roukes. A self-sustaining ultrahigh-frequency nanoelectromechanical oscillator. *Nature Nano.* **3**, 342 (2008).

[Gig06] S. Gigan, H. R. Böhm, M. Paternostro, F. Blaser, G. Langer, J. B. Hertzberg, K. C. Schwab, D. Bäuerle, M. Aspelmeyer, and A. Zeilinger. Self-cooling of a micromirror by radiation pressure. *Nature* **444**, 67 (2006).

[Hag01] C. Hagleitner, A. Hierlemann, D. Lange, A. Kummer, N. Kerness, O. Brand, and H. Baltes. Smart single-chip gas sensor microsystem. *Nature* **414**, 293 (2001).

[Hah50] E. L. Hahn. Spin Echoes. *Phys. Rev.* **80**, 580 (1950).

[Ham07] G. Hammer, S. Wuensch, M. Roesch, K. Ilin, E. Crocoll, and M. Siegel. Superconducting coplanar waveguide resonators for detector applications. *Supercond. Sci. Technol.* **20**, S408 (2007).

[Han07] R. Hanson, L. P. Kouwenhoven, J. R. Petta, S. Tarucha, and L. M. K. Vandersypen. Spins in few-electron quantum dots. *Rev. Mod. Phys.* **79**, 1217 (2007).

[Hei10] G. Heinrich, J. G. E. Harris, and F. Marquardt. Photon shuttle: Landau-Zener-Stückelberg dynamics in an optomechanical system. *Phys. Rev. A* **81**, 011801 (2010).

[Hof09] M. Hofheinz, H. Wang, M. Ansmann, R. C. Bialczak, E. Lucero, M. Neeley, A. D. O'Connell, D. Sank, J. Wenner, J. M. Martinis, and A. N. Cleland. Synthesizing arbitrary quantum states in a superconducting resonator. *Nature* **459**, 546 (2009).

[Ili05] B. Ilic, S. Krylov, K. Aubin, R. Reichenbach, and H. G. Craighead. Optical excitation of nanoelectromechanical oscillators. *Appl. Phys. Lett.* **86**, 193114 (2005).

[Jäc72] J. Jäckle. On the ultrasonic attenuation in glasses at low temperatures. *Z. Phys.* **257**, 212 (1972).

[Jen08] K. Jensen, K. Kim, and A. Zettl. An atomic-resolution nanomechanical mass sensor. *Nature Nano.* **3**, 533 (2008).

[Jud01] J. W. Judy. Microelectromechanical systems (MEMS): fabrication, design and applications. *Smart Mater. Struct.* **10**, 1115 (2001).

[Kar05] D. Karabacak, T. Kouh, and K. L. Ekinci. Analysis of optical interferometric displacement detection in nanoelectromechanical systems. *J. Appl. Phys.* **98**, 124309 (2005).

[Kar11] R. B. Karabalin, R. Lifshitz, M. C. Cross, M. H. Matheny, S. C. Masmanidis, and M. L. Roukes. Signal Amplification by Sensitive Control of Bifurcation Topology. *Phys. Rev. Lett.* **106**, 094102 (2011).

[Kle06] D. Kleckner and D. Bouwmeester. Sub-kelvin optical cooling of a micromechanical resonator. *Nature* **444**, 75 (2006).

[Kno03] R. G. Knobel and A. N. Cleland. Nanometre-scale displacement sensing using a single electron transistor. *Nature* **424**, 291 (2003).

[Koz06] I. Kozinsky, H. W. C. Postma, I. Bargatin, and M. L. Roukes. Tuning nonlinearity, dynamic range, and frequency of nanomechanical resonators. *Appl. Phys. Lett.* **88**, 253101 (2006).

[Koz07] I. Kozinsky, H. W. C. Postma, O. Kogan, A. Husain, and M. L. Roukes. Basins of Attraction of a Nonlinear Nanomechanical Resonator. *Phys. Rev. Lett.* **99**, 207201 (2007).

[Kra12] T. Krastev. *Entwicklung und Optimierung von Mikrowellenresonatoren zur dielektrischen Detektion von schwingenden SiN-Nanobalken*. Bachelor thesis, Ludwig-Maximilians-Universität München (2012).

[Kre11] P. Krenn. *Heterodyne dielektrische Detektion von nanomechanischen Resonatoren*. Master's thesis, Ludwig-Maximilians-Universität München (2011).

[Lan32] L. D. Landau. Zur Theorie der Energieübertragung. *Phys. Z. Sowjetunion* **2**, 46 (1932).

[Lau89] W. S. Lau, S. J. Fonash, and J. Kanicki. Stability of electrical properties of nitrogen-rich, silicon-rich, and stoichiometric silicon nitride films. *J. Appl. Phys.* **66**, 2765 (1989).

[Li10] M. Li, E. B. Myers, H. X. Tang, S. J. Aldridge, H. C. McCaig, J. J. Whiting, R. J. Simonson, N. S. Lewis, and M. L. Roukes. Nanoelectromechanical Resonator Arrays for Ultrafast, Gas-Phase Chromatographic Chemical Analysis. *Nano Lett.* **10**, 3899 (2010).

[Luc04] S. Lucyszyn. Review of radio frequency microelectromechanical systems technology. *IEE Proc.-Sci. Meas. Technol.* **151**, 93 (2004).

[Lud00] S. Ludwig. *Tieftemperatureigenschaften von OH^- bzw. OD^- dotierten Alkalihalogenidkristallen*. Ph.D. thesis, Rupprecht-Karls-Universität Heidelberg (2000).

[Lud13] S. Ludwig. Private communication (2013).

[Mah08] I. Mahboob and H. Yamaguchi. Parametrically pumped ultrahigh Q electromechanical resonator. *Appl. Phys. Lett.* **92**, 253109 (2008).

[Maj32] E. Majorana. Atomi orientati in campo magnetico variabile. *Il Nuovo Cimento* **9**, 43 (1932).

[Mam01] H. J. Mamin and D. Rugar. Sub-attonewton force detection at millikelvin temperatures. *Appl. Phys. Lett.* **79**, 3358 (2001).

[Mar07] F. Marquardt, J. P. Chen, A. A. Clerk, and S. M. Girvin. Quantum Theory of Cavity-Assisted Sideband Cooling of Mechanical Motion. *Phys. Rev. Lett.* **99**, 093902 (2007).

[Mas07] S. C. Masmanidis, R. B. Karabalin, I. De Vlaminck, G. Borghs, M. R. Freeman, and M. L. Roukes. Multifunctional Nanomechanical Systems via Tunably Coupled Piezoelectric Actuation. *Science* **317**, 780 (2007).

[Met04] C. H. Metzger and K. Karrai. Cavity cooling of a microlever. *Nature* **432**, 1002 (2004).

[Nov10] L. Novotny. Strong coupling, energy splitting, and level crossings: A classical perspective. *Am. J. Phys.* **78**, 1199 (2010).

[O'C10] A. D. O'Connell, M. Hofheinz, M. Ansmann, R. C. Bialczak, M. Lenander, E. Lucero, M. Neeley, D. Sank, H. Wang, M. Weides, J. Wenner, J. M. Martinis, and A. N. Cleland. Quantum ground state and single-phonon control of a mechanical resonator. *Nature* **464**, 697 (2010).

[Oka09] H. Okamoto, T. Kamada, K. Onomitsu, I. Mahboob, and H. Yamaguchi. Optical Tuning of Coupled Micromechanical Resonators. *Appl. Phys. Express* **2**, 062202 (2009).

[Oka12] H. Okamoto, A. Gourgout, C.-Y. Chang, K. Onomitsu, I. Mahboob, E. Y. Chang, and H. Yamaguchi. Coherent phonon manipulation in coupled mechanical resonators. *ArXiv e-prints* **1212.3097** (2012).

[Oli05] W. D. Oliver, Y. Yu, J. C. Lee, K. K. Berggren, L. S. Levitov, and T. P. Orlando. Mach-Zehnder Interferometry in a Strongly Driven Superconducting Qubit. *Science* **310**, 1653 (2005).

[Per11] S. Perisanu, T. Barois, P. Poncharal, T. Gaillard, A. Ayari, S. T. Purcell, and P. Vincent. The mechanical resonances of electrostatically coupled nanocantilevers. *Appl. Phys. Lett.* **98**, 063110 (2011).

[Pet05] J. R. Petta, A. C. Johnson, J. M. Taylor, E. A. Laird, A. Yacoby, M. D. Lukin, C. M. Marcus, M. P. Hanson, and A. C. Gossard. Coherent Manipulation of Coupled Electron Spins in Semiconductor Quantum Dots. *Science* **309**, 2180 (2005).

[Poh02] R. O. Pohl, X. Liu, and E. Thompson. Low-temperature thermal conductivity and acoustic attenuation in amorphous solids. *Rev. Mod. Phys.* **74**, 991 (2002).

[Rab37] I. I. Rabi. Space Quantization in a Gyrating Magnetic Field. *Phys. Rev.* **51**, 652 (1937).

[Ram50] N. F. Ramsey. A Molecular Beam Resonance Method with Separated Oscillating Fields. *Phys. Rev.* **78**, 695 (1950).

[Reg08] C. A. Regal, J. D. Teufel, and K. W. Lehnert. Measuring nanomechanical motion with a microwave cavity interferometer. *Nature Phys.* **4**, 555 (2008).

[Rei08] D. J. Reilly, J. M. Taylor, J. R. Petta, C. M. Marcus, M. P. Hanson, and A. C. Gossard. Suppressing Spin Qubit Dephasing by Nuclear State Preparation. *Science* **321**, 817 (2008).

[Rib12] H. Ribeiro. Private communication (2012).

[Rie12] J. Rieger, T. Faust, M. J. Seitner, J. P. Kotthaus, and E. M. Weig. Frequency and Q factor control of nanomechanical resonators. *Appl. Phys. Lett.* **101**, 103110 (2012).

[Rie13] J. Rieger, A. Isacsson, M. J. Seitner, J. P. Kotthaus, and E. M. Weig. Nanoscale acoustic impedance imaging with a mechanical point contact. *In preparation* (2013).

[Rip12] S. Rips and M. J. Hartmann. Quantum Information Processing with Nanomechanical Qubits. *ArXiv e-prints* **1211.4456** (2012).

[Riv11] R. Rivière, S. Deléglise, S. Weis, E. Gavartin, O. Arcizet, A. Schliesser, and T. J. Kippenberg. Optomechanical sideband cooling of a micromechanical oscillator close to the quantum ground state. *Phys. Rev. A* **83**, 063835 (2011).

[Roc10] T. Rocheleau, T. Ndukum, C. Macklin, J. B. Hertzberg, A. A. Clerk, and K. C. Schwab. Preparation and detection of a mechanical resonator near the ground state of motion. *Nature* **463**, 72 (2010).

[Roo09] D. Roodenburg, J. W. Spronck, H. S. J. van der Zant, and W. J. Venstra. Buckling beam micromechanical memory with on-chip readout. *Appl. Phys. Lett.* **94**, 183501 (2009).

[Rug89] D. Rugar, H. J. Mamin, and P. Guethner. Improved fiber-optic interferometer for atomic force microscopy. *Appl. Phys. Lett.* **55**, 2588 (1989).

[Sam06] A. Sampathkumar, T. W. Murray, and K. L. Ekinci. Photothermal operation of high frequency nanoelectromechanical systems. *Appl. Phys. Lett.* **88**, 223104 (2006).

[Sch06] S. Schmid, M. Wendlandt, D. Junker, and C. Hierold. Nonconductive polymer microresonators actuated by the Kelvin polarization force. *Appl. Phys. Lett.* **89**, 163506 (2006).

[Sch08] A. Schliesser, R. Riviere, G. Anetsberger, O. Arcizet, and T. J. Kippenberg. Resolved-sideband cooling of a micromechanical oscillator. *Nature Phys.* **4**, 415 (2008).

[Sei12] M. J. Seitner. *Mechanische und dielektrische Manipulation nanomechanischer Resonatoren*. Master's thesis, Ludwig-Maximilians-Universität München (2012).

[Sek02] L. Sekaric, D. W. Carr, S. Evoy, J. M. Parpia, and H. G. Craighead. Nanomechanical resonant structures in silicon nitride: fabrication, operation and dissipation issues. *Sensor. Actuat. A-Phys.* **101**, 215 (2002).

[She10] S. Shevchenko, S. Ashhab, and F. Nori. Landau–Zener–Stückelberg interferometry. *Phys. Rep.* **492**, 1 (2010).

[Sil09] M. A. Sillanpää, J. Sarkar, J. Sulkko, J. Muhonen, and P. J. Hakonen. Accessing nanomechanical resonators via a fast microwave circuit. *Appl. Phys. Lett.* **95**, 011909 (2009).

[Sou09] D. R. Southworth, R. A. Barton, S. S. Verbridge, B. Ilic, A. D. Fefferman, H. G. Craighead, and J. M. Parpia. Stress and Silicon Nitride: A Crack in the Universal Dissipation of Glasses. *Phys. Rev. Lett.* **102**, 225503 (2009).

[Sou13] D. R. Southworth and E. M. Weig. *in preparation* (2013).

[Ste12] J. Stehlik, Y. Dovzhenko, J. R. Petta, J. R. Johansson, F. Nori, H. Lu, and A. C. Gossard. Landau-Zener-Stückelberg interferometry of a single electron charge qubit. *Phys. Rev. B* **86**, 121303 (2012).

[Sto97] T. D. Stowe, K. Yasumura, T. W. Kenny, D. Botkin, K. Wago, and D. Rugar. Attonewton force detection using ultrathin silicon cantilevers. *Appl. Phys. Lett.* **71**, 288 (1997).

[Stu32] E. C. G. Stueckelberg. Theorie der unelastischen Stösse zwischen Atomen. *Helv. Phys. Acta* **5**, 369 (1932).

[Teu08] J. D. Teufel, C. A. Regal, and K. W. Lehnert. Prospects for cooling nanomechanical motion by coupling to a superconducting microwave resonator. *New J. Phys.* **10**, 095002 (2008).

[Teu09] J. D. Teufel, T. Donner, M. A. Castellanos-Beltran, J. W. Harlow, and K. W. Lehnert. Nanomechanical motion measured with an imprecision below that at the standard quantum limit. *Nature Nano.* **4**, 820 (2009).

[Teu11] J. D. Teufel, T. Donner, D. Li, J. W. Harlow, M. S. Allman, K. Cicak, A. J. Sirois, J. D. Whittaker, K. W. Lehnert, and R. W. Simmonds. Sideband cooling of micromechanical motion to the quantum ground state. *Nature* **475**, 359 (2011).

[Tho08] J. D. Thompson, B. M. Zwickl, A. M. Jayich, F. Marquardt, S. M. Girvin, and J. G. E. Harris. Strong dispersive coupling of a high-finesse cavity to a micromechanical membrane. *Nature* **452**, 72 (2008).

[Tie92] D. Tielbürger, R. Merz, R. Ehrenfels, and S. Hunklinger. Thermally activated relaxation processes in vitreous silica: An investigation by Brillouin scattering at high pressures. *Phys. Rev. B* **45**, 2750 (1992).

[Unt09] Q. P. Unterreithmeier, E. M. Weig, and J. P. Kotthaus. Universal transduction scheme for nanomechanical systems based on dielectric forces. *Nature* **458**, 1001 (2009).

[Unt10a] Q. P. Unterreithmeier. *Gradient Field Transduction of Nanomechanical Resonators*. Ph.D. thesis, Ludwig-Maximilians-Universität München (2010).

[Unt10b] Q. P. Unterreithmeier, T. Faust, and J. P. Kotthaus. Damping of Nanomechanical Resonators. *Phys. Rev. Lett.* **105**, 027205 (2010).

[Unt10c] Q. P. Unterreithmeier, T. Faust, and J. P. Kotthaus. Nonlinear switching dynamics in a nanomechanical resonator. *Phys. Rev. B* **81**, 241405 (2010).

[Unt10d] Q. P. Unterreithmeier, T. Faust, S. Manus, and J. P. Kotthaus. On-Chip Interferometric Detection of Nanomechanical Motion. *Nano Lett.* **10**, 887 (2010).

[Vac05] R. Vacher, E. Courtens, and M. Foret. Anharmonic versus relaxational sound damping in glasses. II. Vitreous silica. *Phys. Rev. B* **72**, 214205 (2005).

[Van05] L. M. K. Vandersypen and I. L. Chuang. NMR techniques for quantum control and computation. *Rev. Mod. Phys.* **76**, 1037 (2005).

[Ver06] S. S. Verbridge, J. M. Parpia, R. B. Reichenbach, L. M. Bellan, and H. G. Craighead. High quality factor resonance at room temperature with nanostrings under high tensile stress. *J. Appl. Phys.* **99**, 124304 (2006).

[Ver07] S. S. Verbridge, D. F. Shapiro, H. G. Craighead, and J. M. Parpia. Macroscopic Tuning of Nanomechanics: Substrate Bending for Reversible Control of Frequency and Quality Factor of Nanostring Resonators. *Nano Lett.* **7**, 1728 (2007).

[Wal04] A. Wallraff, D. I. Schuster, A. Blais, L. Frunzio, R.-S. Huang, J. Majer, S. Kumar, S. M. Girvin, and R. J. Schoelkopf. Strong coupling of a single photon to a superconducting qubit using circuit quantum electrodynamics. *Nature* **431**, 162 (2004).

[Yan06] Y. Yang, C. Callegari, X. Feng, K. Ekinci, and M. Roukes. Zeptogram-Scale Nanomechanical Mass Sensing. *Nano Lett.* **6**, 583 (2006).

[You11] J. Q. You and F. Nori. Atomic physics and quantum optics using superconducting circuits. *Nature* **474**, 589 (2011).

[Yu12] P.-L. Yu, T. P. Purdy, and C. A. Regal. Control of Material Damping in High-Q Membrane Microresonators. *Phys. Rev. Lett.* **108**, 083603 (2012).

[Zen32] C. Zener. Non-adiabatic Crossing of Energy Levels. *Proc. R. Soc. Lond. A* **137**, 696 (1932).

List of Publications

- Quirin P. Unterreithmeier, Thomas Faust, Stephan Manus and Jörg P. Kotthaus. On-Chip Interferometric Detection of Nanomechanical Motion. *Nano Lett.* **10**, 887 (2010).

- Quirin P. Unterreithmeier, Thomas Faust, and Jörg P. Kotthaus. Nonlinear switching dynamics in a nanomechanical resonator. *Phys. Rev. B* **81**, 241405(R) (2010).

- Quirin P. Unterreithmeier, Thomas Faust, and Jörg P. Kotthaus. Damping of Nanomechanical Resonators. *Phys. Rev. Lett.* **105**, 027205 (2010).

- Thomas Faust, Peter Krenn, Stephan Manus, Jörg P. Kotthaus, and Eva M. Weig Microwave cavity-enhanced transduction for plug and play nanomechanics at room temperature. *Nat. Commun.* **3**, 728 (2012).

- Thomas Faust, Johannes Rieger, Maximilian J. Seitner, Peter Krenn, Jörg P. Kotthaus, and Eva M. Weig. Nonadiabatic Dynamics of Two Strongly Coupled Nanomechanical Resonator Modes. *Phys. Rev. Lett.* **109**, 037205 (2012).

- Johannes Rieger, Thomas Faust, Maximilian J. Seitner, Jörg P. Kotthaus, and Eva M. Weig. Frequency and Q factor control of nanomechanical resonators. *Appl. Phys. Lett.* **101**, 103110 (2012).

- Thomas Faust, Johannes Rieger, Maximilian J. Seitner, Jörg P. Kotthaus, Eva M. Weig. Coherent control of a nanomechanical two-level system. *arXiv*:1212.3172 [cond-mat.mes-hall] (2012).

Vielen Dank

Eine derartige Arbeit wäre ohne vielfältige Unterstützung nicht möglich. Deswegen möchte ich mich bei einigen Personen bedanken, die mir innerhalb der letzten Jahre geholfen haben und mich unterstützt haben:

Jörg Kotthaus danke ich für die Möglichkeit, an seinem Lehrstuhl meine Doktorarbeit anzufertigen. Er war während der gesamten Zeit ein exzellenter Betreuer, der sich stets Zeit nahm Ergebnisse zu diskutieren und viele Erklärungen und Anregungen liefern konnte.

Auch Eva Weig möchte ich für die Betreuung während der letzten Jahre danken, sie konnte mir bei Problemen stets weiterhelfen und hat mit guten Vorschlägen zum Gelingen der Experimente beigetragen. Zusammen mit Jörg hat sie auch viele gute Ideen und Formulierungen in die gemeinsamen Veröffentlichungen einfließen lassen und auch dafür gesorgt, dass wir nie einen Mangel an Geräten hatten.

Meinem Diplomanden Peter Krenn gilt mein besonderer Dank, durch seine unermüdliche, exzellente Arbeit an der Mikrowellendetektion hat er dieses Projekt zu einem grossen Erfolg gemacht, was dann zahlreiche weitere Messungen ermöglicht hat.

Johannes Rieger möchte ich für die gute Zusammenarbeit bei den zahlreichen gemeinsamen Projekten und für seine Mathematica-Tipps danken. Wir hatten innerhalb (und auch außerhalb) der Uni viel Spass während der vergangenen Jahre.

Seitdem Maximilian Seitner bei uns in der Gruppe seine Masterarbeit gemacht hat, war ich auch stets mit sehr guten Proben versorgt, sodass ich mich aufs Messen konzentrieren konnte, dafür vielen Dank.

Dank Quirin Unterreithmeier bin ich überhaupt in der Nanomechanik gelandet, und auch zu Beginn meiner Doktorarbeit hat er mich noch mit diversen Tipps unterstützt.

Stephan Manus danke ich für seine vielen Ratschläge zu elektronischen Problemen aller Art und für einige selbstgebaute Schaltungen, die manches Experiment erst ermöglicht haben.

Fredrik Hocke, Matthias Pernpeinter und Hans Hübl danke ich für die gute Kooperation beim Niob-Projekt, und besonders Matthias für die engagierte Fortführung des Projekts.

Daniela Taubert und Daniel Harbusch haben mir viele Fragen zur Cryo- und Vakuumtechnik beantwortet mir damit sehr beim Einstieg in die Tieftemperaturphysik und den damit verbundenen Problemen geholfen.

Bei Max Mühlbacher möchte ich mir für den Aufbau des Michelson-Interferometers bedanken, bei Todor Krastev für die Entwicklung verbesserter Microstrip-Kavitäten und bei Sophie Ratcliffe für das Design von Mikrowellen-Hohlraumresonatoren mit hoher Güte.

Philipp Altpeter und Reinhold Rath gilt mein besonderer Dank für den exzellenten Betrieb des Reinraums und für die Hilfe bei so manchem Vakuum- oder Prozessierungsproblem. Ich danke auch Wolfgang Kurpas und Anton Heindl für die Hilfe bei einigen mechanischen Konstruktionen.

Martina Jüttner und Bert Lorenz wissen bei bürokratischen Problemen stets was zu tun ist, dafür vielen Dank.

Dank meinen Zimmerkollegen Enrico Schubert, Jens Repp, Johannes Rieger und Matthias Hofmann herrschte bei uns im Büro stets eine gute Stimmung und es durfte auch mal gelacht werden.

Außerdem möchte ich mich bei den fleißigen Mensagängern und/oder Kaffetrinkern Daniel, Daniela, Darren, Enrico, Florian, Georg, Gunnar, Jens, Johannes, Matthias, Max, Peter und Sebastian für die zahlreichen interessanten und amüsanten Gespräche (manchmal auch über Physik) bedanken.

Zu guter Letzt danke ich dem gesamten Lehrstuhl für die ausgezeichnete Arbeitsatmosphäre und die gute Zusammenarbeit.